UNIVERSITY OF CALIFORNIA, SAN DIEGO

**The depth of mid-ocean ridges through Earth's evolution and a two-phase study of melt focusing at mid-ocean ridges**

A dissertation submitted in partial satisfaction of the
requirements for the degree
Doctor of Philosophy

in

Earth Science

by

Shi Sim

Committee in charge:

David R. Stegman, Co-Chair
James Day, Co-Chair
Donna Blackman
Juan Carlos Del Alamo
Jeff Gee
Marc Spiegelman

2018

The dissertation of Shi Sim is approved, and it is acceptable in quality and form for publication on microfilm and electronically:

_____

_____

_____

_____

_____
Co-Chair

_____
Co-Chair

University of California, San Diego

2018

DEDICATION

To my family, the Sims and the Naifs.

# EPIGRAPH

*We must not forget that when radium was discovered no one knew that it would prove useful in hospitals. The work was one of pure science. And this is a proof that scientific work must not be considered from the point of view of the direct usefulness of it. It must be done for itself, for the beauty of science, and then there is always the chance that a scientific discovery may become like the radium a benefit for mankind.*

—Marie Curie

TABLE OF CONTENTS

LIST OF FIGURES

LIST OF TABLES

ACKNOWLEDGEMENTS

I would like to acknowledge my wonderful advisor Dave Stegman for always being supportive and encouraging. Your guidance has been invaluable, both in science and in life. Thank you James Day for believing in me and helping me get back into enjoying science (also for always encouraging me to think beyond what I do and dwell to the dark side of petrology). Thank you Marc Spiegelman for your undying enthusiasm and incredible patience with me. You have really shown me the ropes in this game while being encouraging and challenging at the same time. Thank you to my committee, Donna Blackman, Jeff Gee and Juan Carlos del Alamo, who have graciously given me their valuable time in this journey. I am also grateful to Cian Wilson, who tirelessly showed me how to conquer TerraFERMA and will continue to do so.

Chapter 2, is a full reprint of the material as it appears in Gcubed 2016. Shi Sim, Dave R Stegman and Nicolas Coltice, "Effects of continental growth on mid-oceanic ridge depths", *Gcubed*, 2016. The dissertation/thesis author was the primary investigator and author of this paper. I would like to acknowledge my co-authors, Dave R. Stegman and Nicolas Coltice.

Chapter 3, in part, has been submitted for publication of the material as it may appear in Gcubed. The dissertation/thesis author was the primary investigator and author of this paper. I would like to acknowledge my co-authors, Marc Spiegelman, Dave R Stegman and Cian Wilson.

Chapter 4, in part is currently being prepared for submission for publication of the material. The dissertation/thesis author was the primary investigator and author of this material. I would like to acknowledge my co-authors, Marc Spiegelman, Dave R Stegman and Cian Wilson.

I am grateful to my family for always being there for me, through countless skype and facetime sessions. Thank you to my mom and dad for being the mountains that they are. Thank you to my brother and sister for being great role models, always inspiring/challenging me to be a better person and at the same time still being silly. I will always miss home with all of you.

A very special gratitude goes to Samer, who stood by me through the

hardest time and pulling me through whenever needed. Without you, I probably will not be here writing this. A big thank you to my new family, the Naifs, who have accepted me as one of their own. Thank you for immersing me into a beautiful culture with delicious food. I cannot ask for more.

A big thank you to my GP cohort, Nick, Fan, Maggie, Qian, Kyle, Peter, Jasper, Lauren, Kang, to our cheese breaks in the Keller and the many adventures through this perilous journey. Especially to Fan Wenyuan, a great friend who never stopped believing in me. I am also grateful to my SIO cohort for all the good times.

Thank you Gabi Laske, Jennifer Haase, Guy Masters, Lisa Tauxe, Steve and Cathy Constable, for being great role models in Science. I would like to also acknowledge IGPP and SIO admin who have helped so much along the way. To my office mate Jessie for keeping our forest alive and my other office mate Maya for staying there as long as possible. I am grateful to all the students who came before me, Andy, Brent, Erica, Xiao Wei, Robert, Valerie, Diego, Fernando, Soli, Eric, Matt for paving the way.

I am especially grateful to my little sisters Lyne and Lena for keeping me grounded in life. To all my friends, back home and stateside, Vanessa, Celina, Anastasia, the BBCians, Kai, Amanda, Sarika. Thank you to sunday hockey! To the people at Lamont and APAM Columbia who accepted me with open arms. To Owen, my unofficial officemate at both APAM and Lamont.

## VITA

| | |
|---|---|
| 2011 | B. S. in Earth Science *Honors*, University of California, San Diego |
| 2013 | M. Sc Mechanical Enginnering, University of California, San Diego |
| 2018 | Ph. D. in Earth Science, University of California, San Diego |

## PUBLICATIONS

Shi Joyce Sim, Dave R. Stegman and Nicolas Coltice, "Effects of continental growth on mid-oceanic ridge depths", *Gcubed*, 2016.

Shi Joyce Sim, Marc Spiegelman, Dave R. Stegman and Cian R. Wilson, "M3LT: A new model to explore the dynamics of Melt in the Mantle beneath Mid-ocean ridges", submitted, Gcubed.

Shi Joyce Sim, Marc Spiegelman, Dave R. Stegman and Cian R. Wilson, "Large scale organization of multiple melt focusing mechanisms in two-phase flow models of mid-ocean ridges", in preparation.

ABSTRACT OF THE DISSERTATION

**The depth of mid-ocean ridges through Earth's evolution and a two-phase study of melt focusing at mid-ocean ridges**

by

Shi Sim

Doctor of Philosophy in Earth Science

University of California, San Diego, 2018

David R. Stegman, Co-Chair
James Day, Co-Chair

Mid-ocean ridges are prominent features of plate tectonics, stretching for more than 60,000 km in the major ocean basins. Organisms thrive at mid-ocean ridges making it a unique system that connects life, water and plate tectonics. This thesis evaluates the evolution of the global ridge system and considers the processes of melt focusing beneath mid-ocean ridges using two phase flow models. First, I use whole Earth mantle convection models to understand how the global ridge system might have changed over Earth's evolution along with the depths of ocean. I show that mid-ocean ridges have remained submerged over geologic time and that its average depths have not varied by more than 500 m. Mid-ocean ridges

contribute to 90% of global magmatism and yet melt generation and extraction are not well understood due to the difficulty in surveying these systems submerged under a few kilometers of ocean. Active seismic and magnetotelluric surveys suggest that melt is generated in a wide region beneath mid-ocean ridges (*Forsyth et al.*, 1998; *Key et al.*, 2013) and yet the oceanic crust is formed within a narrow neovolcanic zone at the ridge axis (*Macdonald*, 1984). Several mechanisms to focus melt have been proposed (*Spiegelman and McKenzie*, 1987; *Phipps-Morgan*, 1987; *Sparks and Parmentier*, 1991; *Aharonov et al.*, 1995). I present new open source two phase models, Melt in the Mantle beneath Mid-ocean ridges (M3LT), based on TerraFERMA, the Transparent Finite Element Rapid Model Assembler (*Wilson et al.*, 2017), a software for coupled multi-physics problems. Our multi-phase flow models incorporate realistic viscosities and thermal feedbacks. To ensure reproducibility, the models are openly available in the form of TerraFERMA mark up language files. I present a suite of models varying the half spreading rates. The melt generated in our models produce oceanic crustal thicknesses within geophysical observations. We use these models to review and illustrate three mechanisms that are responsible for melt focusing namely, ridge suction, decompaction layers and melting rate focusing (recently observed mechanism). I show that decompaction layers and melting rate focusing are the dominant mechanisms for focusing melt at mid-ocean ridges. Model results show that the melting rate focusing persists regardless of half spreading rates, while the proportion of melt focused by decompaction layers increases with half spreading rate.

# Chapter 1

# Introduction: Mid-ocean ridges and Two phase flow

Mid-ocean ridges are the longest continuous feature of plate tectonics spanning more than 60,000 km in length and forming prominent geomorphic features through all of the ocean basins of the world (*Ito and Dunn*, 2009). The inference of seafloor spreading at these boundaries is one of the fundamental features defining the theory of continental drift (*Wilson*, 1963), which later on evolved to the theory of plate tectonics (*McKenzie and Parker*, 1967; *Morgan*, 1968; *McKenzie*, 1969). Mid-ocean ridges are the boundary between two oceanic plates that are moving apart from each other, causing the mantle beneath the oceanic crust to upwell and melt due to decompression. The melts generate about $3.3km^2/yr$ of new oceanic crust at mid-ocean ridges (*Parsons*, 1981) ($>$ 450 football fields created per year), and accounts for 90% of the magmatism on Earth.

The depths of oceanic crusts generally increase with age (*Stein and Stein*, 1992). Figure 1.1 shows a global map of oceanic crustal age, in which the mid-ocean ridges are indicated by black lines where zero aged (red) oceanic crust occur. The fact that mid-ocean ridges are overlain by kilometers of ocean makes them challenging features to directly observe. Satellite altimetry data and ship board sonar illuminate the ocean floor bathymetry. Sea-going surveys are typically divided into understanding shallow oceanic crustal formation or deeper magma dynamics beneath the mid-ocean ridges.

Shallow crustal formation is probed by active seismic using campaign style

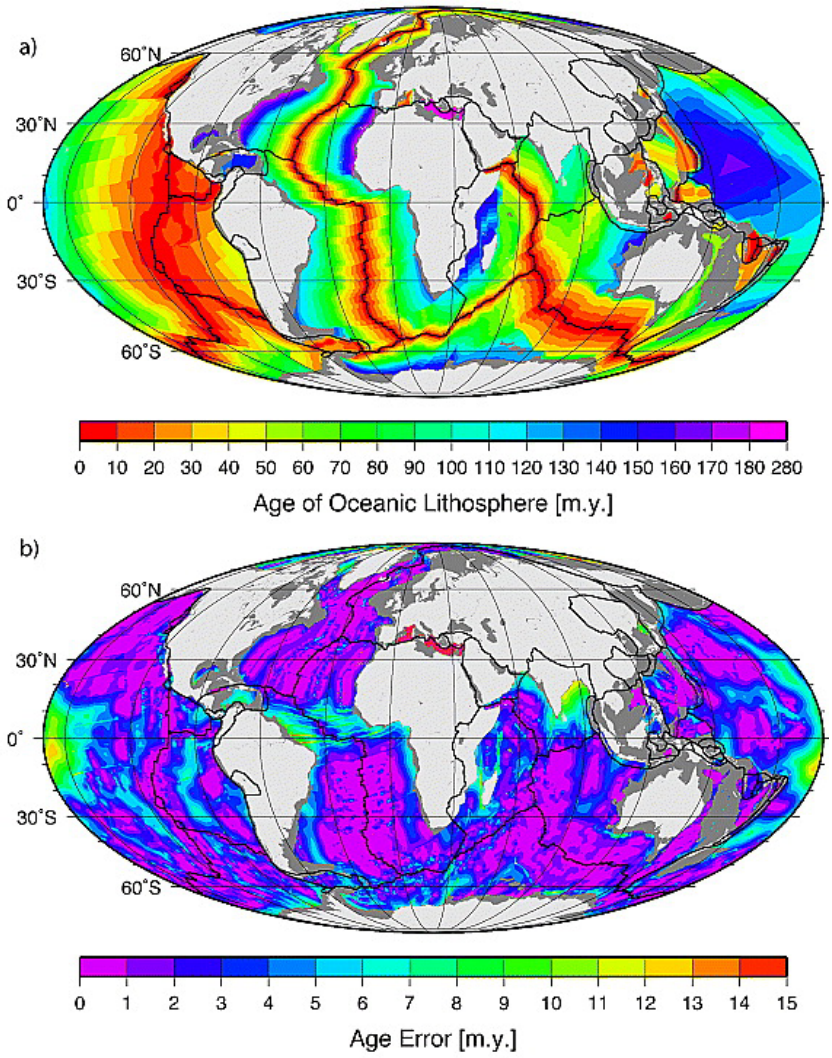


**Figure 1.1**: a) Age of oceanic crust and b) gridded age uncertainties from (*Müller et al.*, 2008)

ocean bottom seismometers (*White et al.*, 2001), controlled source electromagnetic methods using a towed source going over receivers on the seafloor (*Key et al.*, 2013), geochemical analysis of rocks collected in-situ (e.g *Cannat* (1993); *Dick et al.* (1984); *Salters and Dick* (2002)) and direct observations by submersible, remote-operated vehicles and autonomous underwater vehicles (Alvin etc) (*Ballard et al.*, 1975; *Haymon et al.*, 1993). Figure 1.2 shows the sampling density for presently-active mid-ocean ridges, which suggest that half of the mid-ocean ridges remain poorly sampled. A global dataset of oceanic crustal thicknesses versus

half spreading rates has been constructed using active seismic observations (*White et al.*, 1992; *Bown and White*, 1994; *White et al.*, 2001; *Harding et al.*, 2017) and a classic plot from *White et al.* (1992) (Figure 1.3) shows the fundamental observation that oceanic crustal thicknesses does not vary with spreading rate for spreading rates above 2 cm/yr. Shallow surveys investigate the presence of melt and layers in the oceanic crust (*Vera et al.*, 1990). In addition, ophiolites are thought to represent oceanic crust that have been obducted onto land (*Kelemen et al.*, 1997a) and have provided useful insights when studying the formation of oceanic crust.

The shallow oceanic crustal system is fed and coupled to the deeper mantle processes where melt generates and segregates. Deeper processes beneath the oceanic crust have been probed by geophysical methods (*Forsyth et al.*, 1998a,b; *Key et al.*, 2013), geological and geochemical analyses on abyssal peridoties (*Dick et al.*, 1984; *Snow et al.*, 1994; *Salters and Dick*, 2002; *Day et al.*, 2017) and mid-ocean ridge basalts (*Langmuir et al.*, 1977; *Klein and Langmuir*, 1987; *Langmuir et al.*, 1993; *Gale et al.*, 2013; *Shorttle*, 2015). The deeper processes are harder to observe, since no direct observations can be made. Geophysical surveys provides a snapshot in time of the system. With limited spatial and temporal observations on mid-ocean ridges, numerical models are necessary to complement this exploration (e.g *Spiegelman and McKenzie* (1987); *Morgan* (1987)).

Mid-ocean ridges are the focal point that connects life, water and plate tectonics. In chapter 2, We analyze numerical data from whole earth mantle convection models to understand how global ridge system might have changed over Earth's evolution. We study the growth of continents and the amount of water on the surface of the Earth over geologic time. Our results show that mid-ocean ridges have remained submerged over geologic time and that their average depths have not varied by more than 500 m.

## 1.1 Melt generation and extraction

It was established early on that the oceanic crustal thicknesses averaged about 7 km (Figure 1.3) and was independent of spreading rates above above

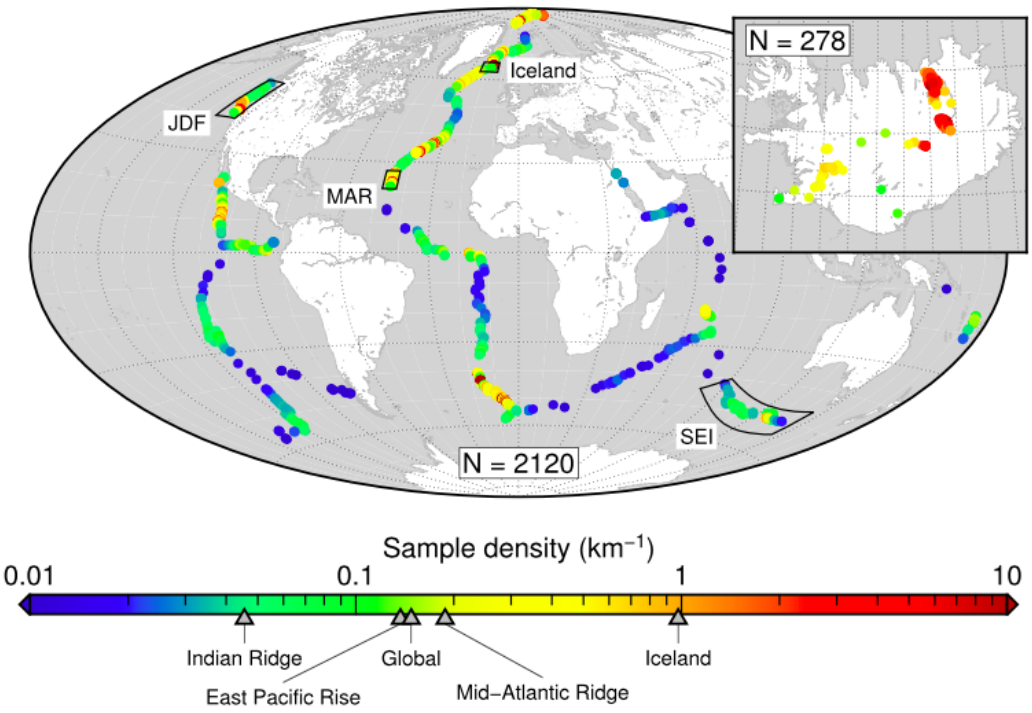


**Figure 1.2**: Global map of along ridge sample density (Figure 1 from *Shorttle* (2015)).

2 cm/yr. To create about 7 km of oceanic crust, the upper mantle potential temperature should be of the order of $1300°C$ (*Plank and Langmuir*, 1992; *Kinzler*, 1997; *Asimow et al.*, 2001). An extra 1 km of crust predicts a $25°C$ increase in mantle potential temperature, $T_m$ (Figure 1.4) (*Asimow et al.*, 2001).

Geochemical analyses of mid-ocean ridges basalts (MORB), abyssal peridotites and field observations from ophiolites suggest the upwelling mantle goes through fractional melting and that melt is extracted by porous flow (*Kelemen et al.*, 1997b; *Maclennan et al.*, 2002). Two dimensional models of the melting region beneath mid-ocean ridges using radiogenic excesses from Uranium decay at mid-ocean ridges suggest that U-series disequilibria is controlled by "mean melting rate at the base of the melting region and by melt fraction present during melting" (*Richardson and McKenzie*, 1994). These authors also suggest that melt extraction is relatively rapid (∼2000 years), which is best explained by channelized flows (*Richardson and McKenzie*, 1994). MORB is shown to be in disequilibrium with

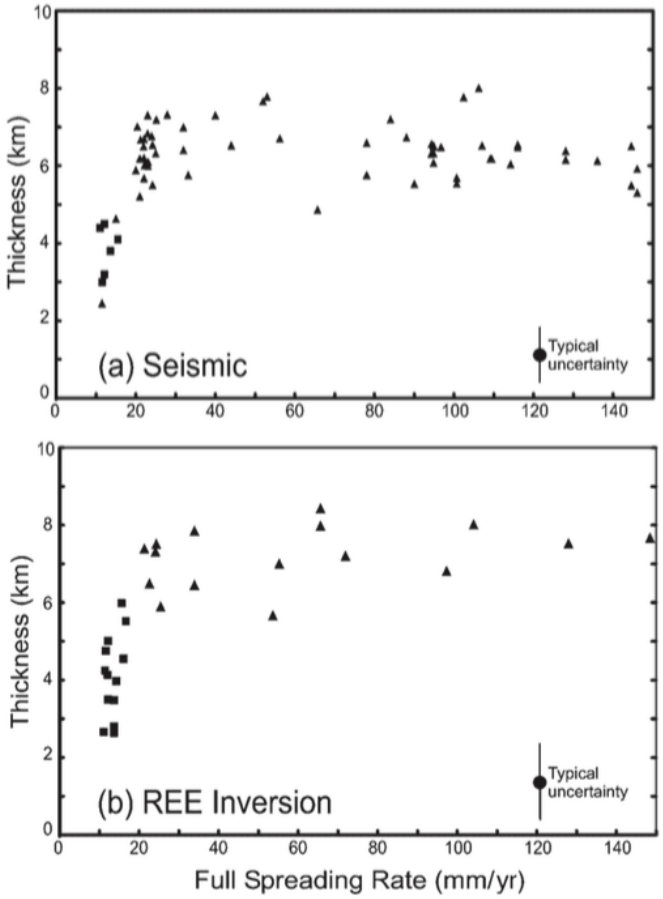


**Figure 1.3**: a) Seismic observations for oceanic igneous crustal thickness at MOR versus full spreading rates. b) Melt thickness inferred from the rare earth elements (REE) inversion (Figure 23 in *White et al.* (2001)).

shallow mantle, suggesting that the basaltic melt moved rapidly through the shallow mantle (*Maclennan et al.*, 2002). Main melt transport times are estimated to be $> 50m/yr$ for Iceland deglaciation, $1m/yr$ Australian/Antarctica, $2 - 5m/yr$ for the East Pacific Rise and $1m/yr$ for global mid-ocean ridges (*Maclennan et al.*, 2002).

Geochemical models suggest that melt segregates at low porosities $\sim$0.1% (*Faul*, 2001). However, geophysical surveys at the East Pacific Rise suggest higher melt porosities (*Forsyth et al.*, 1998a,b; *Key et al.*, 2013). This difference can be reconciled by taking into account the geometry and resulting permeability of the matrix along with dynamic behavior of the ascending melt (*Faul*, 2001).

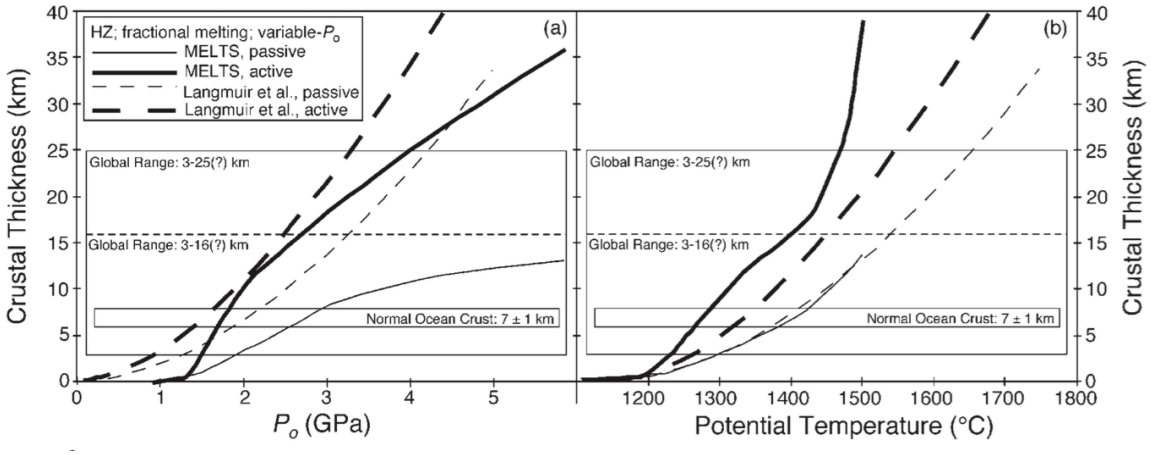


**Figure 1.4**: Oceanic crustal thickness predictions as a function of a) pressure and b) mantle potential temperature (Figure 9 from *Asimow et al.* (2001)).

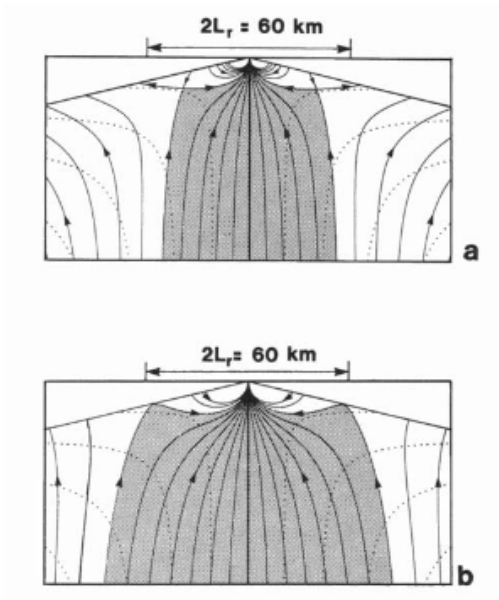


**Figure 1.5**: Analytical solutions for solid and melt flow at mid-ocean ridge at a) low constant porosity and b) higher constant porosity (Figure 3 from *Spiegelman and McKenzie* (1987)). Dotted lines are matrix flow lines and solid lines are melt flow lines.

Oceanic crust is created at a narrow neo-volcanic zone at the mid-ocean ridges but seismic surveys suggest the presence of partially molten mantle beneath mid-ocean ridges in a broad region of several hundred kilometers across and extending to depths more than 100 km (*Forsyth et al.*, 1998a,b). The MELT experiment

at the East Pacific Rise shows low velocities best explained by 1-2% melt (*Forsyth et al.*, 1998a,b). Magnetotelluric survey at another location of the East Pacific Rise also shows broad region of melt (*Key et al.*, 2013) but suggests higher melt porosities of up to 10%.

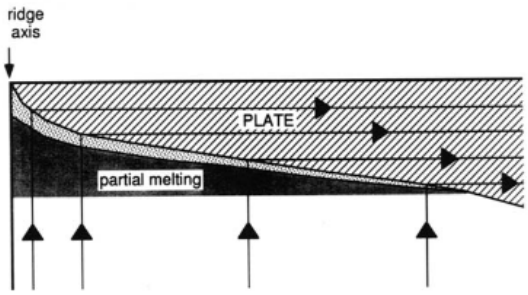


**Figure 1.6**: Simplified two-dimensional ridge model showing the high-porosity decompaction layer, which is the light stippled region (Figure 1 of *Sparks and Parmentier* (1991)).

Several focusing mechanisms have been proposed to explain melt focusing from melt generated in a wide region beneath the mid-ocean ridges. One such mechanism is negative dynamic pressure, due to incompressible shear, pulling in melt to the ridge axis from the surrounding (*Spiegelman and McKenzie*, 1987; *Morgan*, 1987) as shown in Figure 1.5. Aligned cracks create anisotropic permeability that allow melt to travel in a specific direction (*Morgan*, 1987). Similarly, shear driven melt bands from localization instability also align melt bands in accordance to shear direction (*Holtzman et al.*, 2003a,b; *Kohlstedt and Holtzman*, 2009). Decompaction layer is a commonly invoked mechanism (*Sparks and Parmentier*, 1991; *Spiegelman*, 1993a; *Hebert and Montési*, 2010; *Keller et al.*, 2017) with an example shown in Figure 1.6. In decompaction layer focusing, buoyant melt travels upwards from a wide melting region and encounters an impermeable cold strong lithosphere. The solid mantle has to open up pore space (decompact) to accommodate melt below the cold strong lithosphere. This melt rich decompaction layer moves melt towards the ridge axis as the lithosphere cools and thickens away from the ridge axis, creating an inverted funnel effect. Reactive infiltration instability can create melt channels that coalesce into larger channels as a way of focusing melt (*Aharonov et al.*, 1995). Last but not least, positive melting gradient causes a

negative compaction pressure pulling in melt to the region with the highest melting rate as observed recently (*Turner et al.*, 2017).

Based on the observations that melt is extracted at a faster rate compared to the upwelling mantle velocity to form ∼6-7 km of oceanic crust, a multi-phase approach is ideal to understand this porous melt flow.

## 1.2 Two phase flow for Earth material

The theoretical framework for two phase flow applied to mantle material was developed independently by several workers (*McKenzie*, 1984; *Fowler*, 1985; *Scott and Stevenson*, 1986). The set of governing equations describe fluid melt percolating in a viscously deforming and permeable solid mantle, where the solid mantle is more viscous than the fluid by a few orders of magnitude. These equations are highly coupled and to begin to understand the underlying physics requires simple analytical solutions (*Spiegelman and McKenzie*, 1987; *Morgan*, 1987; *Spiegelman*, 1993b,c). The fundamental equations have not changed significantly but extensions have been made to the energy equation to include surface energies (*Bercovici et al.*, 2001a,b; *Ricard et al.*, 2001; *Bercovici and Ricard*, 2003) and the assumption of zero compaction length has been used (*Buck and Su*, 1989; *Sotin and Parmentier*, 1989). To close the set of governing equations, constitutive relations are required to describe the solid rheology, permeability and, in particular, melting rate, $\Gamma$ and the choices typically changes from one model to the next. The boundary conditions also change depending on each model setting.

### 1.2.1 Two phase flow beneath mid-ocean ridges

In Chapter 3, we present a new open source two phase model, Melt in the Mantle beneath Mid-ocean ridges, M3LT. Our goal is to ensure the reproducibility of our results by being transparent about the model choices made. We use TerraFERMA, the Transparent Finite Element Rapid Model Assembler (*Wilson et al.*, 2017). Since these two phase models are complex, we dedicate this paper to describe the model, especially the closures, boundary conditions and numerical methods in detail. Even so, as with any complex model, it is difficult to describe

every single detail in a paper such that the models can be reproduced exactly. We provide the code in the form of TerraFERMA mark up language files (.tfml). The example model produces an average crustal thickness that is within geophysical observations. From our models, we describe three melt focusing mechanisms, one of which was recently recognized.

In Chapter 4, we use M3LT to explore how varying spreading rates changes magma dynamics and melt focusing. These models also produce oceanic crustal thicknesses versus half spreading rates that are within seismic observations. We also show that the persistence of porosity waves with decreasing half spreading rate contributes to the lower variability in oceanic crustal thicknesses with increasing half spreading rate. We analyze how the melt focusing mechanisms vary with spreading rate. Our analysis suggests that magmatic focusing decreases slightly with spreading rate whereas decompaction layers seem to increase rapidly below half spreading rate of 4 cm/yr and then decrease beyond that.

# References


Aharonov, E., J. Whitehead, P. Kelemen, and M. Spiegelman (1995), Channeling instability of upwelling melt in the mantle, *Journal of Geophysical Research: Solid Earth*, *100*(B10), 20,433–20,450.

Asimow, P. D., M. Hirschmann, and E. Stolper (2001), Calculation of peridotite partial melting from thermodynamic models of minerals and melts, iv. adiabatic decompression and the composition and mean properties of mid-ocean ridge basalts, *Journal of Petrology*, *42*(5), 963–998.

Ballard, R., W. Bryan, J. Heirtzler, G. Keller, J. Moore, and T. Van Andel (1975), Manned submersible observations in the famous area: Mid-atlantic ridge, *Science*, *190*(4210),103–108.

Bercovici, D., and Y. Ricard (2003), Energetics of a two-phase model of lithospheric damage, shear localization and plate-boundary formation, *Geophysical Journal International*, *152*(3), 581–596.

Bercovici, D., Y. Ricard, and G. Schubert (2001a), A two-phase model for compaction and damage: 1. general theory, *Journal of Geophysical Research: Solid Earth*, *106*(B5), 8887–8906.

Bercovici, D., Y. Ricard, and G. Schubert (2001b), A two-phase model for compaction and damage: 3. applications to shear localization and plate boundary formation, *Journal of Geophysical Research: Solid Earth*, *106*(B5), 8925–8939.

Bown, J. W., and R. S. White (1994), Variation with spreading rate of oceanic crustal thickness and geochemistry, *Earth and Planetary Science Letters*, *121*(3-4), 435–449.

Buck, W. R., and W. Su (1989), Focused mantle upwelling below mid-ocean ridges due to feedback between viscosity and melting, *Geophysical Research Letters*, *16*(7), 641–644.

Cannat, M. (1993), Emplacement of mantle rocks in the seafloor at mid-ocean ridges, *Journal of Geophysical Research: Solid Earth*, *98*(B3), 4163–4172.

Day, J. M., R. J. Walker, and J. M. Warren (2017), 186 Os–187 Os and highly siderophile element abundance systematics of the mantle revealed by abyssal peridotites and Os-rich alloys, *Geochimica et Cosmochimica Acta*, *200*, 232–254.

Dick, H. J., R. L. Fisher, and W. B. Bryan (1984), Mineralogic variability of the uppermost mantle along mid-ocean ridges, *Earth and Planetary Science Letters*, *69*(1), 88–106.

Faul, U. H. (2001), Melt retention and segregation beneath mid-ocean ridges, *Nature*, *410*(6831), 920.

Forsyth, D. W., S. C. Webb, L. Dorman, and Y. Shen (1998a), Phase velocities of Rayleigh waves in the MELT experiment on the East Pacific Rise, *Science*, *280*(5367), 1235–1238.

Forsyth, D. W., D. S. Scheirer, S. C. Webb, and L. M. Dorman (1998b), Imaging the deep seismic structure beneath a mid-ocean ridge: The MELT experiment, *Science*, *280*(5367), 1215-1220.

Fowler, A. (1985), A mathematical model of magma transport in the asthenosphere, *Geophysical & Astrophysical Fluid Dynamics*, *33*(1-4), 63–96.

Gale, A., C. A. Dalton, C. H. Langmuir, Y. Su, and J.-G. Schilling (2013), The mean composition of ocean ridge basalts, *Geochemistry, Geophysics, Geosystems*, *14*(3), 489–518.

Harding, J. L., H. J. Van Avendonk, N. W. Hayman, I. Grevemeyer, C. Peirce, and A. Dannowski (2017), Magmatic-tectonic conditions for hydrothermal venting on an ultraslow-spread oceanic core complex, *Geology*, *45*(9), 839–842.

Haymon, R., D. Fornari, K. L. Von Damm, M. Lilley, M. Perfit, J. Edmond, W. C. Shanks III, R. Lutz, J. Grebmeier, S. Carbotte, et al. (1993), Volcanic eruption of the mid-ocean ridge along the east pacific rise crest at 9 45–52' N: Direct submersible observations of seafloor phenomena associated with an eruption event in April, 1991, *Earth and Planetary Science Letters*, *119*(1-2), 85–101.

Hebert, L. B., and L. G. Montési (2010), Generation of permeability barriers during melt extraction at mid-ocean ridges, *Geochemistry, Geophysics, Geosystems*, *11*(12).

Holtzman, B., D. Kohlstedt, M. Zimmerman, F. Heidelbach, T. Hiraga, and J. Hustoft (2003a), Melt segregation and strain partitioning: implications for seismic anisotropy and mantle flow, *Science*, *301*(5637), 1227–1230.

Holtzman, B., N. Groebner, M. Zimmerman, S. Ginsberg, and D. Kohlstedt (2003b), Stress-driven melt segregation in partially molten rocks, *Geochemistry, Geophysics, Geosystems*, *4*(5).

Ito, G., and R. A. Dunn (2009), Mid-ocean ridges: Mantle convection and formation of the lithosphere, *Encyclopedia of Ocean Sciences*, 867–880.

Johnson, K., H. J. Dick, and N. Shimizu (1990), Melting in the oceanic upper mantle: an ion microprobe study of diopsides in abyssal peridotites, *Journal of Geophysical Research: Solid Earth*, *95*(B3), 2661–2678.

Kelemen, P. B., K. Koga, and N. Shimizu (1997a), Geochemistry of gabbro sills in the crust-mantle transition zone of the Oman ophiolite: implications for the origin of the oceanic lower crust, *Earth and Planetary Science Letters*.

Kelemen, P. B., G. Hirth, N. Shimizu, M. Spiegelman, and H. J. Dick (1997b), A review of melt migration processes in the adiabatically upwelling mantle beneath oceanic spreading ridges, *Philosophical Transactions of the Royal Society A: Mathematical, Physical and Engineering Sciences*, *355*(1723), 283–318.

Keller, T., R. F. Katz, and M. M. Hirschmann (2017), Volatiles beneath mid-ocean ridges: Deep melting, channelised transport, focusing, and metasomatism., *Earth and Planetary Science Letters*, *464*, 55–68.

Key, K., S. Constable, L. Liu, and A. Pommier (2013), Electrical image of passive mantle upwelling beneath the northern East Pacific Rise, *Nature*, *495*(7442), 499–502.

Kinzler, R. J. (1997), Melting of mantle peridotite at pressures approaching the spinel to garnet transition: Application to mid-ocean ridge basalt petrogenesis, *Journal of Geophysical Research: Solid Earth*, *102*(B1), 853–874.

Klein, E. M., and C. H. Langmuir (1987), Global correlations of ocean ridge basalt chemistry with axial depth and crustal thickness, *Journal of Geophysical Research: Solid Earth*, *92*(B8), 8089–8115.

Kohlstedt, D. L., and B. K. Holtzman (2009), Shearing melt out of the earth: An experimentalist's perspective on the influence of deformation on melt extraction, *Annual Review of Earth and Planetary Sciences*, *37*, 561–593.

Langmuir, C. H., J. Bender, A. Bence, G. Hanson, and S. Taylor (1977), Petrogenesis of basalts from the famous area: Mid-atlantic ridge, *Earth and Planetary Science Letters*, *36*(1), 133–156.

Langmuir, C. H., E. M. Klein, and T. Plank (1993), Petrological systematics of mid-ocean ridge basalts: Constraints on melt generation beneath ocean ridges, *Mantle flow and melt generation at mid-ocean ridges*, pp. 183–280.

Maclennan, J., M. Jull, D. McKenzie, L. Slater, and K. Grönvold (2002), The link between volcanism and deglaciation in iceland, *Geochemistry, Geophysics, Geosystems*, *3*(11), 1–25.

McKenzie, D. (1984), The Generation and Compaction of Partially Molten Rock, *Journal of Petrology*, pp. 1–53.

McKenzie, D. P. (1969), Speculations on the consequences and causes of plate motions, *Geophysical Journal International*, *18*(1), 1–32.

McKenzie, D. P., and R. L. Parker (1967), The north pacific: an example of tectonics on a sphere, *Nature*, *216*(5122), 1276.

Morgan, J. P. (1987), Melt migration beneath mid-ocean spreading centers, *Geophysical Research Letters*, *14*(12), 1238–1241.

Morgan, W. J. (1968), Rises, trenches, great faults, and crustal blocks, *Journal of Geophysical Research*, *73*(6), 1959–1982.

Müller, R. D., M. Sdrolias, C. Gaina, and W. R. Roest (2008), Age, spreading rates, and spreading asymmetry of the world's ocean crust, *Geochemistry, Geophysics, Geosystems*, *9*(4).

Parsons, B. (1981), The rates of plate creation and consumption, *Geophysical Journal International*, *67*(2), 437–448.

Plank, T., and C. H. Langmuir (1992), Effects of the melting regime on the composition of the oceanic crust, *Journal of Geophysical Research: Solid Earth*, *97*(B13), 19,749–19,770.

Pommier, A., and E. Garnero (2014), Petrology-based modeling of mantle melt electrical conductivity and joint interpretation of electromagnetic and seismic results, *Journal of Geophysical Research: Solid Earth*, *119*(5), 4001–4016.

Ricard, Y., D. Bercovici, and G. Schubert (2001), A two-phase model for compaction and damage: 2. applications to compaction, deformation, and the role

of interfacial surface tension, *Journal of Geophysical Research: Solid Earth*, *106*(B5), 8907–8924.

Richardson, C., and D. McKenzie (1994), Radioactive disequilibria from 2d models of melt generation by plumes and ridges, *Earth and Planetary Science Letters*, *128*(3-4), 425–437.

Salters, V. J., and H. J. Dick (2002), Mineralogy of the mid-ocean-ridge basalt source from neodymium isotopic composition of abyssal peridotites, *Nature*, *418*(6893), 68.

Scott, D. R., and D. J. Stevenson (1986), Magma ascent by porous flow, *Journal of Geophysical Research: Solid Earth*, *91*(B9), 9283–9296.

Shorttle, O. (2015), Geochemical variability in morb controlled by concurrent mixing and crystallisation, *Earth and Planetary Science Letters*, *424*, 1–14.

Snow, J. E., S. R. Hart, and H. J. Dick (1994), Nd and sr isotope evidence linking mid-ocean-ridge basalts and abyssal peridotites, *Nature*, *371*(6492), 57.

Sotin, C., and E. Parmentier (1989), Dynamical consequences of compositional and thermal density stratification beneath spreading centers, *Geophysical Research Letters*, *16*(8), 835–838.

Sparks, D. W., and E. M. Parmentier (1991), Melt extraction from the mantle beneath spreading centers, *Earth and Planetary Science Letters*, *105*(4), 368–377.

Spiegelman, M. (1993a), Physics of Melt Extraction: Theory, Implications and Applications, *Philosophical Transactions of the Royal Society A: Mathematical, Physical and Engineering Sciences*, *342*(1663), 23–41.

Spiegelman, M. (1993b), Flow in deformable porous media. Part 1 Simple analysis, *Journal of Fluid Mechanics*, *247*(-1), 17–38.

Spiegelman, M. (1993c), Flow in deformable porous media. part 2 numerical analysis–the relationship between shock waves and solitary waves, *Journal of Fluid Mechanics*, *247*, 39–63.

Spiegelman, M., and D. McKenzie (1987), Simple 2-D models for melt extraction at mid-ocean ridges and island arcs, *Earth and Planetary Science Letters*.

Stein, C. A., and S. Stein (1992), A model for the global variation in oceanic depth and heat flow with lithospheric age, *Nature*, *359*(6391), 123.

Turner, A. J., R. F. Katz, M. D. Behn, and T. Keller (2017), Magmatic Focusing to Mid-Ocean Ridges: The Role of Grain-Size Variability and Non-Newtonian Viscosity, *Geochemistry Geophysics Geosystems*, *23*(1), 15.

Vera, E., J. Mutter, P. Buhl, J. Orcutt, A. Harding, M. Kappus, R. Detrick, and T. Brocher (1990), The structure of 0-to 0.2-my-old oceanic crust at 9 n on the east pacific rise from expanded spread profiles, *Journal of Geophysical Research: Solid Earth*, *95*(B10), 15,529–15,556.

White, R. S., D. McKenzie, and R. K. O'Nions (1992), Oceanic crustal thickness from seismic measurements and rare earth element inversions, *Journal of Geophysical Research: Solid Earth*, *97*(B13), 19,683–19,715.

White, R. S., T. A. Minshull, M. J. Bickle, and C. J. Robinson (2001), Melt generation at very slow-spreading oceanic ridges: Constraints from geochemical and geophysical data, *Journal of Petrology*, *42*(6), 1171–1196.

Wilson, C. R., M. Spiegelman, and P. E. van Keken (2017), TerraFERMA: The Transparent Finite Element Rapid Model Assembler for multiphysics problems in Earth sciences, *Geochemistry Geophysics Geosystems*, *18*(2), 769–810.

Wilson, J. T. (1963), Evidence from islands on the spreading of ocean floors, *Nature*, *197*(4867), 536.

# Chapter 2

# Mid-ocean ridge depths through Earth's history

## 2.1 Abstract

The interconnectedness of life, water, and plate tectonics is strikingly apparent along mid-ocean ridges (MOR) where communities of organisms flourish off the disequilibrium of chemical potentials created by circulation of hydrothermal fluids driven by Earth's heat (*Nisbet and Sleep*, 2001; *Staudigel et al.*, 2004). Moreover, submarine hydrothermal environments may be critical for the emergence of life on Earth (*Nisbet and Sleep*, 2001). Oceans were likely present in the Hadean (*Valley et al.*, 2002; *Harrison*, 2009) but questions remain about early Earth's global tectonics (*Van Hunen and Moyen*, 2012), including when seafloor spreading began and whether mid-oceanic ridges were deep enough for maximum hydrothermal activities (*Kasting et al.*, 2006). For example, plate tectonics influences global sea level by driving secular variations in the volume of ocean basins due to continental growth (*Flament et al.*, 2008). Similarly, variations in the distribution of seafloor age and associated subsidence (*Flament et al.*, 2008), due to assembly and dispersal of supercontinents (*Coltice et al.*, 2012), explains the largest sea level variation over the past 140 Myr (*Müller et al.*, 2008). Using synthetic plate configurations derived from numerical models of mantle convection (*Coltice et al.*, 2012, 2014) appropriate for early Earth, we show that MOR has remained submerged and its depths potentially constant over geologic time. Thus, conditions in the early Earth existed for hydrothermal vents at similar depths as today, providing

environments conducive for the development of life and allowing for processes such as hydrothermal alteration of oceanic crust to influence the mantle's geochemical evolution.

## 2.2 Introduction

Earth's oceans have played an important role in the evolution of life and tectonics on Earth, including establishing conditions for the deep biosphere at mid-oceanic ridges (MORs) (*Nisbet and Sleep*, 2001), promoting single-sided and asymmetric subduction (*Gerya et al.*, 2008), and the emergence of stable continental platforms (*Flament et al.*, 2008). The early Earth is expected to have started with a warmer mantle and cooled over time such that the associated Rayleigh number for the mantle would have been higher in Earth's past. The nature of tectonics that occurred during the early Earth is unknown, with some studies proposing that Earth was in a stagnant lid tectonic regime (*Debaille et al.*, 2013; *O'Neill and Debaille*, 2014) and possibly cooled primarily through volcanism (*Moore and Webb*, 2013) and that possibly drip-tectonics generated Archean crust through delamination of unstable crust (*Johnson et al.*, 2014; *Manning*, 2004). Other studies support the uniformitarian view that recycling of the lithosphere, in some form, has occurred throughout Earth's history (*Höning and Spohn*, 2016). However, geodynamic models indicate that subduction operates differently in a higher mantle temperature, perhaps with more shallow underthrusting (*Sizova et al.*, 2010). For this study we do not presume that plate tectonics was operating in its present form but we explore the scenario in which some kind of mobile lid regime existed with a surface boundary layer being recycled at a rate that could accommodate the higher Rayleigh number.

Hydrothermal activities at MORs make them a potential locational candidate for the origin of life (*Nisbet and Sleep*, 2001). The maximum depth of hydrothermal penetration into oceanic crust at mid-oceanic spreading centers is a primarily a function of the MOR crest depth, but also depends on many things that would be different for the early Earth such as the seawater chemistry, the thickness and porosity of the ocean crust, and the rate of pelagic sedimentation (*Kasting*

*et al.*, 2006). Hydrothermal penetration depth also alters the oceanic crust that is being subducted back into the mantle through metasomatism (*Staudigel*, 2014). The subduction of altered oceanic crust brings volatiles like water and carbonates down into the mantle (*Manning*, 2004; *Jarrard*, 2003), creating flux melting in the mantle wedge as the subducted crust gets dehydrated (*Plank and Langmuir*, 1993; *Plank et al.*, 2009; *Hacker*, 2008). Thus, not only does the suitability of the hydrothermal environment for the origin of life on Earth depend on the MOR depth, but so does the cycling of elements into Earth's deep interior.

Models of relevant tectonic processes and geochemical observations can help to understand the otherwise poorly known depth of early Earth's oceans, in particular the depth to which MORs were submerged, which is also debated (*Kasting et al.*, 2006). MOR depth depends on the ocean basin volume over time as well as the total volume of ocean water. Previous global sea level models account for ocean basin volume by considering globally averaged seafloor subsidence based on a parameterized global heat flow model (*Schubert and Reymer*, 1985) that neglected fluctuations of seafloor age distribution (*Labrosse and Jaupart*, 2007). Such fluctuations, attributed to the changing distribution of continents on the Earth's surface (*Coltice et al.*, 2012), have a greater impact on global sea level compared to variations of spreading rates (*Xu et al.*, 2006; *Loyd et al.*, 2007). Indeed, the ocean basin volume based on reconstructed seafloor age distributions since 140 Ma compares favorably with the observed long term trend of global sea level over the same time (*Müller et al.*, 2008). Additionally, the amount of Earth's surface covered by continents also drives significant variation of seafloor age distribution (*Coltice et al.*, 2014) but the corresponding effect on global MOR depth has yet to be investigated. This study uses mantle convection models to address the question of how the depth of the MOR may have changed over geologic time.

## 2.3 Model setup

The 3D spherical mantle convection models computed here have similar parameterizations to those previously published (*Bello et al.*, 2015), except that no surface velocities are imposed here (so we model convection with free slip bound-

ary conditions). We solve the equations of incompressible convection using the StagYY code (*Tackley*, 2008). Viscosity is the only variable material property in our models. Variations of other material properties (expansion coefficient, thermal diffusivity, heat production) are neglected. The basal heating Rayleigh number $Ra$ here is $10^6$ in these models, mostly because of computational limitations. The average resolution is 45 km laterally and vertically for all the models. The models have mixed heating, internal heating representing about 85% of the total heat in the system.

The viscosity in our models depends on temperature and depth as

$$\eta(T, z) = \eta(z) \exp\left(0.064 + \frac{30}{T+1}\right),$$

where $z$ is the depth. The non-dimensional activation energy being 30 here produces 6 orders of magnitude of viscosity variations with temperature. The depth-dependence of viscosity $\eta(z)$ is taken into account such that a gradual viscosity increase by a factor of 30 occurs between 750 km and 850 km depth.

Pseudo-plasticity is implemented through a stress dependence of the viscosity with a yield stress (*Coltice et al.*, 2012, 2014). We choose a non-dimensional value of 15,000 to produce a plate-like behavior and large-scale convective flow. Continents are modeled as viscous buoyant rafts of complex polygonal shapes (*Rolf and Tackley*, 2011).

The models are started from ad hoc initial conditions, and run for up to 5 billion years to ensure statistical steady-state and stability of the dynamic regime. Such long runs ensure that initial conditions are forgotten. From the solutions at statistical steady-state, we compute the dynamic evolutions for integration times over 4 Gyr (scaling time with present-day transit time) of the models that are analysed in this study. The age of the seafloor is computed from the value of the heat flow (*Coltice et al.*, 2012, 2014). Since small-scale convection is limited in these models, this approximation is effective.

For a constant internally heated mantle, an appropriate estimate of the Rayleigh number (Ra) of the Earth, gives a value of $4.4 \times 10^8$ assuming a mantle viscosity of $\eta = 2 \times 10^{20}$ Pa s. The $Ra$ for the Earth corresponds to the observed RMS surface velocity of the Earth, $V_{surf} = 3.8$ cm/yr, giving an estimated transit

time of the mantle, $\tau_v = H/V_{surf} = 73$ Ma using mantle depth of $H = 2890$ km. Since we adopt a smaller value ($Ra \sim 10^6$) for convection in the numerical model, we have to scale the computed numbers to the present day Earth's values taking the RMS surface velocity of the model (*Coltice et al.*, 2012), thus time is dimensionalized $t = t^{model} \times \tau_v/\tau_v^{model}$.

The vigor of convection (Rayleigh number) is lower in the models than for the Earth. Therefore, we scale our results to obtain values we can compare to the Earth. A classical way to do so is to scale the time to the transit time, which is the time a rock would take to cross the mantle at the root-mean-square velocity $V_{surf}$ at the surface of the planet. Taking $V_{surf} = 3.8$ cm/yr, the estimated transit time of the present-day mantle is $\tau_v = H/V_{surf} = 73$ Myr. In the following, seafloor ages are scaled following the relationship $t = t^{model} \times \tau_v/\tau_v^{model}$. The present-day transit time is easy to evaluate, we will discuss later how we evaluate transit time in the distant past.

## 2.4 Results

### 2.4.1 Estimates of MOR depths

A natural definition for global sea level in the absence of continental hypsometry (*Flament et al.*, 2011) is the depth of MOR crest. The MOR depth can be estimated by filling the volume of the ocean basins assuming the modern day volume of water (*Eakins and Sharman*, 2010) and that the continents are never inundated or submerged. Although the total volume of water above any submerged continental shelf, or that above entirely submerged continents, is not accounted for in our models, the additional uncertainty it introduces in our estimates of MOR depth is not significant compared to other sources of uncertainty. To estimate ocean volume, we first generate synthetic seafloor age maps using the methodology in previous studies (*Coltice et al.*, 2012, 2014).

As oceanic crust moves away from mid-oceanic spreading centers where it is created, it not only ages but it also cools and subsides. This bathymetry associated with the synthetic seafloor age distributions is calculated using a half-

space cooling model (*Stein and Stein*, 1992; *Hasterok*, 2013). The total volume of water the ocean basins can accommodate is then calculated by integrating the predicted bathymetry over the Earth's surface.

The computational expense for running global spherical convection models at conditions appropriate for the early Earth is prohibitive. Instead, the values for the reference model can be scaled to higher Ra combining the transit time scaling expressed above, and using boundary layer theory which predicts that the surface velocity scales as $Ra^{2/3}$. To approximate conditions for early Earth, we consider the change in Rayleigh number caused by a higher temperature in the mantle. This change is

$$\frac{Ra}{Ra_0} = \frac{\bar{T} \exp \frac{Q}{R\bar{T}_0}}{\bar{T}_0 \exp \frac{Q}{R\bar{T}}},$$

where the subscript 0 means present-day, and $\bar{T}$ is the average temperature of the mantle. It is computed averaging the adiabat over the depth of the mantle. Assuming a temperature of 1590 K beneath oceanic plates today (*McKenzie et al.*, 2005), the average temperature along the adiabat is about 2200 K. *Herzberg et al.* (2010) recently estimated a temperature drop of 150 to 250 K for the whole mantle since the Archean. Taking into account the propagation of uncertainties on the activation energy for the viscosity (290 to 520 kJ mol$^{-1}$ (*Mei and Kohlstedt*, 2000; *Karato and Jung*, 2003)), we choose a factor of 10 change in Rayleigh number since the Archean (this value corresponds to the upper one standard deviation). For the Hadean, the temperature of the mantle is at most that of the liquidus and therefore a value of 2700 K is a maximum (*Jaupart et al.*, 2007), and the Archean temperature would be the lower bound. We choose a factor of 100 change in Rayleigh number, again a high end value for the Rayleigh number considering the propagation of uncertainties. Choosing high-end numbers implies we explore the largest changes we can expect in terms of sea-level. These values for Ra, in agreement with previously proposed estimates (*Sleep et al.*, 2001; *Zahnle et al.*, 2007), result in faster surface velocities and, on-average, younger seafloor. The resultant transit times of the models, $\tau_v = 16.5$ and 3.6 Myr, respectively, scale the maximum age of the synthetic seafloor accordingly.

We ran a suite of whole Earth mantle convection models accounting for

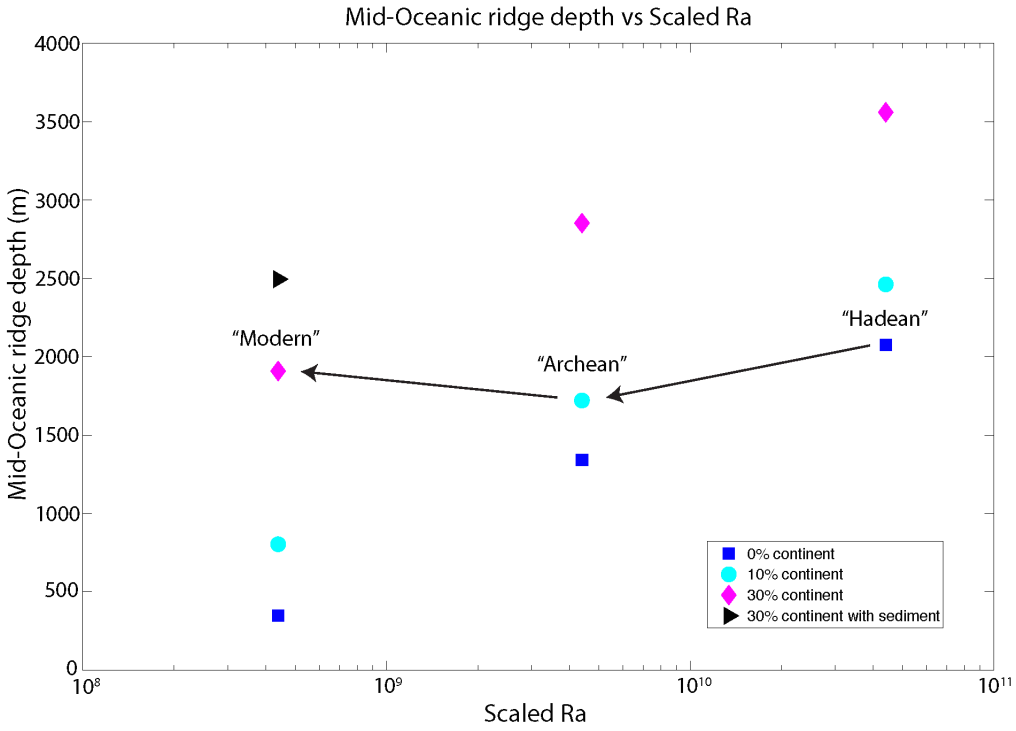


**Figure 2.1**: Mean mid-oceanic ridge depth calculated from all mantle convection model runs with corresponding scaled Ra and relative amount of continents. Details on the calculations described in text. Black arrows represent our preferred temporal evolution of mid-oceanic ridge depths that we will focus on for the rest of the paper. The rest of the figures in this paper correspond to models following this preferred temporal evolution.

varying amounts of continents (0, 10 and 30% of total surface area of the Earth) and scale the results for Rayleigh numbers 10 and 100 times larger than today. We calculate MOR depths for each time-step of every model, and then compute a single time-averaged MOR depth which is shown in Figure 2.1. Figure 2.1 shows MORs become deeper with increasing amounts of continent, because of the associated decreasing surface area available for oceans. Thus, a larger proportion of the ocean volume will be accommodated above the MOR. Figure 2.1 also shows MOR depths become shallower with decreasing Ra, because slower moving plates allow for greater subsidence of the ocean floor which allows ocean basins to hold a larger proportion of the ocean volume. These two effects compete against each other in the case when there are less continents for the higher Ra system and more

continents in the lower Ra system.

### 2.4.2 "Modern", "Archean" and "Hadean" models

Using models described in the previous section, we investigate the effect continental growth has on seafloor age distributions and the associated global MOR depth variations within the context of Earth's thermal evolution. If one assume that continents have grown and Ra in the mantle has decreased monotonically through time, this then limits the possible paths of time evolution of mid-oceanic ridges depth given our suite of models. We have highlighted our preferred path using black arrows in Figure 2.1.

We explore the scenario that the high Ra ($Ra = 4.4 \times 10^{10}$) corresponds to when the Earth had no continents and refer to this as the "Hadean" model. Similarly, we consider that chronologically, as Earth cooled to a lower Ra ($Ra = 4.4 \times 10^{9}$) perhaps 10% continents would have been present so we refer to this case as the "Archean" model. Lastly, we consider a "Modern" case to be a model with 30% continents and $Ra = 4.4 \times 10^{8}$. For the "Modern" case, we consider sediments using a sediment thickness model (*Müller et al.*, 2008) fitting modern day sediment thickness data (*Divins*, 2003) and the corresponding mean MOR is plotted as a black triangle in Figure 2.1. We will focus on these three models for the rest of the paper.

Figure 2.2a-c shows a representative snapshot of the synthetic seafloor age distribution for each of the three cases. The color scales are the same for all three models. Figure 2.2a shows an age range for the "Modern" model similar to what is observed on Earth today, as is expected since the RMS surface velocity of the model is scaled to that of present-day Earth. Figure 2.2b,c show that typical ages for synthetic seafloor in the "Archean" and "Hadean" models are much younger than in the "Modern" model.

The blue line in Figure 2.3a shows the corresponding predicted bathymetry along the equator for the same timestep of the "Modern" model shown in Figure 2.2a. Similarly, Figure 2.3b,c show the bathymetric depth along the equator for the same timestep of the "Archean" and "Hadean" models shown in Figure 2.2b,c. The

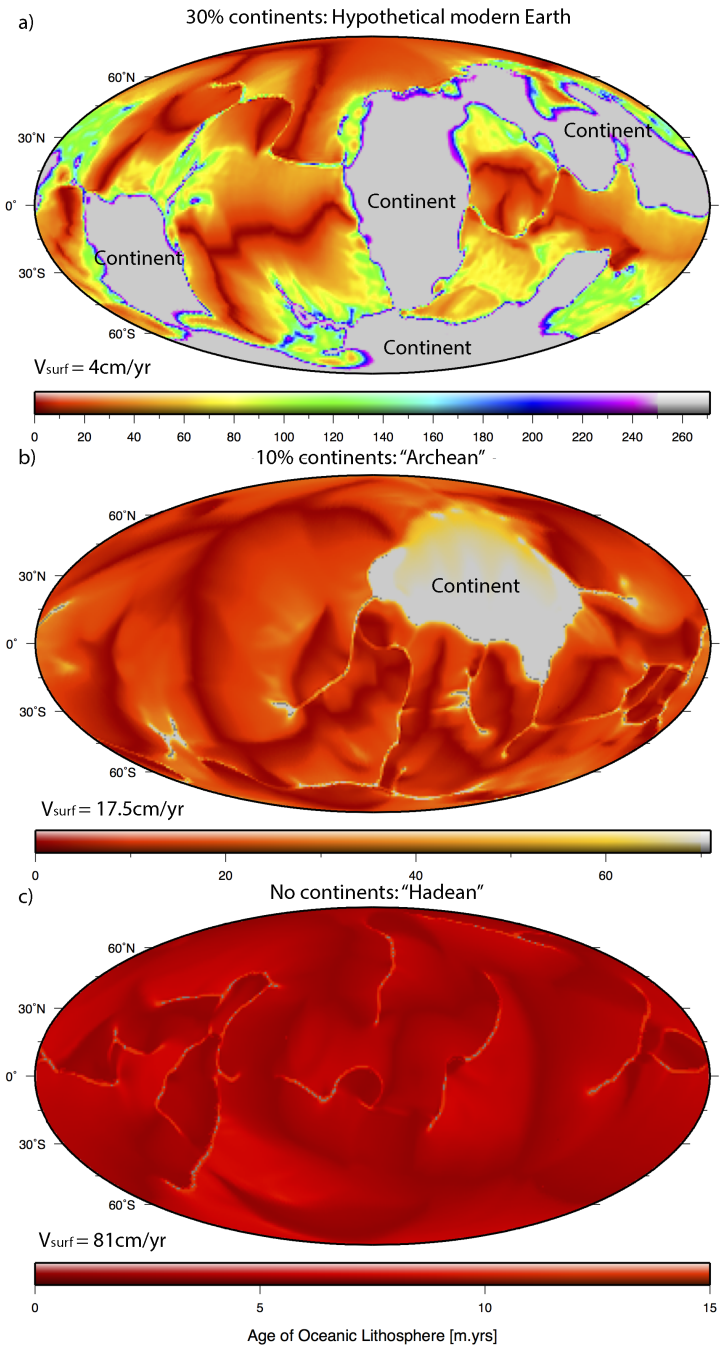


**Figure 2.2**: Synthetic seafloor age maps for representative timesteps from models with (a) 30% continent, (b) 10% continent and (c) 0% continent (continents in grey). Ages of oceanic crust are defined independently for each model (see colorbars) based upon the corresponding surface velocity (above colorbar, leftside).

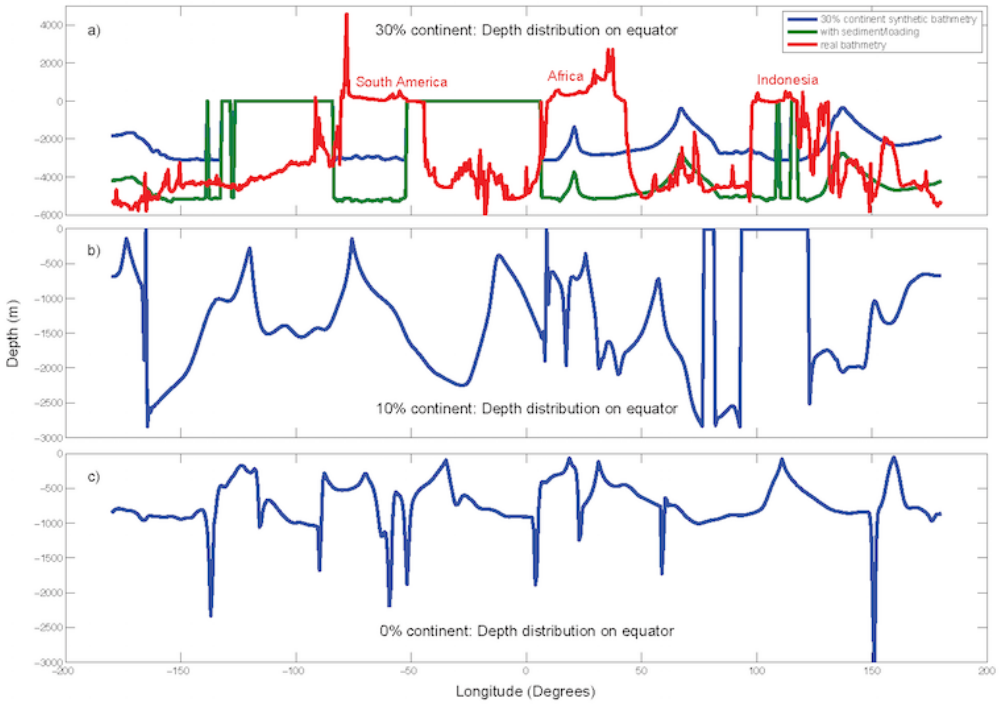


**Figure 2.3**: Bathymetric profiles (in blue) along equator of corresponding maps shown in Figure 1 for (a) 30% continent, (b) 10% continent and (c) 30% continent using a plate cooling model (*Hasterok*, 2013) and tying MOR crest to 0 m (note different y-axes). Depth of 30% continent model corrected for loading with modern day ocean volume and sediments (green curve; see Methods for details) compared to Earth's bathymetry along equator (red curve) with continents labeled.

predicted bathymetry for the "Archean" and "Hadean" cases show a progressive shallowing of ocean basins and decrease in ridge-basin offset with increasing Ra (Fig 2.3b-c).

In order to make a better comparison between the bathymetry of the "Modern" case and the present-day Earth, certain adjustments need to be made. We estimate the current MOR depth for Earth using the age-area distribution of oceanic plates based upon reconstructed oceanic plate age from 140 Myr to present (*Müller et al.*, 2008), accounting for ice sheets, large igneous provinces and sediments which make significant contributions to ocean floor bathymetry (*Müller et al.*, 2008). To account for sediment loading, we first obtain the amount of sediments using modern day sediment model based on NGDC (*Divins*, 2003). It gives us sediment

thickness based on oceanic plate age and latitude. With the calculated sediment thickness, we use *Le Douaran and Parsons* (1982) model for sediment loading. This introduces a downshift in depth as expected due to isostasy from the increase loading. After accounting for these using a sediment loading model (*Müller et al.*, 2008) and airy isostasy model (*Le Douaran and Parsons*, 1982), the predicted bathymetry (Fig. 2.3a, green line) shifts ∼2 km deeper and compares favorably with actual depths of ridges and basins (Fig. 2.3a, red line, $70°E$).

Previous attempts to consider the geologic evolution of global sea level focus around the observation that continental freeboard (elevation of continents with respect to sea level) has remained approximately constant (±200 m) possibly since the Archaean (*Wise*, 1974) and most data is available for the last 500 Myr (*Miller et al.*, 2005). This has been viewed as a constraint on continental growth models (*Schubert and Reymer*, 1985), although more recently it has been argued this observation can be reconciled with the entire spectrum of growth models that have been proposed (*Harrison*, 2009). Of course, any relation between freeboard and continental growth depends upon assumptions made regarding ocean basin volume over time as well as the total volume of water. Similarly, the extent of continental inundation is strongly dependent on the choice of hypsometry model used to represent a statistical average of continental topography (*Flament et al.*, 2008). However, the total volume of water above any submerged continental shelf, or that above entirely submerged continents, is negligible in compared to the ocean volume and therefore not accounted for in our models (*Miller et al.*, 2005). Previous work suggests the continents were entirely submerged well into the Archean (*Vlaar*, 2000; *Flament et al.*, 2008), and that inundation of continents subsequent to their emergence is not significant compared to other sources of uncertainty (*Miller et al.*, 2005).

### 2.4.3 Variations of ocean volume

In Figure 2.4a, we plot our results of MOR crest depth variations in the "Modern", "Archean" and "Hadean" models (blue, green and red respectively) in units of transit times. The MOR depth variations for the "Modern" model with

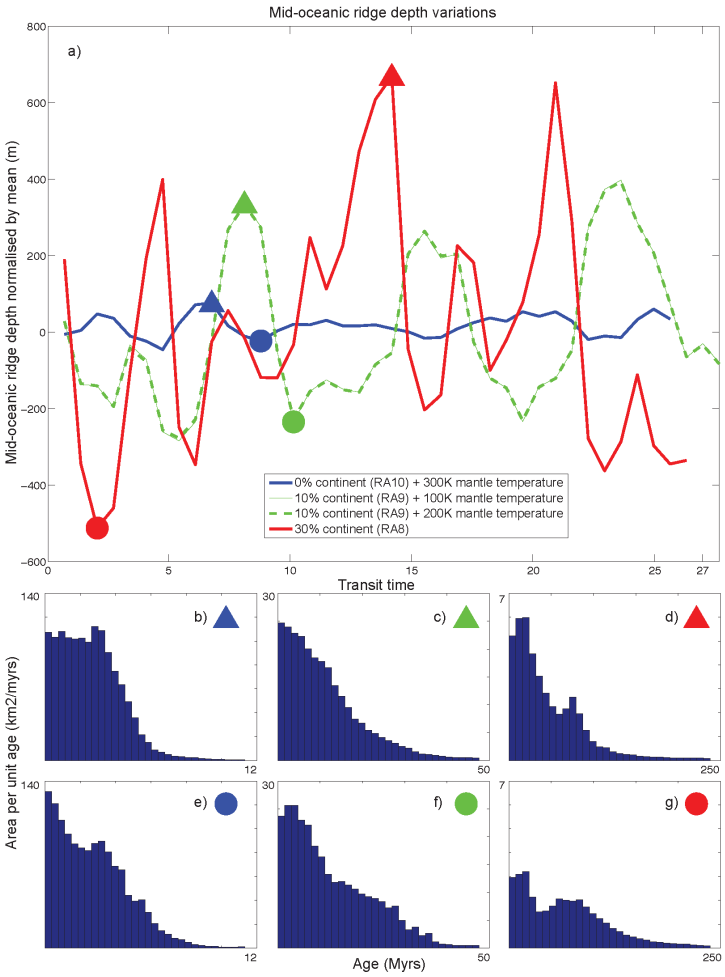


**Figure 2.4**: (a) MOR depth based on synthetic seafloor age distributions with 30% (red), 10% (green), and 0% (blue) continents, $Ra \sim 10^8$, $10^9$ and $10^{10}$ respectively, normalized by the mean over 27 transit times, corresponding to 2000, 440, and 100 Myr, respectively. For models with 0% and 10% continents that represent earlier periods of Earth history when the mantle may have been hotter, mantle convection models themselves do not include the temperature increase but variable levels of increased mantle temperature are considered when calculating ocean bathymetry by adjusting the plate cooling model appropriately (as discussed in text). (b-g) Seafloor age distributions corresponding to minima (circles) and maxima (triangles) MOR depths (note different x and y axes for each distribution).

values ranging from ±100 m to ±900 m, bracketing the range observed in previous models (*Coltice et al.*, 2014), are an order of magnitude larger than that of ±50m for the "Hadean" model. This is expected since on average the age of subducting oceanic crust is older for the "Modern" model. Transitions between minima and

maxima (circles and triangles in Fig 2.4a) increase with continental area, from ~12 Myr for the 0% continent ($Ra \sim 10^{10}$) model compared to ~250 Myr for the "Modern" model. Corresponding histograms of age-area distributions for MOR depths maxima (Figure 2.4b-d) have a higher proportion of younger crust (thus less subsidence and smaller ocean basin volume) leading to higher sea level while distributions for MOR depths minima (Figure 2.4e-g) have a higher proportion of older crust representing larger and deeper ocean basins.

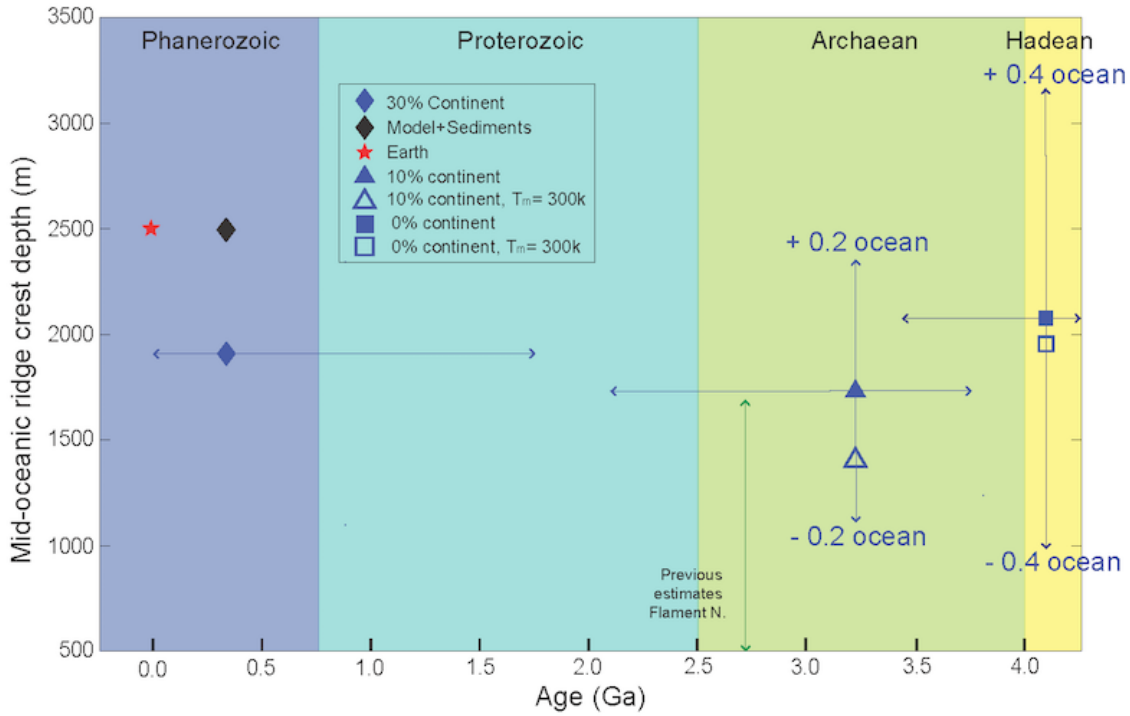


**Figure 2.5**: (a) Mean MOR depth based on synthetic seafloor age distributions with 30% (diamonds), 10% (triangles), and 0% (squares) continents with varying mantle temperatures, and sediment loading compared to actual value for Earth (red star). For models with 0% and 10% continents, bathymetry accounts for increased mantle temperature by adjusting the plate cooling model appropriately. Uncertainty in past ocean volume for models with 0% and 10% continents is shown (light blue lines) as ±40% and ±20%, respectively. (b) Major contributions to global sea level for a range of timescales (after *Miller et al.* (2005)).

In Figure 2.5, we show the mean of all time steps for each model. For the "Modern" model, the mean MOR crest depth is 1900 m (blue diamond) but after correcting for sediment loading, the predicted MOR depth (black diamond) agrees

favorably with the observed MOR depth (red star) of ∼2500 m. The predicted MOR depths for "Archean" and "Hadean" models are 1700 m and 2100 m, respectively, only modestly below the present day depth. Variable levels of temperature increase in the mantle affects the oceanic plate bathymetry and we reflect that by adjusting $\Delta T$ in the coefficient of the plate cooling model which effects the degree of seafloor subsidence (*Davies*, 1999). The Archean mantle is considered to be $100 - 300°C$ warmer than today based on Archaean-aged high magnesium komatiites (*Herzberg et al.*, 2010). When a range of warmer mantle temperatures (100-300°C) are considered for a posterior calculations of seafloor bathymetry, the MOR depths in models with 10% ($Ra \sim 10^9$) and 0% ($Ra \sim 10^{10}$) continents become about 10-20% shallower. The reference temperature in the mantle of the convection models is the same for all cases including the "Archean" and "Hadean" models. Thus, the increases in the Ra due to lowered mantle viscosities associated with warmer mantle temperatures have already been accounted for.

## 2.5 Discussion

The presumption that plate tectonics, or an earlier form of it, was operating during early Earth and persisted throughout Earth's history is debatable. Plate tectonics, sensu stricto, is a kinematic description of a set of rigid plates with boundaries defined by MORs, single-sided asymmetric subduction zones, and transform faults. In regard to early Earth, a broader definition of plate tectonics could encompass a wider spectrum of plate boundary archetypes at zones of convergence and divergence that exhibit deformation over broader regions, and yet generate equivalent geological and geochemical signals. An example from the Hadean are thermobarometric analyses of mineral inclusions within the Jackhill zircons that indicate prograde melting within a low geothermal gradient and water saturated conditions (*Hopkins et al.*, 2008). These observations are interpreted as evidence that the zircons crystallized within the overlying wedge of an underthrust environment, reminiscent of convergent margin tectonics and perhaps capable of recycling crust into the mantle. Similarly, the Isua supracrustal belt in Greenland could preserve Earth's oldest ophiolite and oceanic crust, suggesting that seafloor

spreading was operating ∼3.8 Ga (*Furnes et al.*, 2007). The choices for our models reflect continuous resurfacing of the Earth's surface without reference to a specific manifestation of convergence and divergence, which is compatible with the available evidence. Hydrothermal alteration of oceanic crust generates isotopic signatures that reflect the chemistry of the seawater, including enrichment of Uranium (sourced from eroded continental crust) relative to Thorium. Thus continuously submerged MORs since the Archean are necessary to support current interpretations that ocean island basalts are sampling ancient (<2 Ga) altered oceanic crust that was recycled deep into Earth's mantle.

We present models with 10% ($Ra \sim 10^9$) and 0% ($Ra \sim 10^{10}$) of Earth's surface area covered by continents that approximately represent the Hadean and Archean eons, respectively, in agreement with the vast majority of proposed crustal growth models (*Harrison*, 2009). However, estimating the volume of continental crust through time is hindered by preservation issues and also depends greatly on assumptions of rates of crustal production and erosion. There is evidence from Hadean-aged detrital zircons that suggest the existence of continental crust in that eon. It may have been volumetrically important but only trace amounts of such zircons have been preserved (*Harrison*, 2009). Similarly, episodic crustal growth and collisional events may lead to preferential preservation of Archean rocks, a possibility that many crustal growth models neglect(*Hawkesworth et al.*, 2010). The hypothesis that between 70%-100% of the present volume of continental crust was established by the end of the Archean, and has been in a steady-state since then is largely based on the coincidence that modern rates of crustal generation and destruction along subduction zones are similar in magnitude (but both rates also have large uncertainties) (*Hawkesworth et al.*, 2010). Thus, rather than simply associating an amount of continental crust with specific time periods such as the Hadean and Archean, we considered a wider range of scenarios for each of the 0%, 10%, and 30% continents models by varying mantle temperature for each.

Previous attempts to consider the geologic evolution of global sea level focus around the observation that continental freeboard (elevation of continents with respect to sea level) has remained approximately constant (±200 m) for the past

600Ma (*Worsley et al.*, 1984; *Schubert and Reymer*, 1985) extending to the beginning of the Proterozoic (*Wise*, 1974; *Eriksson*, 1999; *Eriksson et al.*, 2006). (*Conrad*, 2013) provides a wonderful summary of contributions to sea level at different time scales. Large-scale and long term changes in sea level can be due to changes in ocean basin volume such as varying distribution of ages of global oceanic crust (*Harrison*, 1990; *Worsley et al.*, 1984) while others suggest tectonism such as accreting continents (*Worsley et al.*, 1984; *Eriksson*, 1999), isostasy, sediment supply etc (*Eriksson*, 1999). This has been viewed as a constraint on continental growth models(*Schubert and Reymer*, 1985), although more recently it has been argued this observation can be reconciled with the entire spectrum of growth models that have been proposed(*Harrison*, 2009). Of course, any relation between freeboard and continental growth depends upon assumptions made regarding ocean basin volume over time as well as the total volume of water, which we discuss later. These continental freeboard studies look at sea level from the perspective of continents for Phanerozoic (some extending to Proterozoic), while our study explores sea level from the perspective of MOR depths since the beginning of Earth. While there may be evidence for constant continental freeboard in both Phanerozoic and Proterozoic, it is unclear that continental freeboard is constant in Hadaean and Archaean especially with the range of continental growth models. Both perspectives considers volume of ocean basin, amount of total water in the oceans, continental accretion and sediment supply. We also have to consider the growth of continents over all of Earth's evolution and the absence of continental hypsometry. These make the perspective of MOR depths a natural candidate with such considerations.

The total ocean volume present throughout Earth's history is unknown, but several lines of evidence suggest a terrestrial hydrosphere was already present during the Hadean (*Harrison*, 2009). The volume of oceans on the surface is determined by the mantle degassing and regassing throughout Earth's history (*McGovern and Schubert*, 1989). Here, we consider the amount of water exchanged between the deep mantle and hydrosphere from the Hadean to the present day. The current rate of water being subducted back into the mantle is $3.2 \times 10^{17}$ kg/

Myr (*van Keken et al.*, 2011) while the output rate at MOR is about $2 \times 10^{17}$ kg/ Myr (*Hirschmann and Kohlstedt*, 2012), giving a net regassing of the mantle of $1.2 \times 10^{8}$ Tg/ Myr within the range of 1 $3 \times 10^{17}$ kg/ Myr proposed by *Korenaga* (2011). Based on backwards extrapolation using present rates, there would be a net loss of $5.5 \times 10^{20}$ kg of water, or 0.4 oceans, into the mantle since 4.5 Ga as indicated by the vertical error bars for the "Hadean" model in Figure 2.5. However, models of slab dehydration indicate that the only water that gets carried into the deep mantle is via old, nearly vertical dipping slabs with the fastest subduction velocities (*van Keken et al.*, 2011). Thus, younger and more slowly subducting slabs, as expected for early Earth, would experience more efficient slab dehydration and imply much lower rates of delivering water to the deep mantle. Secondly, the rate that water gets exsolved out of MORs would not only be larger for early Earth due to faster spreading rates but also larger amount of MORs. The combination of these effects leads to a net gain of water by the ocean over time to hit a peak surface water volume during early Earth, which may more appropriately characterize the early Earth's deep water cycle in contrast to the net loss of water over time observed for today.

To place our models into context, we consider a range of $\pm 40\%$ and $\pm 20\%$ oceans for the Hadean and Archaen, respectively, in regard to our estimates of the time-averaged MOR depth (Figure 2.5). Other workers have reported that the Earth started out with about the same amount or more water on the surface based on various models (*Crowley et al.*, 2011; *Sandu et al.*, 2011; *Korenaga*, 2011). While it is important to note that there is a clear tradeoff between the amount of ocean water and depth of MOR depths in order to maintain constant continental freeboard (*Korenaga*, 2011), as discussed previously, constant continental freeboard is not well established in Archaean or Hadean. Isotopic compositions of serpentines argue the Archean Earth had up to 26% more ocean (*Pope et al.*, 2012), which is consistent with the analysis that the balance of fluxes changed from positive to negative at a subsequent point. Sedimentary studies show that sea-level changes between 2.7 Ga and 2.0 are close to those at present-day in several cratons (*Eriksson et al.*, 1999) thus suggesting that the ocean was not substantially larger

in volume at this time. The oldest inconformity is about 3.4 Ga in Australia (*Buick et al.*, 1995), suggesting that there was not one or two ocean more than today. It is also important to consider that starting off with a much larger ocean volume, one would have to invoke a process to quickly remove the excess water to get to the volume observed throughout Archaean, Proterozoic and Phanerozoic.

In our results, we have not taken into consideration how oceanic crust in the Hadean and Archaean might be different from today (*Kemp et al.*, 2010; *Darling et al.*, 2009; *Harrison*, 2009). There is evidence for Hadean crust to be more mafic than modern day oceanic crust (*Darling et al.*, 2009). *Arndt* (1983) suggest that dense komatiites were able to subduct Archaean oceanic crust and that the crustal thickness then was not much greater than today. *Galer* (1991) suggest that thicker oceanic crust in the past due to greater depth of melting would lead to lower continental freeboard due to isostatic uplift of the basalt. The presence and kinetics of the basalt-eclogite transition is not considered here. Our assumption for the early Earth scenario considered is that some form of mobile-lid convection is operating in a way to continually recycle the surface of the Earth and that the basalt-eclogite transition, while possibly important for several reasons, does not provide a barrier to the overall process of recycling the lithosphere.

Our sediment calculation is based purely on the model from *Müller et al.* (2008) to predict sediments on the ocean floor given the age and latitude. The model is based on modern day observations (*Divins*, 2003). Here we note that more recent sediment models (*Conrad*, 2013; *Goswami et al.*, 2015) give a smaller estimate for sediment impact taking into account oceans basins with passive vs active margins and thus would lie between our model with no sediments and our sediment loaded model . Overall, the sediment model we use is sufficient as it is able to first order capture the sediment loading impact. One of the major contributions to ocean floor sediments is the pelagic fallout of organisms in the eutrophic zone (*Emerson and Hedges*, 1988). The Great Oxidation Event (GOE) (*Holland*, 2006) at 2.5 Ga allowed efficient carbon fixing, hence increasing organic matters in the eutrophic zone, leading to high burial rates in the still anoxic sea floor (*Kendall et al.*, 2010; *Knoll*, 2014). This is followed by a gradual oxidation of the ocean

towards greater depths, thus allowing bacterial to consume sinking organic matter and as a result, decreasing burial rates (*Knoll*, 2014; *Fike et al.*, 2006). The end of Proterozoic and beginning of Cambrian saw the gradual rise of burrowing animals, which consume organic sediments on the sea floor and recycle them back into the water column (*Knoll*, 2014). Thus the overall trend for this source is an initial increase around 2.5 Ga and gradual decrease until the levels we see today.

Sedimentation in the deep ocean includes banded iron formation (BIFs) and chert formation during Archean through the Proterozoic (*Bjerrum and Canfield*, 2002; *van den Boorn et al.*, 2007). Although Protezoroic oceans are thought to be anoxic (*Anbar and Knoll*, 2002; *Lyons et al.*, 2009) and thus lacking in oxygenic photosynthesis, anoxygenic photosynthesis can still contribute to primary production in the ocean (*Manske et al.*, 2005) leading to deposition in the deep ocean as chert. Similarly in the Archean, chert as a source of ocean sediments was more significant compare to BIFs but it was confined to shallow inland seas and continental shelves (*van den Boorn et al.*, 2007) compared to Proterozoic when anoxygenic photoautotrophs seem more abundant in the deep ocean (*Johnston et al.*, 2009). For the purpose of this paper, we acknowledge such sources but focus on Archean where the sedimentations from such sources is less significant.

Another major contribution to ocean floor sediments is riverine sediments (*Milliman and Farnsworth*, 2013; *Emerson and Hedges*, 1988). For long time scales, this source depends on how much continents are available as sediment source, the maturity of riverine systems coupled with evolution of flora and fauna and the processes of weathering and erosion etc (*Milliman and Farnsworth*, 2013). How the evolution of flora and fauna is beyond the scope of this study along with the processes of weathering and erosion. For this study, we focus on the amount of continents available as sediment source. Since we assume that continents are growing over time, this would mean that sediments from continents are proportionately increasing over time, an opposite trend from the organic matter source.

## 2.6 Conclusion

We quantify the magnitude and variation of the main drivers of global MOR depth for a range of conditions that span the time equivalent to Earth history, thus making our results relevant to the Hadean waterworld hypothesis (*Harrison*, 2009). Within the limits of the assumptions made for our models, the results favor the scenario that MORs were continuously submerged (perhaps to depths not far from today) during the Archaean and Hadean, potentially providing hydrothermal environments conducive for life to originate. We show that the largest contributors to global MOR depths in the early Earth are growing continents decreasing ocean basin surface area and slowing plate speeds resulting in deepening ocean basins, in agreement with previous studies (*Flament et al.*, 2008; *Schubert and Reymer*, 1985), along with the amount of water on the surface of the Earth. To first order these effects compensate each other throughout the Hadean and Archean, leading to continuously submerged MOR and potentially quasi-static MOR depths. These models also inform us about the long term variations in ocean depth due to global tectonic processes Our 30% continent with $Ra \sim 10^9$ models suggest large variations ($\pm$500 m) of MOR depth are both a phenomena confined to the Phanerozoic and relatively uncommon with a typical period of $\sim$250 Ma. Moreover, the large transgressions/regressions on continents well-known in the past 140 Ma of Earth history are similar in both amplitude and frequency to the variations in MOR depth observed in our model. Such variations were smaller in the early Earth, only 50% and 10% when covered by 10% ($Ra \sim 10^9$) and 0% ($Ra \sim 10^{10}$) continents, respectively. The total volume of water on the Earth's surface may not have changed more than 0.4 oceans since the Hadean, and that the possibility exists there was a time in the Archean or Proterozoic when Earth's oceans experienced a peak water volume. While Earth's deep water cycle is likely currently in a state of net loss of water into the mantle, the equivalent budget for the early Earth was likely in a state of net gain, with positive fluxes from MORs dominating the fluxes back into the mantle via subduction. The subject of the environments for the emergence of life is a highly debated one and we highlight one potential candidate in this paper, namely hydrothermal vents at MOR (*Nisbet and Sleep*, 2001). With

our results, we show that MORs were continuously submerged and that the depths could have remained unchanged through geologic time. The importance of the unchanged MOR depths lies in the maximum hydrothermal penetration depths as the current average MOR depths gives us the maximum hydrothermal penetration depths (*Kasting et al.*, 2006). Assuming that increasing the hydrothermal depth gives more heat, elemental and ionic exchange, this will then result in a larger disequilibrium in energy that early life is proposed to take advantage of (*Nisbet and Sleep*, 2001).

Chapter 2, is a full reprint of the material as it appears in Gcubed 2016. Shi Sim, Dave R Stegman and Nicolas Coltice, "Effects of continental growth on mid-oceanic ridge depths", *Gcubed*, 2016. The dissertation/thesis author was the primary investigator and author of this paper. I would like to acknowledge my co-authors, Dave R. Stegman and Nicolas Coltice.

# References


Anbar, A. D., and A. Knoll (2002), Proterozoic ocean chemistry and evolution: a bioinorganic bridge?, *science*, *297*(5584), 1137–1142.

Arndt, N. T. (1983), Role of a thin, komatiite-rich oceanic crust in the archean plate-tectonic process, *Geology*, *11*(7), 372–375.

Bello, L., N. Coltice, P. J. Tackley, R. D. Müller, and J. Cannon (2015), Assessing the role of slab rheology in coupled plate-mantle convection models, *Earth and Planetary Science Letters*, *430*, 191–201.

Bjerrum, C. J., and D. E. Canfield (2002), Ocean productivity before about 1.9 gyr ago limited by phosphorus adsorption onto iron oxides, *Nature*, *417*(6885), 159–162.

Buick, R., J. Thornett, N. McNaughton, J. Smith, M. Barley, and M. Savage (1995), Record of emergent continental crust 3.5 billion years ago in the pilbara craton of australia, *Nature*, *375*(6532), 574–577.

Coltice, N., T. Rolf, P. J. Tackley, and S. Labrosse (2012), Dynamic Causes of the Relation Between Area and Age of the Ocean Floor, *Science*, *336*(6079), 335–338.

Coltice, N., T. Rolf, and P. J. Tackley (2014), Seafloor spreading evolution in response to continental growth, *Geology*, *42*(3), 235–238.

Conrad, C. P. (2013), The solid earth's influence on sea level, *Geological Society of America Bulletin*, *125*(7-8), 1027–1052.

Crowley, J. W., M. Gérault, and R. J. O'Connell (2011), On the relative influence of heat and water transport on planetary dynamics, *Earth and Planetary Science Letters*, *310*(3), 380–388.

Darling, J., C. Storey, and C. Hawkesworth (2009), Impact melt sheet zircons and their implications for the hadean crust, *Geology*, *37*(10), 927–930.

Davies, G. F. (1999), *Dynamic Earth: Plates, plumes and mantle convection*, Cambridge University Press.

Debaille, V., C. O'Neill, A. D. Brandon, P. Haenecour, Q.-Z. Yin, N. Mattielli, and A. H. Treiman (2013), Stagnant-lid tectonics in early Earth revealed by 142Nd variations in late Archean rocks, *Earth and Planetary Science Letters*, *373*, 83–92.

Divins, D. (2003), Total Sediment Thickness of the World's Oceans & Marginal Seas, *NOAA National Geophysical Data Center, Boulder, CO*.

Eakins, B., and G. Sharman (2010), Volumes of the world's oceans from ETOPO1, *NOAA National Geophysical Data Center, Boulder, CO, USA*.

Emerson, S., and J. Hedges (1988), Processes controlling the organic carbon content of open ocean sediments, *Paleoceanography*, *3*(5), 621–634.

Eriksson, P. (1999), Sea level changes and the continental freeboard concept: general principles and application to the precambrian, *Precambrian Research*, *97*(3), 143–154.

Eriksson, P., R. Mazumder, S. Sarkar, P. Bose, W. Altermann, and R. Van der Merwe (1999), The 2.7–2.0 ga volcano-sedimentary record of africa, india and australia: evidence for global and local changes in sea level and continental freeboard, *Precambrian Research*, *97*(3), 269–302.

Eriksson, P. G., R. Mazumder, O. Catuneanu, A. J. Bumby, and B. O. Ilondo (2006), Precambrian continental freeboard and geological evolution: a time perspective, *Earth-Science Reviews*, *79*(3), 165–204.

Fike, D., J. Grotzinger, L. Pratt, and R. Summons (2006), Oxidation of the ediacaran ocean, *Nature*, *444*(7120), 744–747.

Flament, N., N. Coltice, and P. F. Rey (2008), A case for late-archaean continental emergence from thermal evolution models and hypsometry, *Earth and Planetary Science Letters*, *275*(3), 326–336.

Flament, N., P. F. Rey, N. Coltice, G. Dromart, and N. Olivier (2011), Lower crustal flow kept archean continental flood basalts at sea level, *Geology*, *39*(12), 1159–1162.

Furnes, H., M. de Wit, H. Staudigel, M. Rosing, and K. Muehlenbachs (2007), A Vestige of Earth's Oldest Ophiolite, *Science*, *315*(5819), 1704–1707.

Galer, S. (1991), Interrelationships between continental freeboard, tectonics and mantle temperature, *Earth and Planetary Science Letters*, *105*(1-3), 214–228.

Gerya, T. V., J. A. D. Connolly, and D. A. Yuen (2008), Why is terrestrial subduction one-sided?, *Geology*, *36*(1), 43.

Goswami, A., P. Olson, L. Hinnov, and A. Gnanadesikan (2015), Oesbathy version 1.0: a method for reconstructing ocean bathymetry with generalized continental shelf-slope-rise structures, *Geoscientific Model Development*, *8*(9), 2735–2748.

Hacker, B. R. (2008), H2o subduction beyond arcs, *Geochemistry, Geophysics, Geosystems*, *9*(3).

Harrison, C. (1990), Long-term eustasy and epeirogeny in continents, *Sea-level change*, pp. 141–158.

Harrison, T. M. (2009), The Hadean Crust: Evidence from $>$ 4 Ga Zircons, *Annual Review of Earth and Planetary Sciences*, *37*(1), 479–505.

Hasterok, D. (2013), Global patterns and vigor of ventilated hydrothermal circulation through young seafloor, *Earth and Planetary Science Letters*, *361*(c), 34–43.

Hawkesworth, C. J., B. Dhuime, A. B. Pietranik, P. A. Cawood, A. I. S. Kemp, and C. D. Storey (2010), The generation and evolution of the continental crust, *Journal of the Geological Society*, *167*(2), 229–248.

Herzberg, C., K. Condie, and J. Korenaga (2010), Thermal history of the Earth and its petrological expression, *Earth and Planetary Science Letters*, *292*(1-2), 79–88.

Hirschmann, M., and D. Kohlstedt (2012), Water in Earth's mantle, *Physics Today*, *65*(3), 40–45.

Holland, H. D. (2006), The oxygenation of the atmosphere and oceans, *Philosophical Transactions of the Royal Society B: Biological Sciences*, *361*(1470), 903–915.

Höning, D., and T. Spohn (2016), Continental growth and mantle hydration as intertwined feedback cycles in the thermal evolution of earth, *Physics of the Earth and Planetary Interiors*, *255*, 27–49.

Hopkins, M., T. M. Harrison, and C. E. Manning (2008), Low heat flow inferred from > 4Gyr zircons suggests Hadean plate boundary interactions, *Nature*, *456*(7221), 493–496.

Jarrard, R. D. (2003), Subduction fluxes of water, carbon dioxide, chlorine, and potassium, *Geochemistry, Geophysics, Geosystems*, *4*(5).

Jaupart, C., S. Labrosse, and J. Mareschal (2007), 7.06-temperatures, heat and energy in the mantle of the earth, *Treatise on geophysics*, pp. 253–303.

Johnson, T. E., M. Brown, B. J. Kaus, and J. A. VanTongeren (2014), Delamination and recycling of archaean crust caused by gravitational instabilities, *Nature Geoscience*, *7*(1), 47–52.

Johnston, D. T., F. Wolfe-Simon, A. Pearson, and A. H. Knoll (2009), Anoxygenic photosynthesis modulated proterozoic oxygen and sustained earth's middle age, *Proceedings of the National Academy of Sciences*, *106*(40), 16,925–16,929.

Karato, S.-I., and H. Jung (2003), Effects of pressure on high-temperature dislocation creep in olivine, *Philosophical Magazine*, *83*(3), 401–414.

Kasting, J. F., M. T. Howard, K. Wallmann, J. Veizer, G. Shields, and J. Jaffrés (2006), Paleoclimates, ocean depth, and the oxygen isotopic composition of seawater, *Earth and Planetary Science Letters*, *252*(1), 82–93.

Kemp, A., S. Wilde, C. Hawkesworth, C. Coath, A. Nemchin, R. Pidgeon, J. Vervoort, and S. DuFrane (2010), Hadean crustal evolution revisited: new constraints from pb–hf isotope systematics of the jack hills zircons, *Earth and Planetary Science Letters*, *296*(1), 45–56.

Kendall, B., C. T. Reinhard, T. W. Lyons, A. J. Kaufman, S. W. Poulton, and A. D. Anbar (2010), Pervasive oxygenation along late archaean ocean margins, *Nature Geoscience*, *3*(9), 647–652.

Knoll, A. H. (2014), Paleobiological perspectives on early eukaryotic evolution, *Cold Spring Harbor perspectives in biology*, *6*(1), a016,121.

Korenaga, J. (2011), Thermal evolution with a hydrating mantle and the initiation of plate tectonics in the early earth, *Journal of Geophysical Research: Solid Earth*, *116*(B12).

Labrosse, S., and C. Jaupart (2007), Thermal evolution of the Earth: Secular changes and fluctuations of plate characteristics, *Earth and Planetary Science Letters*, *260*(3-4), 465–481.

Le Douaran, S., and B. Parsons (1982), A note on the correction of ocean floor depths for sediment loading, *Journal of Geophysical Research: Solid Earth (1978–2012)*, *87*(B6), 4715–4722.

Loyd, S., T. Becker, C. Conrad, C. Lithgow-Bertelloni, and F. Corsetti (2007), Time variability in cenozoic reconstructions of mantle heat flow: Plate tectonic cycles and implications for earth's thermal evolution, *Proceedings of the National Academy of Sciences*, *104*(36), 14,266–14,271.

Lyons, T. W., A. D. Anbar, S. Severmann, C. Scott, and B. C. Gill (2009), Tracking euxinia in the ancient ocean: a multiproxy perspective and proterozoic case study, *Annual Review of Earth and Planetary Sciences*, *37*, 507–534.

Manning, C. E. (2004), The chemistry of subduction-zone fluids, *Earth and Planetary Science Letters*, *223*(1), 1–16.

Manske, A. K., J. Glaeser, M. M. Kuypers, and J. Overmann (2005), Physiology and phylogeny of green sulfur bacteria forming a monospecific phototrophic assemblage at a depth of 100 meters in the black sea, *Applied and environmental microbiology*, *71*(12), 8049–8060.

McGovern, P. J., and G. Schubert (1989), Thermal evolution of the earth: effects of volatile exchange between atmosphere and interior, *Earth and Planetary Science Letters*, *96*(1), 27–37.

McKenzie, D., J. Jackson, and K. Priestley (2005), Thermal structure of oceanic and continental lithosphere, *Earth and Planetary Science Letters*, *233*(3), 337–349.

Mei, S., and D. Kohlstedt (2000), Influence of water on plastic deformation of olivine aggregates: 2. dislocation creep regime, *Journal of Geophysical Research: Solid Earth*, *105*(B9), 21,471–21,481.

Miller, K. G., M. A. Kominz, J. V. Browning, J. D. Wright, G. S. Mountain, M. E. Katz, P. J. Sugarman, B. S. Cramer, N. Christie-Blick, and S. F. Pekar (2005), The phanerozoic record of global sea-level change, *Science*, *310*(5752), 1293–1298.

Milliman, J. D., and K. L. Farnsworth (2013), *River discharge to the coastal ocean: a global synthesis*, Cambridge University Press.

Moore, W. B., and A. A. G. Webb (2013), Heat-pipe earth, *Nature*, *501*(7468), 501–505.

Müller, R. D., M. Sdrolias, C. Gaina, B. Steinberger, and C. Heine (2008), Long-Term Sea-Level Fluctuations Driven by Ocean Basin Dynamics, *Science*, *319*(5868), 1357–1362.

Nisbet, E. G., and N. H. Sleep (2001), The habitat and nature of early life, *Nature*, *409*(6823), 1083–1091.

O'Neill, C., and V. Debaille (2014), The evolution of hadean–eoarchaean geodynamics, *Earth and Planetary Science Letters*, *406*, 49–58.

Plank, T., and C. H. Langmuir (1993), Tracing trace elements from sediment input to volcanic output at subduction zones, *Nature*, *362*(6422), 739–743.

Plank, T., L. B. Cooper, and C. E. Manning (2009), Emerging geothermometers for estimating slab surface temperatures, *Nature Geoscience*, *2*(9), 611–615.

Pope, E. C., D. K. Bird, and M. T. Rosing (2012), Isotope composition and volume of Earth's early oceans, *Proceedings of the National Academy of Sciences*, *109*(12), 4371–4376.

Rolf, T., and P. Tackley (2011), Focussing of stress by continents in 3d spherical mantle convection with self-consistent plate tectonics, *Geophysical Research Letters*, *38*(18).

Sandu, C., A. Lenardic, and P. McGovern (2011), The effects of deep water cycling on planetary thermal evolution, *Journal of Geophysical Research: Solid Earth*, *116*(B12).

Schubert, G., and A. P. S. Reymer (1985), Continental volume and freeboard through geological time, *Nature*, *316*(6026), 336–339.

Sizova, E., T. Gerya, M. Brown, and L. Perchuk (2010), Subduction styles in the precambrian: insight from numerical experiments, *Lithos*, *116*(3), 209–229.

Sleep, N. H., K. Zahnle, and P. S. Neuhoff (2001), Initiation of clement surface conditions on the earliest Earth, *Proceedings of the National Academy of Sciences*, *98*(7), 3666–3672.

Staudigel, H. (2014), Chemical fluxes from hydrothermal alteration of the oceanic crust, *Treatise on Geochemistry*, *3*, 583–606.

Staudigel, H., B. Tebo, A. Yayanos, H. Furnes, K. Kelley, T. Plank, and K. Muehlenbachs (2004), The oceanic crust as a bioreactor, *The Subseafloor Biosphere at Mid-Ocean Ridges*, pp. 325–341.

Stein, C. A., and S. Stein (1992), A model for the global variation in oceanic depth and heat flow with lithospheric age, *Nature*, *359*(6391), 123–129.

Tackley, P. J. (2008), Modelling compressible mantle convection with large viscosity contrasts in a three-dimensional spherical shell using the yin-yang grid, *Physics of the Earth and Planetary Interiors*, *171*(1), 7–18.

Valley, J. W., W. H. Peck, E. M. King, and S. A. Wilde (2002), A cool early Earth, *Geology*, *30*(4), 351.

van den Boorn, S. H., M. J. van Bergen, W. Nijman, and P. Z. Vroon (2007), Dual role of seawater and hydrothermal fluids in early archean chert formation: evidence from silicon isotopes, *Geology*, *35*(10), 939–942.

Van Hunen, J., and J.-F. Moyen (2012), Archean subduction: fact or fiction?, *Annual Review of Earth and Planetary Sciences*, *40*, 195–219.

van Keken, P. E., B. R. Hacker, E. M. Syracuse, and G. A. Abers (2011), Subduction factory: 4. Depth dependent flux of $H_2O$ from subducting slabs worldwide, *Journal of Geophysical Research: Solid Earth*, *116*(B1).

Vlaar, N. J. (2000), Continental emergence and growth on a cooling earth, *Tectonophysics*, *322*(1-2), 191–202.

Wise, D. U. (1974), Continental margins, freeboard and the volumes of continents and oceans through time, in *The Geology of Continental Margins*, edited by C. Burk and C. Drake, pp. 45–58, Springer.

Worsley, T. R., D. Nance, and J. B. Moody (1984), Global tectonics and eustasy for the past 2 billion years, *Marine Geology*, *58*(3), 373–400.

Xu, X., C. Lithgow-Bertelloni, and C. P. Conrad (2006), Global reconstructions of Cenozoic seafloor ages: Implications for bathymetry and sea level, *Earth and Planetary Science Letters*, *243*(3), 552–564.

Zahnle, K., N. Arndt, C. Cockell, A. Halliday, E. Nisbet, F. Selsis, and N. H. Sleep (2007), Emergence of a habitable planet, *Space Science Reviews*, *129*(1-3), 35–78.

# Chapter 3

# M3LT: A new model to explore the dynamics of Melt in the Mantle beneath Mid-ocean ridges

## 3.1 Abstract

Mid-ocean ridges run for more than 60,000 km of the ocean floor and are a prominent feature of plate tectonics. Regions of partially molten mantle at least 50 km wide have been inferred in the mantle beneath specific ridge systems (e.g. *Forsyth et al.* (1998a,b); *Key et al.* (2013)) and yet these melts erupt in a narrow neo-volcanic region of a few kilometers across to form the oceanic crust (*Macdonald*, 1982; *Carbotte et al.*, 2016). Debate around how the system focuses melt has evolved over the years as new observations and improved modeling shed light on some aspects of the problem. Here we introduce and describe new two-dimensional, two-phase numerical models beneath mid-oceanic ridges, Melt in the Mantle beneath Mid-ocean Ridges (M3LT). M3LT is built using TerraFERMA, the Transparent Finite Element Rapid Model Assembler (*Wilson et al.*, 2017), an open source software framework for coupled multi-physics problems. Our mid-ocean ridge models incorporate realistic viscosities and thermal feedbacks. This paper provides technical details on the formulation, setup and numerical implementations of these models and releases working TerraFERMA input files for reproducible computations. We use these models to review and illustrate the various mechanisms that are responsible for melt focusing.

## 3.2 Introduction

Magmatism at mid-ocean ridges accounts for about 90% of global volcanism. The upwelling of mantle due to the separation of oceanic plates causes decompression melting. The generation and transportation of partially molten mantle beneath the ridge axis are complicated and obscured since the rocks are inaccessible. Regional seismic and magnetotelluric surveys have imaged a wide partially molten region beneath specific mid-ocean ridges (*Forsyth et al.*, 1998a,b; *Key et al.*, 2013) and yet the oceanic crust is only formed within a few kilometers of the ridge axis (*Macdonald*, 1982). To complement the geophysical observations, theoretical models are needed to help better understand the physics governing these systems (e.g *Spiegelman and McKenzie* (1987); *Katz* (2010)).

The theoretical framework for two-phase flow applied to mantle material was developed independently by several workers (*McKenzie*, 1984; *Fowler*, 1985; *Scott and Stevenson*, 1986). The governing equations are highly coupled and to begin to understand the underlying physics requires simple analytical solutions (e.g *Spiegelman and McKenzie* (1987); *Phipps-Morgan* (1987); *Spiegelman* (1993a,b)). While the fundamental equations have remained largely unchanged, the constitutive relations for rheology, permeability and interphase exchanges often vary from one model to the next. For example, a novel framework for reactive, disequilibrium, multi-component melting has been employed to parameterize melting (*Keller and Katz*, 2016; *Keller et al.*, 2017).

One of the two goals of this chapter is to ensure the reproducibility of our results by being transparent about the model choices made. Here, I present a new two-dimensional, open-source model for exploring the dynamics of Melt in the Mantle beneath the Mid-ocean ridge system (M3LT). M3LT is built using TerraFERMA, the Transparent Finite Element Rapid Model Assembler (TF) (*Wilson et al.*, 2017). Since two-phase models are complex, I dedicate this chapter to describing the model set up, especially the constitutive, boundary conditions and numerical methods in detail. As with any complex model, it is difficult to describe every single detail such that the models can be reproduced exactly. Therefore, the codes, in the form of TerraFERMA mark up language files (.tfml), are openly

available so that the reader can reproduce exactly what was done.

The model presented here is one-way coupled and is the first of a suite of planned models. M3LT solves solid Stokes flow for dynamic pressure, solid velocity and temperature and then proceeds to solve the two-phase flow equations. This is a natural first step to understand the dynamics of the two-phase equations applied to mid-ocean ridges. Doing so also saves computational time as a solid Stokes flow solve at every time step is avoided.

The second goal of this chapter is to understand melt focusing mechanisms beneath mid oceanic ridges. Focusing mechanisms are needed if melt is generated in a wide region, as is observed geophysically (*Bown and White*, 1994; *Forsyth et al.*, 1998a,b; *Key et al.*, 2013). Various focusing mechanisms have been proposed: 1) dynamic pressure, due to incompressible shear, pulls in melt from around the ridge axis (*Spiegelman and McKenzie*, 1987; *Phipps-Morgan*, 1987), 2) anisotropic permeability where cracks allow melt to permeate through in specific direction (*Phipps-Morgan*, 1987), 3) shear driven melt bands from localization instability (*Holtzman et al.*, 2003a,b; *Kohlstedt and Holtzman*, 2009), 4) decompaction layer or thermal boundary layer (*Sparks and Parmentier*, 1991; *Spiegelman*, 1993c; *Hebert and Montési*, 2010; *Keller et al.*, 2017), 5) reactive infiltration instability where melt forms channels that coalesce into bigger ones (*Aharonov et al.*, 1995; *Spiegelman et al.*, 2001) and 6) recently observed melting rate pressure mechanism (*Turner et al.*, 2017) that we also observe.

In this chapter, I describe an example model with half spreading rate, $U_0 =$ 4 cm/yr, generates $\sim$6 km of oceanic crust, which is within the range of observed oceanic crustal thickness. The example model successfully delivers this melt to the ridge axis through three distinct melt focusing mechanisms, namely ridge suction, decompaction layers and the melting rate pressure mechanism, which we describe in detail.

First, I will describe the set of governing equations for this problem along with the required constitutive relations. Next, I will describe how we set up and solve these equations numerically with M3LT. Lastly, I present results from an example model.

## 3.3 Model formulation

The governing equations for the flow of a low viscosity fluid in a viscously deformable, permeable matrix were derived by various workers (*McKenzie*, 1984; *Scott and Stevenson*, 1984, 1986; *Fowler*, 1985), which have since been extended to include features such as surface tension (*Bercovici et al.*, 2001a,b; *Ricard et al.*, 2001; *Bercovici and Ricard*, 2003) or more complex visco-plastic rheologies (*Keller et al.*, 2013). Nevertheless, at their basic level, all of these formulations are macroscopic descriptions based on volume averaging of two interpenetrating viscous fluids. Under specific assumptions, these formulations all reduce to the same underlying set of partial differential equations (see *Simpson et al.* (2010a,b) for a detailed comparison of the different derivations). A review of the derivation of these two-phase equations with an emphasis on the energy equations is provided by *Rudge et al.* (2010).

Statements of mass conservation for the fluid and solid phases respectively are given by

$$\frac{\partial}{\partial t}(\rho_f \phi) + \nabla \cdot \rho_f \phi \mathbf{v_f} = \Gamma \tag{3.1}$$

$$\frac{\partial}{\partial t}(\rho_s (1-\phi)) + \nabla \cdot \rho_s (1-\phi) \mathbf{v_s} = -\Gamma \tag{3.2}$$

where $\rho_f$ and $\rho_s$ are the fluid and solid matrix densities, $\phi$ is the volume fraction of melt (porosity), $\mathbf{v_f}$ and $\mathbf{v_s}$ are the fluid and solid matrix velocities and $\Gamma$ is the melt production rate. $\Gamma > 0$ represents melting while the $\Gamma < 0$ represents freezing.

The total conservation of momentum for compactible two-phase Stokes flow is given by

$$\nabla \cdot (2\eta \dot{\epsilon}_d + \zeta \nabla \cdot \mathbf{v_s} \mathbf{I}) - \nabla P + \bar{\rho} \mathbf{g} = 0 \tag{3.3}$$

where $\eta$ is the shear viscosity, $\dot{\epsilon}_d$ is the deviatoric strain rate, $\zeta$ is the bulk viscosity, $P$ is the total fluid pressure, $\bar{\rho} = \phi \rho_f + (1-\phi)\rho_s$ is the phase averaged density and $\mathbf{g}$ is the gravitational acceleration. The deviatoric strain rate tensor is defined as:

$$\dot{\epsilon}_d = \frac{1}{2}(\nabla \mathbf{v_s} + \nabla \mathbf{v_s^T}) - \frac{1}{3} \nabla \cdot \mathbf{v_s} \mathbf{I} \tag{3.4}$$

Conservation of momentum for the mean fluid flux in the pores is governed by Darcy's law:

$$\phi(\mathbf{v_f} - \mathbf{v_s}) = -\frac{K}{\mu}(\nabla P - \rho_f \mathbf{g}) \tag{3.5}$$

where $K$ is the permeability and $\mu$ is the fluid viscosity. This formulation neglects surface tension and assumes that the fluid is much less viscous than the solid mantle matrix. All the variables are given in Table 1.

Assuming no heat sources due to radioactivity or viscous dissipation, the energy equation (*Rudge et al.*, 2010) is given by:

$$\rho_f c_p^f \phi \frac{D_f T}{Dt} + \rho_s c_p^s (1-\phi)\frac{D_s T}{Dt} - \phi \alpha_f T \frac{D_f P}{Dt} - (1-\phi)\alpha_s T \frac{D_s P}{Dt} + T\Delta S \Gamma - \nabla \cdot k \nabla T = 0 \tag{3.6}$$

where $c_p^f$ and $c_p^s$ are the heat capacities of fluid and solid matrix, $T$ is the temperature, which is assumed to be in thermal equilibrium between melt and solid mantle, $\alpha_s$ and $\alpha_f$ are the solid and fluid thermal expansion coefficient, $P$ is the thermodynamic pressure, $\Delta S = s_f - s_s$ is the change in entropy on melting and $k$ is the thermal conductivity. $\frac{D_f}{Dt}$ and $\frac{D_s}{Dt}$ are the fluid and solid material derivatives:

$$\frac{D_f}{Dt} = \frac{\partial}{\partial t} + \mathbf{v_f} \cdot \nabla \tag{3.7}$$

$$\frac{D_s}{Dt} = \frac{\partial}{\partial t} + \mathbf{v_s} \cdot \nabla \tag{3.8}$$

Total fluid pressure, $P$, can be decomposed into compaction pressure, $\mathcal{P}$, dynamic pressure, $p^*$, and lithostatic pressure, $P_L$:

$$P = \mathcal{P} + p^* + P_L \tag{3.9}$$

Compaction pressure, $\mathcal{P}$, is defined by the compaction and decompaction of the solid matrix scaled by the bulk viscosity.

$$\mathcal{P} = \zeta \nabla \cdot \mathbf{v_s} \tag{3.10}$$

$p^*$ is the dynamic pressure due to incompressible solid shear and $P_L$ is defined as:

$$P_L(z) = \rho_s g z \tag{3.11}$$

**Table 3.1**: Symbols and their definition in the equations

| Symbol | Definition |
|---|---|
| $\mathbf{v}$ | Velocity |
| $U$ | Half spreading rate |
| $T$ | Temperature |
| $p^*$ | Dynamic pressure |
| $\mathcal{P}$ | Compaction pressure |
| $\phi$ | Porosity |
| $t$ | Time |
| $\cdot_s$ | subscript denoting solid |
| $\cdot_f$ | subscript denoting fluid |
| $\rho$ | Density |
| $\Delta\rho$ | Difference in density between fluid and solid ($\rho_s - \rho_f$) |
| $\Gamma$ | Melting rate |
| $\eta$ | Solid shear viscosity |
| $\dot{\epsilon}_d$ | Deviatoric stain rate |
| $\zeta$ | Bulk viscosity |
| $\mathbf{I}$ | Identity matrix |
| $\mathbf{g}$ | Gravitational acceleration |
| $K$ | Permeability |
| $\mu$ | Melt viscosity |
| $c_p$ | Heat capacity at constant pressure |
| $\alpha$ | Thermal expansion coefficient |
| $P$ | Thermodynamic pressure |
| $\Delta S$ | Change in Entropy |
| $k$ | Thermal conductivity |
| $\kappa$ | Thermal diffusivity |

Rearranging and making appropriate substitutions, the following set of governing equations is obtained:

$$\nabla \cdot 2\eta\dot{\epsilon}_d - \nabla p^* + \Delta\rho\phi\mathbf{g} = 0 \tag{3.12}$$

where $\Delta\rho = \rho_s - \rho_f$.

$$\frac{\mathcal{P}}{\zeta} = \nabla \cdot \mathbf{v_s} \tag{3.13}$$

$$\frac{D_s\phi}{Dt} + (1-\phi)\frac{\mathcal{P}}{\zeta} = -\frac{\Gamma}{\rho_s} \tag{3.14}$$

$$\frac{\mathcal{P}}{\zeta} - \nabla \cdot \frac{K}{\mu}(\nabla\mathcal{P} + \nabla p^* + \Delta\rho\mathbf{g}) = \frac{\Delta\rho}{\rho_f\rho_s}\Gamma \tag{3.15}$$

$$\rho_f c_p^f \phi\frac{D_f T}{Dt} + \rho_s c_p^s(1-\phi)\frac{D_s T}{Dt} - \phi\alpha_f T\frac{D_f P}{Dt} - (1-\phi)\alpha_s T\frac{D_s P}{Dt} + T\Delta S\Gamma - \nabla\cdot k\nabla T = 0 \tag{3.16}$$

This set of governing equations describe percolative fluid flow through a viscously deforming and compactible mantle matrix. The equations include mass transfer and energy conservation but are not closed until the functional forms for $\eta$, $\zeta$, $K$ and $\Gamma$ are given.

The fluid and solid densities are held constant in our models, i.e $\rho_f = 2800$ kg/m$^3$ and $\rho_s = 3300$ kg/m$^3$. To understand the first order effects, we make the assumption that the changes in densities are small compared with the densities themselves. In reality, basaltic melt extraction leaves behind a depleted residue and reduces the density by decreasing the Fe/Mg ratio and the proportion of garnet (e.g. *Sotin and Parmentier* (1989)). This change in density can impact the details of melting and melt flow (*Jha et al.*, 1994).

### 3.3.1 Constitutive relations

To close the set of governing equations, constitutive relations are required to describe the solid rheology, permeability and, in particular, melting rate, $\Gamma$.

#### Rheology

Shear viscosity can vary with temperature, pressure, strain-rate/stress, presence of melt and volatiles and grain size (*Hirth and Kohlstedt*, 2003). We

assume that the solid rheology is described by a mixture of diffusion creep, dislocation creep and a small plasticity term. In detail, we use temperature dependent diffusion creep:

$$\eta_{diff} = A_{diff} e^{[-E_{diff}/(RT)]} \tag{3.17}$$

where $A_{diff}$ and $E_{diff}$ are the constant and activation energy for diffusion creep respectively, and $R$ is the universal gas constant. We also use temperature and strain rate dependent dislocation creep (*Karato and Wu*, 1993; *Hirth and Kohlstedt*, 2003):

$$\eta_{disl} = A_{disl} e^{[-E_{disl}/(RT)]} \dot{\epsilon}_{II}^{1-\frac{1}{n_{disl}}} \tag{3.18}$$

where $A_{disl}$ and $E_{disl}$ are the constant and activation energy for dislocation creep respectively, $\dot{\epsilon}_{II}$ is the second invariant of strain rate and $n_{disl} = 3.5$ is the exponent of stress. The values for parameters used are given in Table 3.2.

The Arrhenius relationship describing the temperature dependence of shear viscosity in both creep laws leads to very strong material when the temperatures are low. This can create unrealistic stresses when modeling geologic material with high strain rate (i.e flow near a ridge), and therefore needs to be bounded. We use a weakening mechanism that is an approximation to Drucker-Prager viscoplasticity, which is a lithostatic pressure dependent rheological model for plastic yielding (depth-dependent von Mises (*Spiegelman et al.*, 2016))

$$\eta_{plast} = \frac{Y}{2\dot{\epsilon}_{II}} \tag{3.19}$$

where

$$Y = C\cos\varphi + P_L \sin\varphi = A + BP_L \tag{3.20}$$

C is the constant of cohesion independent of pressure ($10^8$ Pa), $\varphi$ is the friction angle ($0 - 30°$), $A = 5 \times 10^7$ Pa, $B = 0.5$ and $P_{lith} = \rho_s g z$. Full Drucker-Prager plasticity replaces $P_{lith}$ with the dynamic pressure, $p^*$, however, *Spiegelman et al.* (2016) shows that this formulation can be ill-posed.

To prevent the solid matrix from becoming too strong, we impose a maximum viscosity, $\eta_{max}$. We use a smooth inverse combination of the various deformation mechanisms, which produces an effective viscosity that favors the weakest

mechanism (*Spiegelman et al.*, 2016; *Tosi et al.*, 2015):

$$\frac{1}{\eta} = \frac{1}{\eta_{diff}(T)} + \frac{1}{\eta_{disl}(T, \dot{\epsilon}_{II})} + \frac{1}{\eta_{max}} + \frac{2\dot{\epsilon}_{II}}{Y} \tag{3.21}$$

In this formulation, we have not included a melt weakening shear viscosity (e.g *Cooper and Kohlstedt* (1984); *Kohlstedt et al.* (2000); *Mei et al.* (2002)) that has been used in other models (e.g. *Katz et al.* (2006); *Keller et al.* (2013)). For the generally small porosities generated in these models, this effect is negligible but could become important in fully coupled models in regions of local melt-pooling. Given the flexibility of TerraFERMA based models, however, it would not be difficult to add this effect and compare solutions.

For bulk viscosity, $\zeta$, we use

$$\zeta = \frac{\eta}{\phi} \tag{3.22}$$

This inverse dependence on porosity for $\zeta$ was previously suggested (e.g *Scott and Stevenson* (1984); *Schmeling et al.* (2000)). Using homogenization theory, *Simpson et al.* (2010a,b) have shown that this functional relationship, and the full McKenzie equations for momentum conservation, are consistent with upscaling the deformation of two interpenetrating viscous stokes fluids with very different viscosities.

**Permeability**

The permeability of upper mantle materials (olivine, lherzolites, harzburgites) are constrained experimentally (*Zhu et al.*, 1995; *Wark and Watson*, 1998) and are well approximated by a simple power law similar to the Blake-Kozeny-Carman equation (*Dullien*, 2012):

$$K = \frac{a^2\phi^n}{b} = K_0\phi^n \tag{3.23}$$

where $a$ is the pore or channel spacing, $b$ is a dimensionless coefficient and $n$ is the exponent dependence on porosity.

The expected scaling for the porosity exponent in the small tube limit (simulating melt along a grain boundary edge) is $n = 2$, whereas experimentally,

more complicated geometries suggest $n = 3$, at least for porosities $> 2\%$ (*Zhu et al.*, 1995; *Miller et al.*, 2014, 2016). This is dependent on small scale grain geometry. *Wark and Watson* (1998) have done experiments using water in calcite and quartz and they show that "even for texturally equilibrated rocks, the permeable network deviates from the ideal case of self-similarity at all porosities" (*Faul*, 2001). We use $n = 3$ with background permeability, $K_0 = 4 \times 10^{-9}$ m$^2$, in our models. We do not consider anisotropic permeability (*Phipps-Morgan*, 1987).

**Melting/Freezing relations**

All the parameterization for melting and freezing we discuss here are for closed systems in terms of mass transport but allows heat transport. We describe the total melting rate, $\Gamma$:

$$\Gamma = \Gamma_s + \Gamma_f \tag{3.24}$$

where $\Gamma_s$ is the melting rate and $\Gamma_f$ is the freezing rate. Given a closed system pseudo phase diagram $f_s(T, P)$ and for $T > T_{solidus}$ (peridotite solidus *Hirschmann* (2000)), we define the melting rate of solid, $\Gamma_s$, as:

$$\Gamma_s = \rho_s(1-\phi)\frac{D_s f_s}{Dt} = \rho_s(1-\phi)\left[\frac{\partial f_s}{\partial T}\frac{D_s T}{Dt} + \frac{\partial f_s}{\partial P}\frac{D_s P}{Dt}\right] \tag{3.25}$$

where $f_s$ is the volume fraction of melt predicted in a closed system (batch melting) as a function of pressure and temperature.

We use a power law parameterization of the peridotite phase diagram, where $f_s$, for equilibrium batch melting before the exhaustion of clinopyroxenes (*Katz et al.*, 2003), is:

$$f_s(T') = [T'(T, P)]^{\beta} \tag{3.26}$$

$\beta = 1.5$ is the power law exponent and $T'(T, P)$ is the rescaled temperature:

$$T'(T, P) = \frac{T - T_{solidus}(P)}{T^{lherz}_{solidus}(P) - T_{solidus}(P)} \tag{3.27}$$

where $T_{solidus}(P)$ is the peridotite solidus temperature, $T^{lherz}_{solidus}(P)$ is the lherzolite solidus temperature (*Katz et al.*, 2003). We use the solidi adopted by *Hirschmann* (2000) based on a number of experimental constraints for natural peridotites (e.g.

*McKenzie and Bickle* (1988); *Hirose and Kushiro* (1993); *Herzberg et al.* (2000)). This formulation of the phase diagram implicitly assumes a constant bulk composition for a lherzolite but tracks clinopyroxene depletion.

For freezing rate, $\Gamma_f$, we use a reactive formulation that is dependent on the temperature difference below the solidus:

$$\Gamma_f = \rho_f \phi R[T - T_{solidus}(P) - |T - T_{solidus}(P)|] \tag{3.28}$$

where R is the freezing rate constant. Freezing rate, $\Gamma_f$, depends on density of the melt, porosity and $T - T_{solidus}(P)$. The dependence on porosity ensures that there will be freezing only when melt is present.

To determine clinopyroxene exhaustion, we follow *Spiegelman* (1996) to determine the concentration of a completely compatible trace element (i.e bulk partition coefficient $D \to \infty$) and relate that to the local degree of depletion a piece of solid has undergone. This formulation can be extended to trace elements in equilibrium. For trace elements, the solid concentration, $c^s$, is related to fluid concentration, $c^f$, by the bulk partition coefficient, $D$:

$$c^s = Dc^f \tag{3.29}$$

For disequilibrium transport characterized by the solid velocity, we conserve melt and solid compositions following *Spiegelman* (1996). Conservation of mass of a trace element undergoing fractional melting in the solid can be written as:

$$\frac{\partial U^s}{\partial t} + \mathbf{v_s} \cdot \nabla U^s = \left(1 - \frac{1}{D}\right) \frac{\Gamma}{\rho_s(1-\phi)} \tag{3.30}$$

where $U^s = \ln(c^s/c_0^s)$ is the ratio of concentration and $c_0^s$ is the reference solid concentration. For a completely compatible element (i.e $D \to \infty$) that partitions completely into solid residue, $U^s$ will increase with increasing melting:

$$\frac{\partial U^s}{\partial t} + \mathbf{v_s} \cdot \nabla U^s = \frac{\Gamma}{\rho_s(1-\phi)} \tag{3.31}$$

The local degree of depletion, $F_d$, for the solid is (*Spiegelman*, 1996):

$$F_d = 1 - \frac{c_0^s}{c^s} = 1 - e^{-U_s} \tag{3.32}$$

A mantle peridotite is made up of mostly olivine, along with orthopyroxene and clinopyroxenes (and/or garnet). Clinopyroxene, being the most enriched in incompatible elements, is likely the first of the three minerals to be depleted. Clinopyroxene primarily controls melt production in the spinel peridotite field for which estimates of modal clinopyroxene have a wide range, i.e. $\sim 15 - 40\%$ from experiments on anhydrous peridotites (*Longhi*, 2002; *Katz et al.*, 2003). In our models, melting is terminated when $F_d = 0.2$, approximating a lherzolite with 20% modal clinopyroxenes, which is high but observed (*McDonough and Rudnick*, 1998).

### 3.3.2 Non-dimensionalization

To reduce the number of adjustable parameters and provide numerical stability, we solve dimensionless versions of the governing equations. Here we scale the critical variables as:

$$\phi = \phi_0 \phi' \quad \mathbf{x} = h\mathbf{x}' \quad (\mathbf{v_s}, \mathbf{v_f}) = w_0(\mathbf{v'_s}, \mathbf{v'_f}) \tag{3.33}$$

$$(\mathcal{P}, p^*) = \Delta\rho g h(\mathcal{P}, p^*)' \quad T = T_1 T' \quad t = \frac{h}{w_0} t' \tag{3.34}$$

$$\eta = \eta_0 \eta' \quad \zeta = \frac{\eta_0}{\phi_0}\zeta' \qquad K = K_0 \phi_0^n K' \tag{3.35}$$

$$\Gamma = \frac{\rho_s \phi_0 w_0}{h}\Gamma' \quad \phi_0 w_0 = \frac{K_0 \phi_0^n \Delta\rho g}{\mu} \tag{3.36}$$

where dimensionless variables are denoted by primes. $t$ is scaled by the time taken for fluid melt traveling at velocity, $w_0$, to cross the domain depth, $h$. $\Gamma$ is scaled to have units of density per unit time (*Spiegelman*, 1996). Melt flux, $\phi_0 w_0$, is defined as the natural percolative melt flux from the Darcy equation (Equation 3.15).

To provide a reasonable estimate for the reference porosity, $\phi_0$, and reference melt velocity, $w_0$, we use the results for the porosity structure of a 1-D steady state upwelling melting column (e.g. *Ribe* (1987); *Spiegelman and Elliott* (1993)). In the 1-D melting column, if all the melting is due to adiabatic decompression, then the melting rate is proportional to mantle upwelling rate such that $\Gamma = \rho_s W_0 \frac{dF_0}{dz}$, where $\frac{dF_0}{dz}$ is the imposed change in the degree of melting with height in the melting region and $W_0$ is the upwelling rate. Conservation of mass in a steady state 1-D upwelling

column implies that the melt flux at any point in the column must balance total melt production up to that point. Thus, if we use the porosity at the top of the column, where $F_0 = F_{max}$, as our reference porosity, and approximate upwelling rate, $W_0$, with half spreading rate, $U_0$, it follows that $\rho_f \phi_0 w_0 = \rho_s U_0 F_{max}$. Now we have two equations for melt flux $\phi_0 w_0$ and can solve for both $\phi_0$ and $w_0$ given the rest of the parameters.

From the $\Gamma$ scaling and equation 3.28 for freezing rate, the freezing rate constant, $R$, has to be proportional to $\frac{\phi_0 w_0}{h}$ and has units of $s^{-1}$. Using the one dimensional melting column approximation, the freezing rate constant, $R$, should then scale linearly with half spreading rate, $U_0$.

Substituting these definitions and dropping primes, the dimensionless equations can be written:

$$\left(\frac{\delta_0}{h}\right)^2 \nabla \cdot 2\eta \dot{\epsilon}_d - \nabla p^* + \phi_0 \phi \hat{\mathbf{k}} = 0 \tag{3.37}$$

$$\nabla \cdot \mathbf{v_s} = \phi_0 \left(\frac{h}{\delta_0}\right)^2 \frac{\mathcal{P}}{\zeta} \tag{3.38}$$

$$\frac{\partial \phi}{\partial t} + \mathbf{v_s} \cdot \nabla \phi + (1 - \phi_0 \phi) \left(\frac{h}{\delta_0}\right)^2 \frac{\mathcal{P}}{\zeta} = -\Gamma \tag{3.39}$$

$$\left(\frac{h}{\delta_0}\right)^2 \frac{\mathcal{P}}{\zeta} - \nabla \cdot \frac{K}{\mu}[\nabla(\mathcal{P} + p^*) + \hat{\mathbf{k}}] = \frac{\Delta \rho}{\rho_f \rho_s} \Gamma \tag{3.40}$$

$$\begin{aligned} \left(\frac{\rho_f}{\rho_s}\phi_0 \phi + (1 - \phi_0 \phi)\right) \frac{\partial T}{\partial t} + \frac{\rho_f}{\rho_s}\phi_0 \phi \mathbf{v_f} \cdot \nabla T + (1 - \phi_0 \phi)\mathbf{v_s} \cdot \nabla T - \\ (1 - \phi_0 \phi)\frac{\alpha_s g h}{c_p} T \mathbf{v_s} \cdot \hat{\mathbf{k}} + \phi_0 \frac{L_0}{c_p T_1} L\Gamma - \frac{1}{Pe} \nabla^2 T = 0 \end{aligned} \tag{3.41}$$

where $\hat{\mathbf{k}}$ is the vertical unit vector. $\delta_0$ is the compaction length scale (*McKenzie*, 1984):

$$\delta_0^2 = \frac{K_0 \phi_0^n \zeta_0}{\mu} = \frac{K_0 \phi_0^n}{\mu} \left(\frac{\eta_0}{\phi_0}\right) \tag{3.42}$$

$\delta_0$ can be interpreted as the length scale over which variations in the melt flux generate excess pressure through volumetric viscous strain. $Pe$ is the Peclet number:

$$Pe = \frac{w_0 h}{\kappa} \tag{3.43}$$

The Peclet number is a measure of advective heat transport versus diffusive heat transport and $\kappa$ is the thermal diffusivity such that $\kappa = \frac{k}{\rho_s c_p}$. In the energy equation, we have assumed that thermodynamic pressure is basically lithostatic and that the adiabatic term from the fluid phase is negligible. From here on, equations will be in non-dimensional form unless indicated otherwise.

### 3.3.3 One way coupling in the small porosity limit

In the limit of small porosity, the terms in the Equations 4.6-4.10 that are scaled by $\phi_0$ are dropped. This decouples the two momentum and continuity equations such that the solid flow no longer depends on the fluid flow. On the other hand, the fluid flow still depends on the solid velocity and dynamic pressure.

#### Solid Stokes system

Using the small porosity approximation, equations 4.6, 4.7 and 4.10 become

$$\frac{\delta_0^2}{h^2}\nabla \cdot 2\eta\dot{\epsilon}_d - \nabla p^* = 0 \tag{3.44}$$

$$\nabla \cdot \mathbf{v_s} = 0 \tag{3.45}$$

$$\mathbf{v_s} \cdot \nabla T - \frac{\alpha_s g h}{c_p} T \mathbf{v_s} \cdot \hat{\mathbf{k}} + \phi_0 \frac{L_0}{c_p T_1} L\Gamma - \frac{1}{Pe}\nabla^2 T = 0 \tag{3.46}$$

respectively in the solid system. This is the solid phase Stokes problem, except that it allows for temperature variations due to melting and latent heat. The melting term is kept in the energy equation since $\Gamma$ is of order $F_{max}/\phi_0$ in this scaling so the term is of order $F_{max}$ not $\phi_0$. We have assumed that temperature does not vary with time. We solve for solid velocity, $\mathbf{v_s}$, dynamic pressure, $p^*$, and temperature, $T$, in the solid system.

#### Fluid system

Similarly for the fluid system, Equations 4.8-4.10 become

$$\frac{\partial \phi}{\partial t} + \mathbf{v_s} \cdot \nabla \phi + \frac{h^2}{\delta_0^2}\frac{\mathcal{P}}{\zeta} = -\Gamma \tag{3.47}$$

$$\frac{h^2}{\delta_0^2}\frac{\mathcal{P}}{\zeta} - \nabla \cdot \frac{K}{\mu}[\nabla(\mathcal{P} + p^*) + \hat{\mathbf{k}}] = \frac{\Delta\rho}{\rho_f \rho_s}\Gamma \tag{3.48}$$

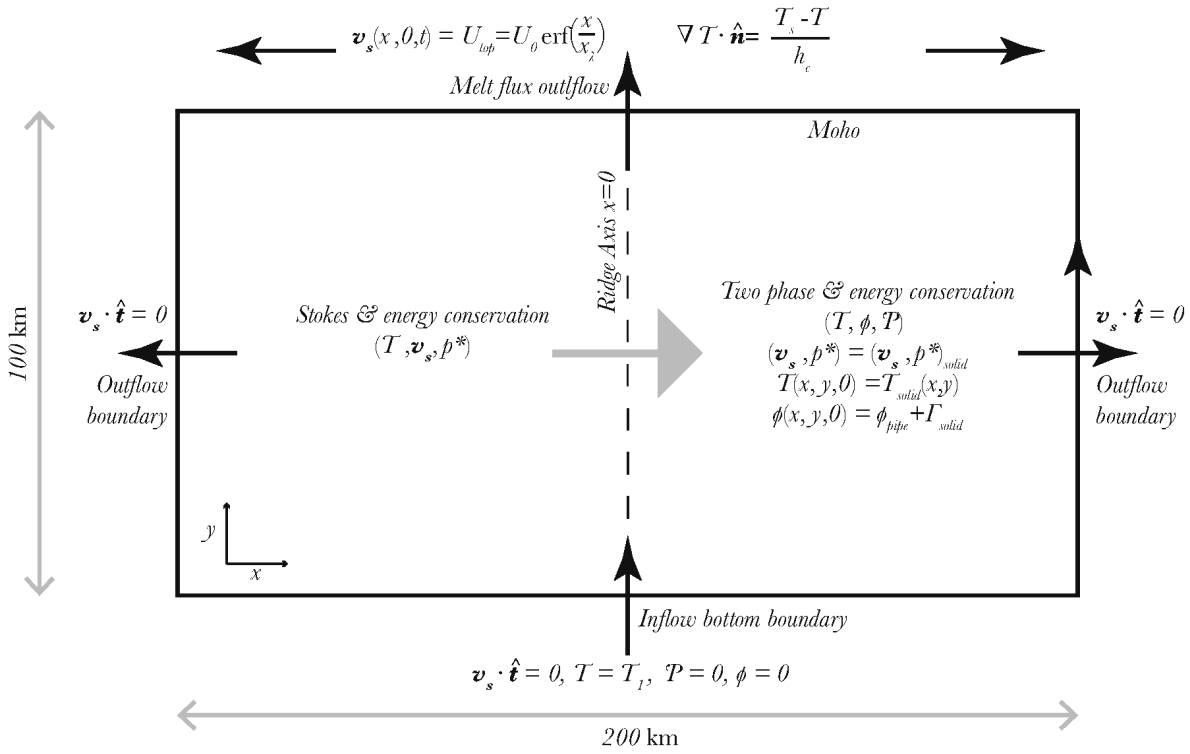


**Figure 3.1**: Schematic of 2D model diagram with initial and boundary conditions.

$$\begin{aligned}(\frac{\rho_f}{\rho_s}\phi_0\phi + (1-\phi_0\phi))\frac{\partial T}{\partial t} + \frac{\rho_f}{\rho_s}\phi_0\phi\mathbf{v_f}\cdot\nabla T + (1-\phi_0\phi)\mathbf{v_s}\cdot\nabla T \\ -\frac{\alpha_s g h}{c_p}T\mathbf{v_s}\cdot\hat{\mathbf{k}} + \phi_0\frac{L_0}{c_p T_1}L\Gamma - \frac{1}{Pe}\nabla^2 T = 0\end{aligned} \tag{3.49}$$

For the fluid system, we have kept the thermal evolution and advection terms in the energy equation even with the small porosity limit to understand heat transport and production via melting processes. We solve for porosity, $\phi$, compaction pressure, $\mathcal{P}$, and temperature, $T$, in the fluid system.

## 3.4 Numerical implementations

A schematic of our model set up with initial and boundary conditions is shown in Figure 3.1. Our domain is rectangular with a width of 200 km and a depth of 100 km. The ridge axis is at the center. Since the governing equations really only describe flow in a permeable, viscously deformable media, we restrict the top of the domain to be the Moho.

### 3.4.1 Boundary conditions

Our model assumes that mantle upwelling beneath mid-ocean ridges is passively driven by plate motion. This is enforced by a Dirichlet boundary condition on solid velocity along the top boundary such that:

$$U_{top} = U_0 \text{erf}\left(\frac{x}{x_\lambda}\right) \tag{3.50}$$

where $x$ is the distance from the ridge axis and $x_\lambda = 0.01$ (1 km) is the width of the smoothed step function, which is chosen to represent roughly the width of the neo-volcanic zone at the ridge axis. Solid flow tangent to the sides and bottom boundaries is not allowed (i.e $\mathbf{v_s} \cdot \hat{\mathbf{t}} = 0$, where $\hat{\mathbf{t}}$ is the unit vector tangent to the boundary). The top boundary allows melt to outflow but prevents any outflow of the solid mantle (i.e the upper boundary condition for the solid velocity is $\mathbf{v_s} \cdot \hat{\mathbf{n}} = 0$, where $\hat{\mathbf{n}}$ is the unit vector normal to the boundary).

One of the critical problems in all ridge models is maintaining a weak corner at the ridge axis such that melt can escape to form the oceanic crust. This can be highly problematic if one starts from a cold thermal boundary layer near the Moho. Since the top of the domain is the Moho, the upper thermal boundary condition should not be sea-floor temperature but an approximation to Moho temperature, which can change depending on advection of heat by solid and melt. Here we use a Robin condition:

$$\nabla T(x) \cdot \hat{\mathbf{n}} = \frac{T_s - T(x)}{h_c} \tag{3.51}$$

where we assume a linear relationship between ocean surface temperature, $T_s$, and temperature at the Moho over $h_c$, the crustal thickness. Given $T_s = 0°\text{C}$ and $h_c = 7$ km, the system can solve for $T$ at the top boundary. Using crustal thickness, $h_c = 7$ km, will lead to an inconsistency if the crust is not 7 km thick (particularly at slow spreading) but this is necessary to keep the ridge axis sufficiently weak along with the plasticity discussed in Section 3.3.1.

For our system of governing equations, another boundary condition is required. Since there is only solid inflow at the bottom boundary, it is consistent to enforce that the compaction pressure is zero on the boundary, since solid flow is incompressible outside of the melting regime (i.e. $\nabla \cdot \mathbf{v_s} = 0$ implying $\mathcal{P} = 0$).

### 3.4.2 Initial conditions

Initial conditions are only necessary for temperature and porosity in the fluid system equations. The initial condition for temperature, $T$, is the temperature solution from the solid system:

$$T(x, y, 0) = T_{solid}(x, y) \tag{3.52}$$

The initial condition for porosity consists of two parts:

$$\phi(x, y, 0) = \Phi(\Gamma_{solid}(x, y)) + \phi_{pipe} \tag{3.53}$$

$\Phi(\Gamma_{solid}(x, y))$ is the porosity approximated from the melting rate in the solid system:

$$\Phi(\Gamma_{solid}(x, y)) = \frac{\Gamma_{solid}}{(\Gamma_{solid})_{max}} \tag{3.54}$$

To minimize transients in the model, we use an initial porosity pipe, $\phi_{pipe}$, just below the ridge axis and remove freezing for a small region at the ridge axis. Both of these features also help with maintaining a weak ridge axis to facilitate melt out of the Moho to form oceanic crust. Without the initial porosity pipe, melt will pool beneath the stronger, colder lithosphere, eventually resulting in the failure of the models. The initial porosity pipe is described by:

$$\phi_{pipe} = \phi_m e^{-\left(\frac{x}{x_{pipe}(1-m_p y)}\right)^2} \left\{ \frac{1}{2} \left[ \tanh\left( \frac{y - y_{pipe}}{y_\lambda} \right) - \tanh\left( \frac{y}{y_\lambda} \right) \right] \right\} \tag{3.55}$$

where $\phi_m = 1$ is the magnitude of scaled porosity and various other parameters, $x_{pipe}$, $m_p$, $y_{pipe}$ and $y_\lambda$, control the shape of the initial pipe.

To ensure that a melt pipe at the ridge axis is maintained as the simulation runs, we put in a small semi-circular region at the ridge axis where freezing cannot occur as follows:

$$\Gamma_{non} = \frac{1}{2} \tanh\left( \frac{\sqrt{x^2 + y^2} - x_{pipe}}{p_\lambda} \right) \tag{3.56}$$

where $p_\lambda = 0.01$. With this feature, the ridge axis is kept weak and melt flux can be maintained across the Moho at the ridge axis.

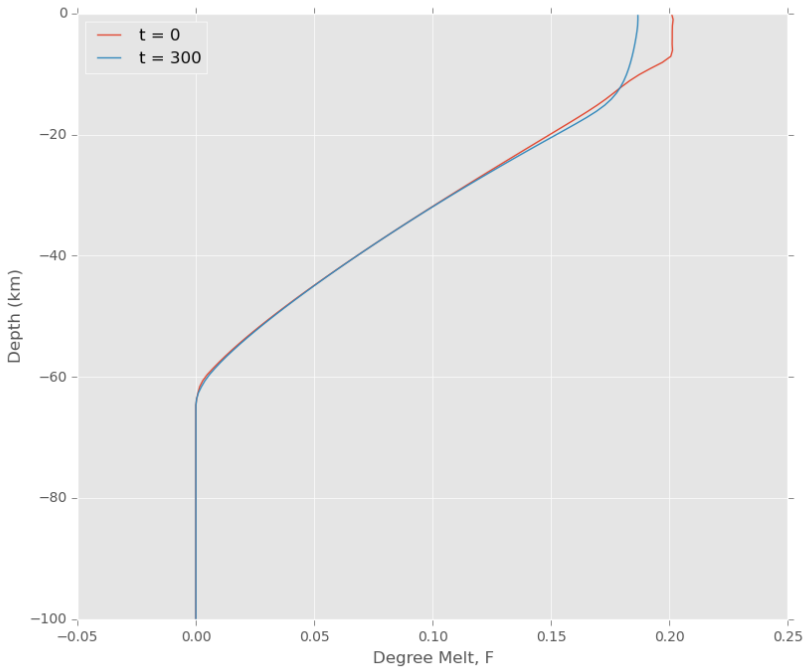


**Figure 3.2**: Depth profile of degree of depletion, $F_d$, on the ridge axis for our reference model with half spreading rate, $U_0 = 4$ cm/yr, at the beginning, $t = 0$ (red line), and at the end, $t = 300$ (blue line), of the model run. The red line shows the initial condition for degree of depletion, $F_d$, where $F_d$ is approximated by the volume fraction of melting, $f$, from the solid system. The blue line is the profile at the end of the model run, $t = 300$. The only notable change, $\sim 2\%$, of the depletion at shallow depths is due to reduced melting.

**Geochemical depletion**

For the initial condition for concentration ratio, as discussed in Section 3.3.1, we approximate the degree of depletion, $F_d$, from the volume fraction of melt, $f_s$, in the solid Stokes system (Equations 3.44-3.46). This is not only an attempt to push the model closer to the quasi steady state so as to reduce the transient/ramp up time, but also to avoid too much melting at the beginning of the simulation. The volume fraction of melt, $f_s$, is sampled on the ridge axis for the solid Stokes system, giving a one-dimensional approximation of degree of depletion. The 1-D profile of $f_s$ has a maximum, $f_{max}$, at some depths on the ridge axis. Since $f_{max}$ represents the maximum degree of melting the upwelling solid mantle would experience, anything above that depth should have at least experienced the same amount of melting. Therefore, above this depth, the degree of depletion is the maximum, $F_{max}$, and below this depth, the degree of depletion is approximated by volume fraction of melt, $F_d = f_s$. Now we have a depth profile for degree of depletion on the ridge axis, which is shown as the red line in Figure 3.2. This profile is used to calculate the initial condition for the concentration ratio (i.e Equation 3.32). In reality, the peridotite phase diagram evolves with changing pressure, temperature and chemical composition as the solid mantle melts. However, a more robust parameterization of melting is beyond the scope of this work.

### 3.4.3 Mesh

We use a triangular unstructured mesh generated by GMSH (*Geuzaine and Remacle*, 2009). Cell size is variable with ∼100 m edge lengths at the ridge axis to better resolve any sharp gradients (Figure 3.3). The mesh coarsens away from the ridge axis. The top boundary has a mesh size of at least 1 km in order to resolve the thermal boundary layer, while the bottom boundary has coarser elements, up to an edge length of ∼8 km.

### 3.4.4 Numerical method

We discretize our two systems of equations, 3.44-3.46 and 3.47-3.49, using finite elements in space and finite differences in time. In the solid system, both the

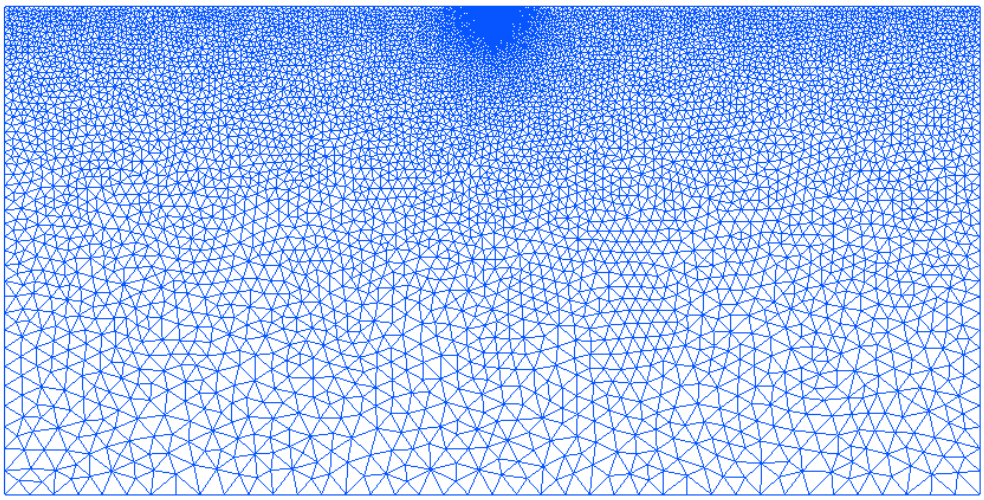

**Figure 3.3**: Mesh generated using GMSH (*Geuzaine and Remacle*, 2009).

solid velocity and temperature fields are solved as piecewise quadratic, continuous Lagrange elements (P2) for a vector and scalar respectively, while the dynamic pressure field is solved as piecewise linear, continuous Lagrange elements (P1). In the fluid phase, the porosity field is solved as piecewise quadratic, discontinuous Lagrange element (P2DG), while both the compaction pressure and temperature fields are solved as piecewise quadratic, continuous Lagrange element (P2). For a discussion on these element type choices for each field, we refer the reader to *Wilson et al.* (2017).

The models start off at non-dimensional time, $t = 0.0$, and run to a given (non-dimensional) stopping time. The run time is set by the maximum amount of time needed for a parcel of material to travel from the bottom of the domain and exit through the side boundaries or $t \sim 2h/U_0$. We use a semi-implicit Crank-Nicolson method (or trapezoidal rule) for the time integration and an adaptive time stepper based on the Courant-Friedrichs-Lewy (CFL) number for melt flux.

### Solvers

The solid system is solved twice at the start of the simulation. First, we solve an approximation of the equations to get a better initial guess for a second non-linear solve. At each iteration, $i$, the non-linear solvers (SNES, *Balay et al.*

(2017)) solve for:

$$J(\mathbf{u_i})\delta\mathbf{u_i} = -F(\mathbf{u_i}) \tag{3.57}$$

where $F$ is the weak finite element residual of the equations, $\mathbf{u_i}$ is the vector of variables, $\delta\mathbf{u_i} = \mathbf{u_{i+1}} + \mathbf{u_i}$ is the change in variables between iterations $i$ and $i+1$ and $J = F'(u')$ is the Jacobian matrix,. In the solid system, $\mathbf{u_i} = (\mathbf{v_s}, p^*, T)$:

$$J(\mathbf{u_i})\delta\mathbf{u_i} = \begin{bmatrix} K & G & 0 \\ G^T & 0 & 0 \\ B & 0 & A \end{bmatrix} \begin{bmatrix} \delta\mathbf{v_s} \\ \delta p^* \\ \delta T \end{bmatrix} = - \begin{bmatrix} F_{\mathbf{v_s}} \\ F_{p^*} \\ F_T \end{bmatrix} \tag{3.58}$$

where the upper $2 \times 2$ block is the discrete Stokes equation, $B$ contains the coupling between velocity and temperature, and $A$ is the standard advection-diffusion operator. The first approximate solver solves for the isoviscous problem such that non-dimensional shear viscosity is unity. This problem is easy to solve and gives a good estimate for the second non-linear solver with fully variable solid viscosity (i.e. Equations 3.44-3.46). The solutions for solid velocity, $\mathbf{v_s}$, and dynamic pressure, $p^*$, are used in the fluid phase and do not change with time.

The temperature solution in the solid system for our example model shows the thermal boundary layers on either side of the ridge axis (Figure 3.4). The black solid flow lines show upwelling into the domain and flow out the sides. As the top boundary (i.e the Moho) is being pulled apart, a thermal boundary layer forms away from the ridge axis creating a cooler and stronger lithosphere. Total melt production rate, $\Gamma$, as shown by the labeled white contours in Figure 3.4, is roughly triangular in shape. $\Gamma$ is highest at $\sim 1.5$ non-dimensional units beneath the ridge axis at $\sim$10-30 km depths.

Given the solid system solution, we proceed to solve the two-phase flow system (Equations 3.47-3.49). We again use two solvers at every time step. The first is a low order approximate solve for $\phi$ and $T$ to set a better initial guess for the second Newton solver which provides the actual fully converged solution (including $\mathcal{P}$) for the time step. To prevent unphysical negative porosities, we enforce a non-negative porosity requirement, $\phi \geq 0$, at every non-linear iterations using a Newton solver with bounds (SNES VI, *Balay et al.* (2017)). In the two-

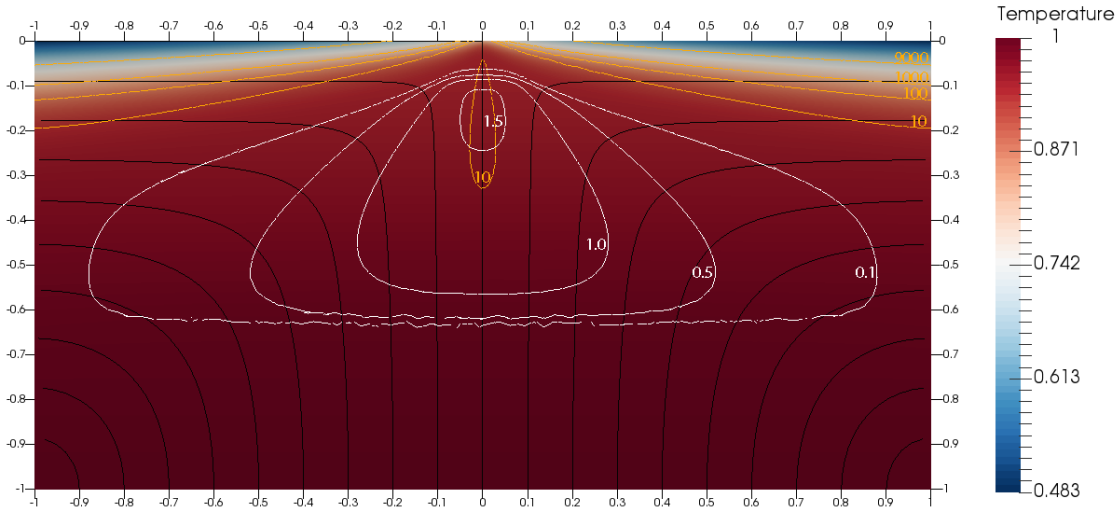


**Figure 3.4**: Non-dimensional temperature for intermediate spreading rate $U_0 = 4$ cm/yr, white contours show non-dimensional melting rate, $\Gamma$, and orange contours show shear viscosity scaled to $\eta_0 = 10^{19}$ Pa s. The domain is 200 km wide and 100 km deep. Temperature is scaled by the temperature at the base of the model, $T_1$. Solid velocity streamlines are in black.

phase system, $\mathbf{u_i} = (T, \phi, \mathcal{P})$:

$$J(\mathbf{u_i})\delta\mathbf{u_i} = \begin{bmatrix} A & B & 0 \\ C & P & Q \\ E & L & D \end{bmatrix} \begin{bmatrix} \delta T \\ \delta\phi \\ \delta\mathcal{P} \end{bmatrix} = - \begin{bmatrix} F_T \\ F_\phi \\ F_\mathcal{P} \end{bmatrix} \tag{3.59}$$

where $A$ is the advective-diffusion operator, $B$ is the porosity dependent heat advection, both $C$ and $E$ are from the temperature dependence of the shear viscosity that couples T to $\phi$ and $\mathcal{P}$, $P$ is an advection operator for porosity, $Q$ is the pressure-dependence of porosity, $D$ is the pressure operator, while $L$ is the porosity dependence of pressure.

The first initial guess solver applies the flexible generalized minimal residual method (FGMRES) to the Jacobian of the upper porosity-temperature block at each iteration. We use an additive fieldsplit preconditioner splitting porosity and temperature. The porosity block P uses a GMRES iterative method for the linear solve with an Eisentat preconditioner while temperature block A uses a Richardson iterative method with the Geometric-Algebraic MultiGrid Method (gamg) preconditioner (*Balay et al.*, 2016).

**Table 3.2**: Parameters, quantity, values and units

| Symbol | Quantity | Value | Units |
|---|---|---|---|
| $U_0$ | Half spreading rate | 4 | cm/yr |
| $h$ | Depth of domain | $10^5$ | m |
| $g$ | Gravity | 9.81 | $m/s^2$ |
| $\rho_s$ | Solid density | 3300 | $kg/m^3$ |
| $\rho_f$ | Fluid density | 2800 | $kg/m^3$ |
| $\Delta\rho$ | Density difference | $\rho_s - \rho_f$ | $kg/m^3$ |
| $A_{diff}$ | Constant for diffusion creep | $1.3204 \times 10^9$ | - |
| $E_{diff}$ | Activation energy for diffusion creep | $335 \times 10^3$ | J/mol |
| $A_{disl}$ | Constant for dislocation creep | 28968.6 | - |
| $E_{disl}$ | Activation energy for dislocation creep | $540 \times 10^3$ | J/mol |
| $R$ | Universal gas constant | 8.3145 | J/K·mol |
| $\eta_0$ | Background shear viscosity | $10^{19}$ | Pa·s |
| $\eta_{max}$ | Max shear viscosity | $10^{23}$ | Pa·s |
| $\alpha_s$ | Thermal expansivity from Solid adiabat | $3 \times 10^{-5}$ | K |
| $\kappa$ | Thermal diffusivity for mantle peridotities (Olivine) | $0.7272^{-6}$ | $m/s^2$ |
| $c_p$ | Heat capacity | 1200 | $m/s^2$ |
| $\beta$ | Dimensionless adiabatic gradient | $\frac{h\alpha g}{c_p}$ | - |
| $T_1$ | Mantle potential temperature | 1673 | K |
| $T_s$ | Surface temperature | 273 | K |
| $L$ | Latent heat for formation of melt for mantle peridotite | $4 \times 10^5$ | J/Kg |
| $F_{max}$ | Max degree of melting in model | 0.2 | - |
| $K_0$ | Background permeability | $4 \times 10^{-9}$ | - |

The main non-linear Newton solver in the fluid phase solves for porosity, compaction pressure and temperature, also using an FGMRES iterative method. We use a multiplicative fieldsplit preconditioner sequentially on compaction pressure, porosity then temperature. The compaction pressure block D is preconditioned with an algebraic multigrid solver (HYPRE) with a GMRES iterative method. Both the porosity and temperature fieldsplits uses iterative methods similar to those in the initial guess solver.

The numerical computations are done using the supercomputer COMET,

**Table 3.3**: Parameters used for example model

| Symbol | Definition | Value and units |
|---|---|---|
| $U_0$ | Spreading rate | 4 cm/yr |
| $R$ | Freezing rate constant | 200 $s^{-1}$ |
| $x_{pipe}$ | Width of initial porosity pipe | 100 m |
| $y_{pipe}$ | Depth of initial porosity pipe | 5 km |
| $m_p$ | Fanning gradient of initial porosity pipe | 100 |

part of the XSEDE program at University of California, San Diego. Our numerical models typically have 146,902 degrees of freedom and run for 48 hours on 12 cores on one node.

### 3.4.5 TerraFERMA

Our models are built using TerraFERMA, the Transparent Finite Element Rapid Model Assembler (*Wilson et al.*, 2017) to solve our governing set of non-linear equations. TerraFERMA provides considerable flexibility in model composition and numerical methods by leveraging the open source libraries, FEniCS (*Logg et al.*, 2011, 2012), PETSc (*Balay et al.*, 2017) and SPuD (*Ham et al.*, 2009). FEniCS provides a high level language for the description of weak forms and a form compiler for automatic code generation for assembly and mesh management. PETSc provides linear and non-linear solvers that are scalable. SPuD manages the options and provides a GUI interface to TerraFERMA. We present the open-source code in the form of TerraFERMA mark up language files (.tfml), which contain all the details of the numerical implementation we have described in this section.

## 3.5 Example model

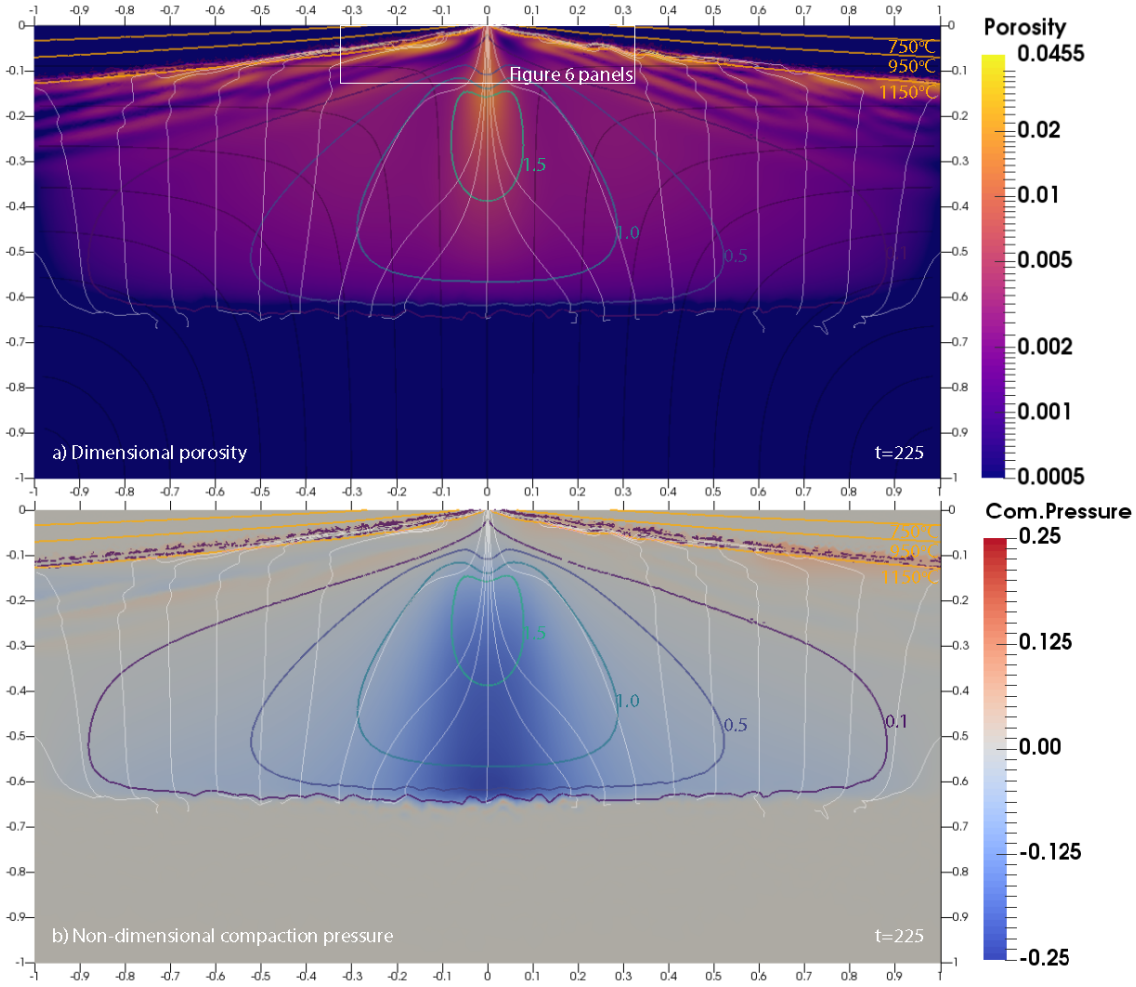


**Figure 3.5**: Snapshots of a) porosity and b) non-dimensional compaction pressure for our example model with intermediate spreading rate, $U_0 = 4$ cm/yr, at $t = 225$ (9.32 Myrs). The domain is 200 km wide and 100 km deep. White lines show fluid flow and black lines show solid flow. The closed labelled contours in the middle of the domain are for non-dimensional total melting rate, $\Gamma$. The melting region is roughly triangular in shape. Orange contours are for temperature and are labeled in degrees celsius. There are dark purple contours of freezing just above the orange contour for 1150°C.

Figure 3.5 (continued): a) Porosity or melt is mainly concentrated beneath the ridge axis (or in the middle of the domain) where melting rate is the largest and at decompaction layers on both sides of the ridge axis. There is a strong focusing of melt towards the axis deep in the melting region, away from the thermal boundary layers. The white box shows the domain for the panels in Figure 3.5. b) 0.1 non-dimensional units of pressure scales as 50 MPa. Compaction pressure is negative in the melting region and positive directly above each of the porosity waves.

We present an example model with intermediate half spreading rate, $U_0 = 4$ cm/yr, along with corresponding parameters for the initial porosity pipe (top snapshot, $t = 0$, in Figure 3.5) and freezing rate constant, $R$, given in Table 3.3. Porosity (melt) is mainly concentrated in two regions at $t \sim 225$ (9.32 Myrs) as shown in Figure 3.5a. One is beneath the ridge axis at about 5-40 km depth range, where the melting rate is highest. This agrees well with magnetotelleric observations at the East Pacific Rise (*Key et al.*, 2013). Even though the East Pacific Rise has a higher spreading rate than our example model, we expect the location of the highest melt region to remain similar whereas the amount of melt might change. The other high porosity region is along porosity waves that eventually travel upwards to the thermal boundary layer. These have been described as "decompaction melt layers" (e.g *Sparks and Parmentier* (1991); *Spiegelman* (1993c)) on either side of the ridge axis. This model runs to a maximum non-dimensional time of 300 (12.42 Myrs). Snapshots of the model are taken at $t \sim 225$ (9.32 Myrs) to compare with a case where all parameters were kept the same but the model domain is wider (Figure 3.6) that ran to a maximum time of $t \sim 225$ due to the limited computational resources available.

The corresponding non-dimensional compaction pressure is negative in the melting region (Figure 3.5b). Compaction pressure is most negative below the ridge axis, when the upwelling solid mantle starts to melt as it crosses the peridotite solidus. Compaction pressure is positive above the porosity waves on both sides, where the solid is decompacting to allow incoming melt. White melt flow lines in both panels a and b in Figure 3.5 show a strong melt focusing deep in the melting region, where the horizontal compaction pressure gradients are stronger. These flow lines bunch up where melting rate is the highest in the heart of the melting

region. On the sides, the melt flow lines are mostly vertical until the fluid leaves the melting region, traveling upwards in porosity waves. Melt in these porosity waves then gets deflected towards the ridge axis once it reaches the decompaction layers.

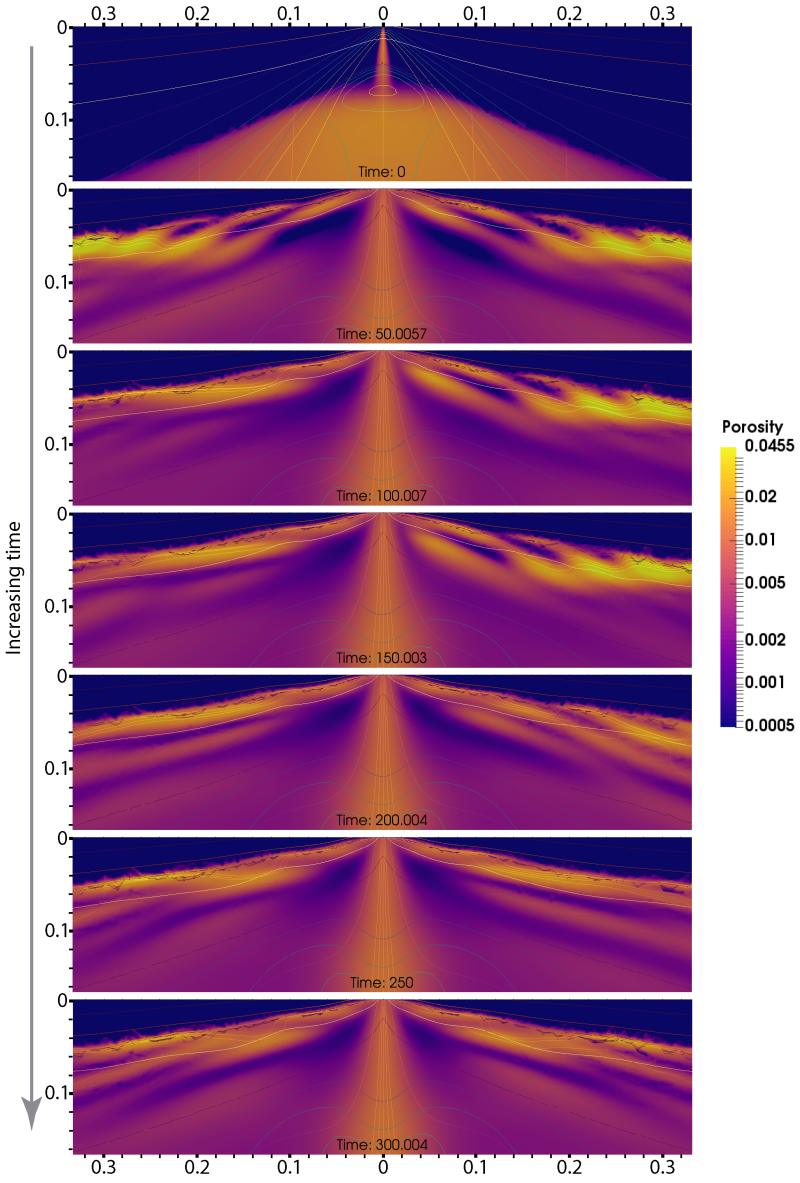


**Figure 3.5**: Six snapshots equally spaced in time show the evolution of porosity near the ridge axis for the example model with half-spreading rate of $U_0 = 4$ cm/yr. Each panel is taken from the white box in Figure 3.5a at the respective times. The panels are 78 km wide and 16 km deep. Consecutive snapshots are spaced $\sim 50$ non-dimensional time or $\sim$2.07 Myrs.

Figure 3.5 (continued): The top snapshot shows the porosity initial condition at $t = 0$. The subsequent snapshots show higher porosity regions in the center beneath the ridge axis and in the porosity waves on both sides above the melting region. The higher porosity region in the center does not change with time over the evolution of the numerical model. In contrast, the porosity waves are time-dependent and evolve throughout the time evolution of the numerical model. In some snapshots, the porosity wave structure is asymmetric across the ridge axis.

Snapshots of the porosity at equally spaced times between $t = 0$ and $t = 300$ shows the porosity evolution near the ridge axis (Figure 3.5). At the beginning of the numerical simulation (top panel in Figure 3.5), there is no melt outside of the melting region and the initial porosity pipe. The model goes through a transient period of time when porosity/melt generated in the melting region travels upwards to the ridge or lithosphere-asthenosphere boundary. On the sides of the subaxial zone, the top of the melting region sheds porosity waves towards the thermal boundary layer. The distance between the melting region and the thermal boundary increases away from the ridge axis, so the porosity waves reach the thermal boundary first near the ridge axis and last furthest away from the ridge axis. This is especially clear in the model run with a wider domain shown in Figure 3.6 ($300 \times 100$ km domain). This transient time is short ($\sim 45$ non-dimensional time) compared to the entire length of the model run of $t = 300$.

The porosity waves lead to small time-dependent fluctuations in porosity, compaction pressure and melt flux (Figure 3.5). The porosity waves are local effects and lead to small asymmetries in the porosity field (Figures 3.5). White melt flow lines in Figure 3.5 show that melt segregation near the center of the domain does not vary significantly with time.

To make sure that the boundary conditions on the sides do not affect the overall solution and that the smaller domain captures the main physics to first order, we ran a model using a wider domain of 300 km (Figure 3.6). The wider model shows no significant difference compared to the narrow model.

Our example model produces $\sim 6 - 6.5$ km of oceanic crust (Figure 3.7a), within the observational average oceanic crustal thicknesses of $\sim 6 - 7$ km (*White et al.*, 1992; *Bown and White*, 1994; *White et al.*, 2001; *Harding et al.*, 2017). The

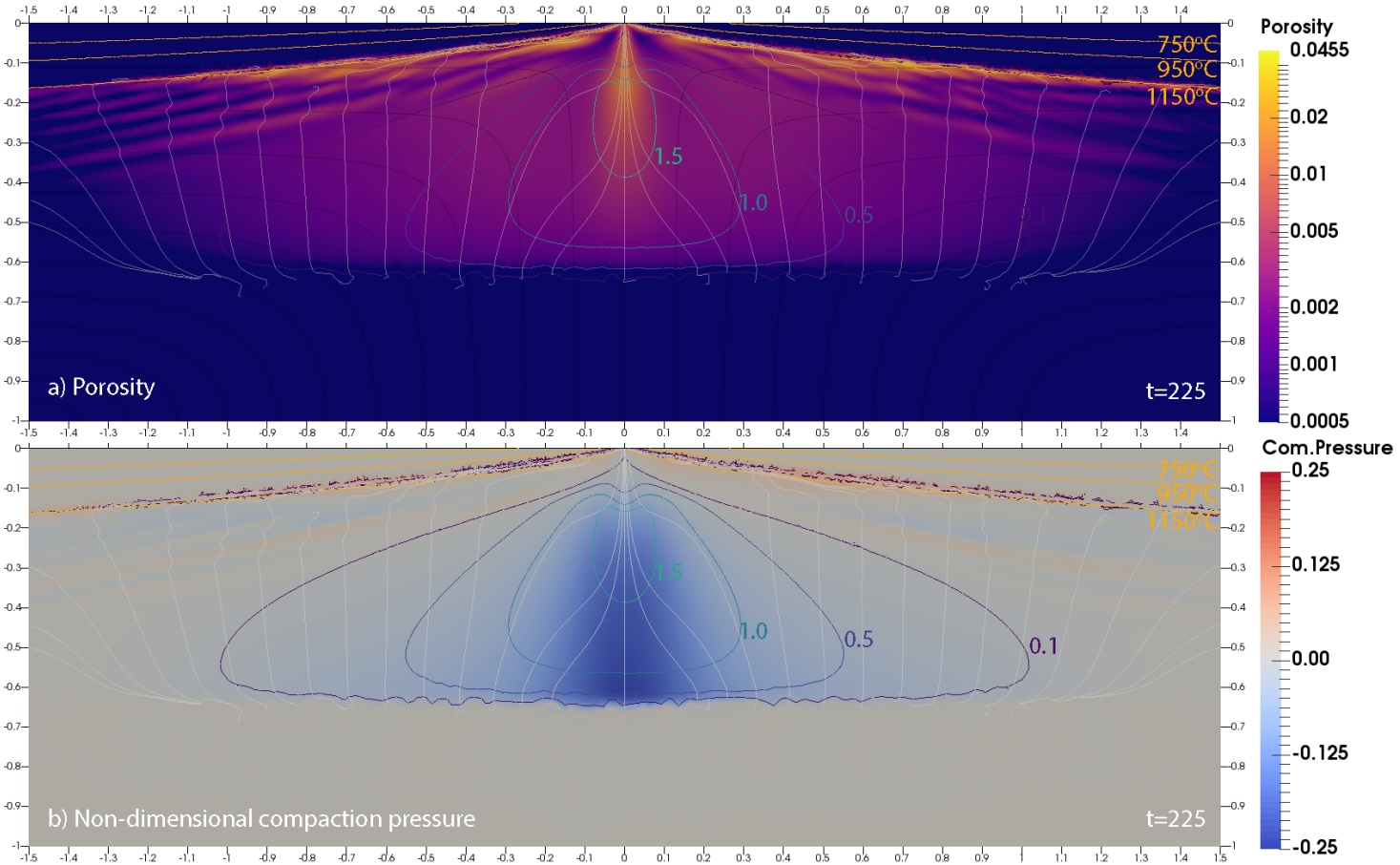


**Figure 3.6**: A snapshot of a) porosity and b) non-dimensional compaction pressure for the same model run as in figure 3.5 with wider domain to explore boundary effects. There is no significant difference between the wider and narrower run.

crustal thickness is calculated using the integral of the melt flux that leaves the top boundary $\int \mathbf{q} ds_{top}$, assuming an oceanic crustal density of $\rho_c = 2800$ kg/m$^3$ (same as melt density, $\rho_f$). The average crustal thickness produced is about 6.09 km for the narrow model and 6.37 km for the wider model. The difference between the two crustal thicknesses produced is $< 5\%$ of the mean ($\sim 6.23$ km). Most of the melting occurs beneath the ridge axis. A significant portion of melt focusing occurs near the ridge axis and not away from it. Therefore, even with a smaller domain, most of the focusing effect and melt produced to form oceanic crust are captured. The porosity profiles taken across the domain at depth 5 km for both the narrow and wide runs show no significant difference for that time snapshot (Figure 3.7b). We emphasize that the use of a smaller domain saves significant computational time.

There is a transient time of large fluctuations before the system settles into a quasi-steady state after about 1 Myr (Figure 3.7a), where crustal production oscillates with an amplitude of $\sim$200 m and period of $\sim$130 kyrs. After about 8 Myrs, these oscillations reduce in amplitude and are replaced by a saw tooth pattern with lower amplitude and longer duration that becomes well established after about 10 Myrs. These are a result of porosity waves, shedding above the melting region on either side of the domain, accumulating in the decompaction layers that focus melt to the ridge axis. These porosity waves can also be observed beyond 10 km away from the ridge axis in Figure 3.7b, which shows porosity across the domain at 5 km depth.

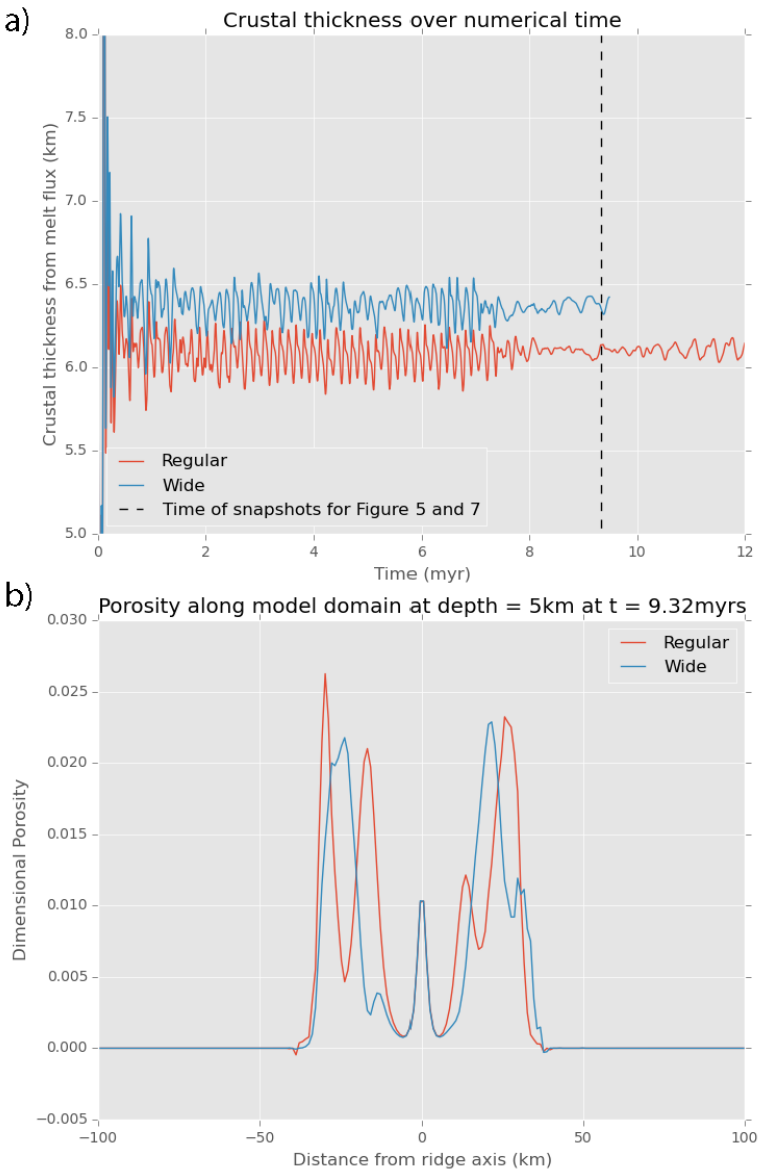


**Figure 3.7**: a) Crustal production for the narrow and wide domain runs over time. Crustal thickness is calculated using the accumulated melt flux leaving the top boundary assuming an oceanic crustal density of $\rho_c = 2800$ kg/m$^3$. The red and blue lines represent the crustal production from the narrow and wide domain runs respectively. There is a clear transient time at the beginning where the crustal production varied much more over a short period of time.

Figure 3.7 (continued) b) Porosity profiles taken across the width of domain at depth of 5 km and at time, $t\sim225$ or 9.32 Myrs (same time as in both Figures 3.5 and 3.6), for both the narrow and wide models. The higher porosity region in the center is identical in both models. The time-dependent porosity waves on the sides that accumulate in the decompaction layers are of similar magnitudes and width for both the models.

### 3.5.1 Magmatic focusing

A dominant focusing mechanism in these models can be seen in Figures 3.5 and 3.6, which show a dramatic focusing of melt flow well beneath the thermal boundary layer towards the center of the melting region. This mechanism is different from the melt focusing due to incompressible corner flow (*Spiegelman and McKenzie*, 1987; *Phipps-Morgan*, 1987) or the flow along decompaction channels near the base of the cooling lithosphere (*Sparks and Parmentier*, 1991; *Hebert and Montési*, 2010), although some of that mechanism is present in our example model as well.

All previously published two-phase mid-ocean ridge models begin with the same fundamental equations but each model makes different choices for approximations which can change the dominant physics in the problem (e.g zero compaction length approximation, small porosity approximation). The various focusing mechanisms proposed here exist in any model that is based on the full "McKenzie" equations that include pressure gradients due to viscous deformation. Each focusing mechanism might not manifest itself due to specific model choices for the constitutive relations. A category of two phase models assumes that compaction length, $\delta$, is small compared to the geologic length scale of the model problem (zero compaction length approximation), therefore the associated pressure gradients are insignificant (e.g *Ribe* (1985); *Buck and Su* (1989); *Sotin and Parmentier* (1989)). These models with only buoyancy driven melt flow will not have any of the melt focusing effects from pressure gradients due to viscous deformation. These models, when applied to the mid-ocean ridge setting, tend to suggest a narrow high porosity partially molten region beneath the ridge axis, where focusing melt to the ridge axis is less of a problem. However, geophysical observations seem to

suggest otherwise (*Forsyth et al.*, 1998a,b; *Key et al.*, 2013). Two phase modeling efforts without the zero compaction length assumption have been able to emulate the wide region of partially molten mantle beneath mid-ocean ridges (*Ghods and Arkani-Hamed*, 2000; *Katz*, 2008).

Melt flows due to pressure gradients. With the pressure decomposition (Equation 3.9) in our model and some previous models (*Hebert and Montési*, 2010; *Keller and Katz*, 2016), the pressure gradient is split into compaction pressure, dynamic pressure and buoyancy in the Darcy-like flow equation (Equation 3.5):

$$\phi(\mathbf{v_f} - \mathbf{v_s}) = -\frac{K}{\mu}[\nabla\mathcal{P} + \nabla p^* + \Delta\rho\mathbf{g}] \tag{3.60}$$

The non-dimensionalized buoyancy term is of order unity such that all the generated melt flows upwards, as indicated by $\hat{\mathbf{k}}$ in Equation 3.48. The other two pressure gradients will move melt horizontally if the gradient in the horizontal direction is comparable to the buoyancy term, therefore focusing melt. Compaction and dynamic pressures depend on volumetric and shear deformations respectively. Thus, the specific rheological relations for bulk and shear viscosities in these models play an important role in determining the focusing mechanisms observed.

In our example model, buoyancy moves melt upwards everywhere in the model domain, as shown by the background lithostatic pressure in Figure 3.8. The compaction pressure is significant in a large area compared to the dynamic pressure, which is only important near the ridge axis at the top. Therefore, horizontal melt flows or melt focusing is largely due to gradients in compaction pressures as opposed to dynamic pressure in our example model. The ridge-suction pressure gradient described in *Spiegelman and McKenzie* (1987) affects a region of length scale, $L = \sqrt{\eta U_0/\Delta\rho g}$, near the ridge axis. For shear viscosities of order $10^{19}$ used in our example model, this length scale is $\sim$1.59 km, which is confined to a small region near the ridge axis (inset of Figure 3.8). Compaction pressure is negative for most of the melting region but the structure of the contours (most negative on axis) shows how the compaction pressure gradient would move melt horizontally towards the ridge axis, deep in the melting region.

The new focusing mechanism seen here has only been recognized recently (*Turner et al.*, 2017) and in this work. *Turner et al.* (2017) uses a variable non-

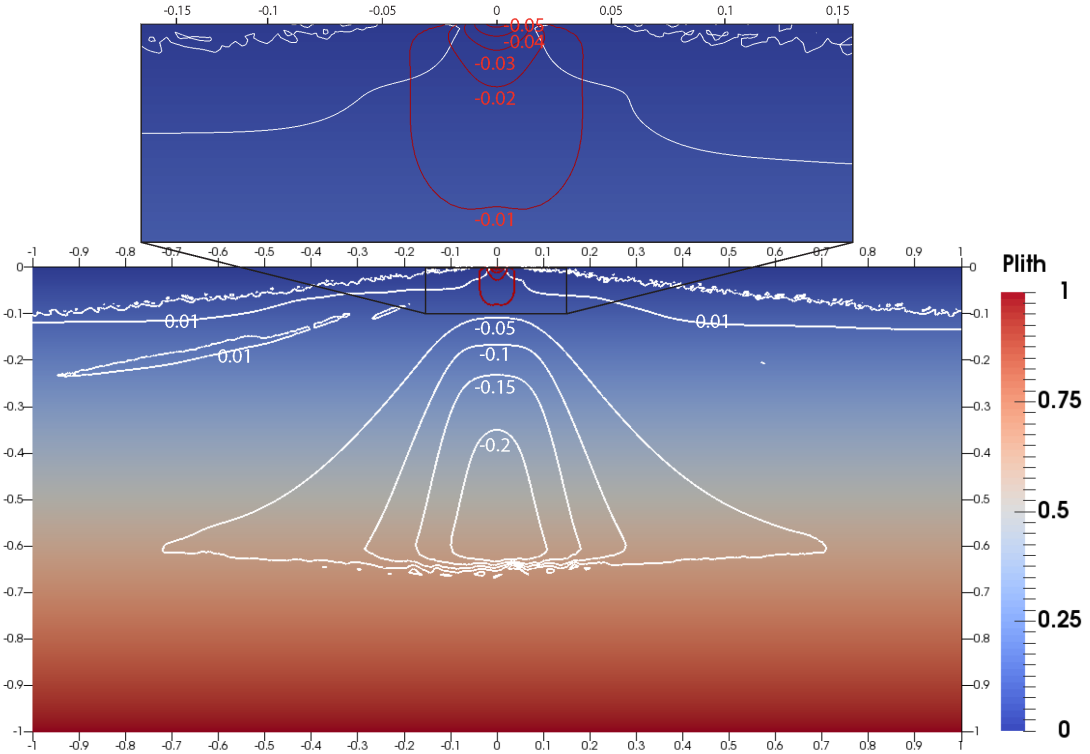


**Figure 3.8**: A composite of non-dimensional dynamic, compaction and lithostatic pressures in the example model taken at $t$∼225. The background color shows lithostatic pressure, white contours are for compaction pressure and red contours are for dynamic pressure. A black zoomed in box shows the dynamic pressure near the ridge. All numbers are in non-dimensional units, where all pressures scale as $P' = 1$ is 500 MPa ($\Delta\rho g h$).

linear rheology which has a grain size dependence along with an equation for grain growth. They report seeing this new focusing mechanism as we do in this work, although we use variable viscosity with no grain size dependence. We propose that the reason behind this focusing mechanism is simple. In near quasi steady state, the conservation of mass for porosity (Equation 3.2) shows that the compaction of the solid matrix balances melting:

$$0 = \nabla \cdot \mathbf{v_s} + \Gamma/\rho_s \tag{3.61}$$

However, the compaction pressure is defined as $\mathcal{P} = \zeta \nabla \cdot \mathbf{v_s}$ (Equation 3.10) and scales as the bulk viscosity, thus, in quasi steady state, we have

$$\mathcal{P} = -\zeta\Gamma/\rho_s \tag{3.62}$$

Therefore, the structure of the compaction pressure is controlled by the melting rate field and the scale depends on the bulk viscosity. The melt production rate, $\Gamma$, is highest beneath the ridge axis and its structure is largely determined by the solid upwelling field. Hence, this melt focusing mechanism or melting rate focusing is a result of the horizontal gradients in compaction pressure due to the structure of the melting rate field and is strongly dependent on the bulk viscosity specified in the models. In our example mode, this relatively new melt focusing mechanism focuses a significant portion of the melt produced deep in the melting region.

Outside of the region where melt is focused by the melting rate focusing, buoyancy dominates as indicated by the vertical melt flow lines in Figures 3.5 and 3.6. Melt traveling upwards encounters a thermal boundary layer, where decompaction melt channels form to move melt diagonally upwards towards the ridge axis, thus focusing melt (*Sparks and Parmentier*, 1991; *Spiegelman*, 1993b; *Hebert and Montési*, 2010). Some melt freezes/metasomatizes into the lithosphere. There is a clear distinction between melt from the central high porosity region that is focused deep in the melting region and the melt from the decompaction layers on either side of the ridge axis (Figure 3.7b).

## 3.6 Discussion

Our models are one way coupled so that the solid velocity and dynamic pressure in the solid system are not affected by the fluid flow system. While still capturing the main dynamics of the system, the problem becomes less computationally expensive since a full Stokes solve at every time-step is avoided. However, one-way coupling leads to an inconsistency in mass conservation. The solid velocity is not adjusted to move up faster as melt is produced and extracted/segregated. This is a minor contribution and might allow slightly more melt to be produced than the predicted 6 km as shown in Figure 3.7a. This inconsistency could be corrected simply by adding a correction term to the solid velocity.

One advantage of using TerraFERMA is that it is flexible. It allows us to build on this current model and expand it to be fully coupled. This flexibility is an important design feature of TerraFERMA and other software such as ComSol (www.comsol.com) and Underworld2 (*Moresi et al.*, 2007). For these types of complex highly coupled problems, the flexibility gives it an advantage over other software that can be purpose specific and therefore difficult to modify. An example of fully coupled ridge model with an isoviscous rheology is included in the primary TerraFERMA paper (*Wilson et al.*, 2017).

Our numerical models are passively driven by a Dirichlet condition that sets the solid velocity at the top boundary to be plate spreading rate. Geophysical observations of asymmetric upwelling suggest buoyancy driven flow beneath some mid-ocean ridges (*Hammond and Toomey*, 2003; *Dunn and Forsyth*, 2003; *Baba et al.*, 2006). However, a combined geochemical and dynamical study suggests that passively driven upwelling seems more consistent with observations (*Spiegelman and Reynolds*, 1999). Furthermore, symmetry in a highly conductive region beneath the East Pacific Rise is interpreted to be evidence for passively driven flow (*Key et al.*, 2013).

Magnetotelluric (MT) resistivity imaging of the East Pacific Rise with half spreading rate of 5.5 cm/yr, suggests that there is one main conductor interpreted as partially molten mantle, $\sim 20-40$ km beneath the ridge axis (*Key et al.*, 2013). The shallow uppermost mantle is largely resistive, suggesting a lack of porosity.

Previous models (*Sparks and Parmentier*, 1991; *Hebert and Montési*, 2010; *Keller and Katz*, 2016), and models presented in this paper, suggest that decompaction layers with higher porosity should exist in these areas, where it is geophysically observed to be largely unmolten. MT is sensitive to conductors but less so to resistors. Perhaps the shallow uppermost mantle is less resistive than thought but the inversion methods puts the resistors there because of the strong conductor in the middle depths. However, if this observation is accurate, then it is possible that melt focusing from melting rate gradients might be much stronger than shown here. To strengthen this effect requires either increasing the melting rate (without changing the total melt production) or increasing the bulk viscosity. If this new magmatic focusing is stronger, it is possible that most melt will be focused within the melting region before reaching the thermal boundary layer.

*Katz et al.* (2003) provides a convenient parameterization of melting that combines some understanding of melting theory calibrated to laboratory experiments for a fixed bulk peridotite composition. For a reasonable mantle temperature, it predicts sensible amounts of melt production and crustal thickness without any tuning. Both the parameterization and the Hirschman peridotite solidus (*Hirschmann*, 2000) used are calibrated to fit experimental and observational data. We use the dry solidus melting instead of wet solidus melting to explore the two-phase dynamics without the complication of adding volatiles. The wet solidus melting merely depresses the solidus, giving a long low tail in melt production. This long tail does not add significantly to the total amount of melt produced. Our parameterized melting model does not track compositional change as melt is generated, which in reality changes the chemical composition, thus density, of the residual.

The strength of the melting rate focusing effect demonstrated here depends crucially on the magnitude of the bulk viscosity. In some early works, it was assumed that $\zeta \sim \eta$ and thus in the convecting mantle for $\eta \sim 10^{19}$ Pa s, this new focusing effect would be small. Later on, other models assumed $\zeta = \eta/\phi$ or other similar formulations but the porosity dependence of bulk viscosity was treated as a free parameter. Bulk viscosity is an effective property of the two-phase medium

that depends on the distribution and micro-mechanics of melt and solid at the grain scale. To put better bounds on both bulk viscosity and permeability (which also depends on microscale geometry), *Simpson et al.* (2010a,b) used homogenization theory to upscale equations for a mixture of two interpenetrating Stokes fluids with very different viscosities. They showed that the homogenization of this problem was consistent with the McKenzie equations if $\zeta = \eta/\phi$. This makes sense as the system of equations for multi-phase flow should reduce to incompressible stokes flow for the solid at zero porosity to be consistent with the standard equations for mantle convection. Using $\eta/\phi$ causes the bulk viscosity to increase by several orders of magnitude for small porosities. Recent work on homogenization of other viscosity mechanisms (*Rudge*, 2017) provide additional functional relationships between $\zeta$, $\eta$ and $\phi$, which should be systematically investigated.

## 3.7 Conclusion

We present new open-source two-phase flow models (M3LT) to understand magma dynamics beneath mid-ocean ridges. These models are built using TerraFERMA and consist of a set of structured input files for TerraFERMA that describe all the model choices required to solve the complex two-phase models described here. By building M3LT on TerraFERMA, we provide a consistent mechanism for reproducing, understanding and potentially modifying published models in a way that the derived models can also be used and shared. As a note of caution however, highly non-linear models such as these can be sensitive to small changes in parameters or constitutive relationships. A key design feature of TerraFERMA, inherited from the underlying FEniCS and PETSc libraries, is to give the user sufficient flexibility in changing computational strategies (solvers, meshes, time-stepping) to help mitigate the fragility of complex models.

We described in detail the model set up for our example model with half spreading rate of $U_0 = 4$ cm/yr. We discuss the various focusing mechanisms seen in our example model, highlighting the recently recognized melting rate focusing mechanism and the physics behind it. The melting rate focusing mechanism is a natural consequence of the two-phase flow equations, creating a compaction

pressure suction from the melting rate gradient. In the example model presented in this paper, this mechanism focuses a significant proportion of the melt generated from a wide region beneath the mid-ocean ridges to a small area and may explain two of the fundamental observations of mid-ocean ridges, the extreme narrowness of the neo-volcanic zone and the relative constancy of crustal thickness independent of spreading rate for intermediate to fast spreading ridges.

Chapter 3, in part, has been submitted for publication of the material as it may appear in Gcubed, 2018, Shi Sim, Marc Spiegelman, Dave R Stegman and Cian Wilson, 2018. The dissertation/thesis author was the primary investigator and author of this paper. I would like to acknowledge my co-authors, Marc Spiegelman, Dave R Stegman and Cian Wilson.

# References

Aharonov, E., J. Whitehead, P. Kelemen, and M. Spiegelman (1995), Channeling instability of upwelling melt in the mantle, *Journal of Geophysical Research: Solid Earth*, *100*(B10), 20,433–20,450.

Baba, K., A. D. Chave, R. L. Evans, G. Hirth, and R. L. Mackie (2006), Mantle dynamics beneath the east pacific rise at 17 S: Insights from the mantle electromagnetic and tomography (melt) experiment, *Journal of Geophysical Research: Solid Earth*, *111*(B2).

Balay, S., S. Abhyankar, M. F. Adams, J. Brown, P. Brune, K. Buschelman, L. Dalcin, V. Eijkhout, W. D. Gropp, D. Kaushik, M. G. Knepley, L. C. McInnes, K. Rupp, B. F. Smith, S. Zampini, H. Zhang, and H. Zhang (2016), PETSc users manual, *Tech. Rep. ANL-95/11 - Revision 3.7*, Argonne National Laboratory.

Balay, S., S. Abhyankar, M. F. Adams, J. Brown, P. Brune, K. Buschelman, L. Dalcin, V. Eijkhout, W. D. Gropp, D. Kaushik, M. G. Knepley, D. A. May, L. C. McInnes, K. Rupp, P. Sanan, B. F. Smith, S. Zampini, H. Zhang, and H. Zhang (2017), PETSc users manual, *Tech. Rep. ANL-95/11 - Revision 3.8*, Argonne National Laboratory.

Bercovici, D., and Y. Ricard (2003), Energetics of a two-phase model of lithospheric damage, shear localization and plate-boundary formation, *Geophysical Journal International*, *152*(3), 581–596.

Bercovici, D., Y. Ricard, and G. Schubert (2001a), A two-phase model for compaction and damage: 1. general theory, *Journal of Geophysical Research: Solid Earth*, *106*(B5), 8887–8906.

Bercovici, D., Y. Ricard, and G. Schubert (2001b), A two-phase model for compaction and damage: 3. applications to shear localization and plate boundary formation, *Journal of Geophysical Research: Solid Earth*, *106*(B5), 8925–8939.

Bown, J. W., and R. S. White (1994), Variation with spreading rate of oceanic crustal thickness and geochemistry, *Earth and Planetary Science Letters*, *121*(3-4), 435–449.

Buck, W. R., and W. Su (1989), Focused mantle upwelling below mid-ocean ridges due to feedback between viscosity and melting, *Geophysical Research Letters*, *16*(7), 641–644.

Carbotte, S. M., D. K. Smith, M. Cannat, and E. M. Klein (2016), Tectonic and magmatic segmentation of the global ocean ridge system: A synthesis of observations, *Geological Society, London, Special Publications*, *420*(1), 249–295.

Cooper, R., and D. Kohlstedt (1984), Solution-precipitation enhanced diffusional creep of partially molten olivine-basalt aggregates during hot-pressing, *Tectonophysics*, *107*(3-4), 207–233.

Dullien, F. A. (2012), *Porous media: fluid transport and pore structure*, Academic press.

Dunn, R. A., and D. W. Forsyth (2003), Imaging the transition between the region of mantle melt generation and the crustal magma chamber beneath the southern east pacific rise with short-period love waves, *Journal of Geophysical Research: Solid Earth*, *108*(B7).

Faul, U. H. (2001), Melt retention and segregation beneath mid-ocean ridges, *Nature*, *410*(6831), 920.

Forsyth, D. W., S. C. Webb, L. Dorman, and Y. Shen (1998a), Phase velocities of Rayleigh waves in the MELT experiment on the East Pacific Rise, *Science*, *280*(5367), 1235–1238.

Forsyth, D. W., D. S. Scheirer, S. C. Webb, and L. M. Dorman (1998b), Imaging the deep seismic structure beneath a mid-ocean ridge: The MELT experiment, *Science*, *280*(5367), 1215–1220.

Fowler, A. (1985), A mathematical model of magma transport in the asthenosphere, *Geophysical & Astrophysical Fluid Dynamics*, *33*(1-4), 63–96.

Geuzaine, C., and J.-F. Remacle (2009), Gmsh: A 3-d finite element mesh generator with built-in pre-and post-processing facilities, *International journal for numerical methods in engineering*, *79*(11), 1309–1331.

Ghods, A., and J. Arkani-Hamed (2000), Melt migration beneath mid-ocean ridges, *Geophysical Journal of the Royal Astronomical Society*, *140*(3), 687–697.

Ham, D., P. Farrell, G. Gorman, J. Maddison, C. Wilson, S. Kramer, J. Shipton, G. Collins, C. Cotter, and M. Piggott (2009), Spud 1.0: generalising and automating the user interfaces of scientific computer models, *Geoscientific Model Development*, *2*(1), 33.

Hammond, W. C., and D. R. Toomey (2003), Seismic velocity anisotropy and heterogeneity beneath the mantle electromagnetic and tomography experiment (melt) region of the east pacific rise from analysis of p and s body waves, *Journal of Geophysical Research: Solid Earth*, *108*(B4).

Harding, J. L., H. J. Van Avendonk, N. W. Hayman, I. Grevemeyer, C. Peirce, and A. Dannowski (2017), Magmatic-tectonic conditions for hydrothermal venting on an ultraslow-spread oceanic core complex, *Geology*, *45*(9), 839–842.

Hebert, L. B., and L. G. Montési (2010), Generation of permeability barriers during melt extraction at mid-ocean ridges, *Geochemistry, Geophysics, Geosystems*, *11*(12).

Herzberg, C., P. Raterron, and J. Zhang (2000), New experimental observations on the anhydrous solidus for peridotite KLB-1, *Geochemistry, Geophysics, Geosystems*, *1*(11).

Hirose, K., and I. Kushiro (1993), Partial melting of dry peridotites at high pressures: determination of compositions of melts segregated from peridotite using aggregates of diamond, *Earth and Planetary Science Letters*, *114*(4), 477–489.

Hirschmann, M. M. (2000), Mantle solidus: Experimental constraints and the effects of peridotite composition, *Geochemistry, Geophysics, Geosystems*, *1*(10).

Hirth, G., and D. Kohlstedt (2003), Rheology of the upper mantle and the mantle wedge: A view from the experimentalists, *Inside the subduction Factory*, 83–105.

Holtzman, B., D. Kohlstedt, M. Zimmerman, F. Heidelbach, T. Hiraga, and J. Hustoft (2003a), Melt segregation and strain partitioning: implications for seismic anisotropy and mantle flow, *Science*, *301*(5637), 1227–1230.

Holtzman, B., N. Groebner, M. Zimmerman, S. Ginsberg, and D. Kohlstedt (2003b), Stress-driven melt segregation in partially molten rocks, *Geochemistry, Geophysics, Geosystems*, *4*(5).

Jha, K., E. Parmentier, and J. P. Morgan (1994), The role of mantle-depletion and melt-retention buoyancy in spreading-center segmentation, *Earth and Planetary Science Letters*, *125*(1-4), 221–234.

Karato, S.-i., and P. Wu (1993), Rheology of the upper mantle: a synthesis, *Science*, *260*(5109), 771–778.

Katz, R. F. (2008), Magma Dynamics with the Enthalpy Method: Benchmark Solutions and Magmatic Focusing at Mid-ocean Ridges, *Journal of Petrology*, *49*(12), 2099–2121.

Katz, R. F. (2010), Porosity-driven convection and asymmetry beneath mid-ocean ridges, *Geochemistry, Geophysics, Geosystems*, *11*(11).

Katz, R. F., M. Spiegelman, and C. H. Langmuir (2003), A new parameterization of hydrous mantle melting, *Geochemistry, Geophysics, Geosystems*, *4*(9).

Katz, R. F., M. Spiegelman, and B. Holtzman (2006), The dynamics of melt and shear localization in partially molten aggregates, *Nature*, *442*(7103), 676–679.

Keller, T., and R. F. Katz (2016), The Role of Volatiles in Reactive Melt Transport in the Asthenosphere, *Journal of Petrology*, *57*(6), 1073–1108.

Keller, T., D. A. May, and B. J. P. Kaus (2013), Numerical modelling of magma dynamics coupled to tectonic deformation of lithosphere and crust, *Geophysical Journal of the Royal Astronomical Society*, *195*(3), 1406–1442.

Keller, T., R. F. Katz, and M. M. Hirschmann (2017), Volatiles beneath mid-ocean ridges: Deep melting, channelised transport, focusing, and metasomatism., *Earth and Planetary Science Letters*, *464*, 55–68.

Key, K., S. Constable, L. Liu, and A. Pommier (2013), Electrical image of passive mantle upwelling beneath the northern East Pacific Rise, *Nature*, *495*(7442), 499–502.

Kohlstedt, D. L., and B. K. Holtzman (2009), Shearing melt out of the earth: An experimentalist's perspective on the influence of deformation on melt extraction, *Annual Review of Earth and Planetary Sciences*, *37*, 561–593.

Kohlstedt, D. L., Q. Bai, Z.-C. Wang, and S. Mei (2000), Rheology of partially molten rocks, in *Physics and Chemistry of Partially Molten Rocks*, 3–28.

Logg, A., K. Ølgaard, M. Rognes, G. Wells, J. Jansson, R. Kirby, M. Knepley, D. Lindbo, and O. Skavhaug (2011), The fenics project, *GNU Free Documentation License*, *1*(5.5).

Logg, A., K.-A. Mardal, and G. Wells (2012), *Automated solution of differential equations by the finite element method: The FEniCS book*, (Vol. 84), Springer Science & Business Media.

Longhi, J. (2002), Some phase equilibrium systematics of lherzolite melting: I, *Geochemistry Geophysics Geosystems*, *3*(3), 1–33.

Macdonald, K. C. (1982), Mid-ocean ridges: Fine scale tectonic, volcanic and hydrothermal processes within the plate boundary zone, *Annual Review of Earth and Planetary Sciences*, *10*(1), 155–190.

McDonough, W. F., and R. L. Rudnick (1998), Mineralogy and composition of the upper mantle, *Reviews in mineralogy*, *37*, 139–164.

McKenzie, D. (1984), The Generation and Compaction of Partially Molten Rock, *Journal of Petrology*, 1–53.

McKenzie, D., and M. Bickle (1988), The volume and composition of melt generated by extension of the lithosphere, *Journal of petrology*, *29*(3), 625–679.

Mei, S., W. Bai, T. Hiraga, and D. Kohlstedt (2002), Influence of melt on the creep behavior of olivine–basalt aggregates under hydrous conditions, *Earth and Planetary Science Letters*, *201*(3), 491–507.

Miller, K. J., W.-l. Zhu, L. G. J. Montési, and G. A. Gaetani (2014), Experimental quantification of permeability of partially molten mantle rock, *Earth and Planetary Science Letters*, *388*, 273–282.

Miller, K. J., W.-l. Zhu, L. G. J. Montési, G. A. Gaetani, V. Le Roux, and X. Xiao (2016), Experimental evidence for melt partitioning between olivine and orthopyroxene in partially molten harzburgite, *Journal of Geophysical Research-Solid Earth*, *121*(8), 5776–5793.

Moresi, L., S. Quenette, V. Lemiale, C. Meriaux, B. Appelbe, and H.-B. Mühlhaus (2007), Computational approaches to studying non-linear dynamics of the crust and mantle, *Physics of the Earth and Planetary Interiors*, *163*(1-4), 69–82.

Parsons, B. (1981), The rates of plate creation and consumption, *Geophysical Journal International*, *67*(2), 437–448.

Phipps-Morgan, J. (1987), Melt migration beneath mid?ocean spreading centers, *Geophysical Research Letters*, *14*(12), 1238–1241.

Ribe, N. M. (1985), The deformation and compaction of partial molten zones, *Geophysical Journal International*, *83*(2), 487–501.

Ribe, N. M. (1987), Theory of melt segregation: a review, *Journal of volcanology and geothermal research*, *33*(4), 241–253.

Ricard, Y., D. Bercovici, and G. Schubert (2001), A two-phase model for compaction and damage: 2. applications to compaction, deformation, and the role of interfacial surface tension, *Journal of Geophysical Research: Solid Earth*, *106*(B5), 8907–8924.

Rudge, J. F. (2017), Textural equilibrium melt geometries around tetrakaidecahedral grains, *arXiv preprint arXiv:1709.03303*.

Rudge, J. F., D. Bercovici, and M. Spiegelman (2010), Disequilibrium melting of a two phase multicomponent mantle, *Geophysical Journal International*, *184*(2), 699–718.

Schmeling, H., N. Bagdassarov, D. Laporte, and A. Thompson (2000), Partial melting and melt segregation in a convecting mantle, *Physics and Chemistry of Partially Molten Rocks*, *11*, 141–178.

Scott, D. R., and D. J. Stevenson (1984), Magma solitons, *Geophysical Research Letters*, *11*(11), 1161–1164.

Scott, D. R., and D. J. Stevenson (1986), Magma ascent by porous flow, *Journal of Geophysical Research: Solid Earth*, *91*(B9), 9283–9296.

Simpson, G., M. Spiegelman, and M. I. Weinstein (2010a), A multiscale model of partial melts: 1. effective equations, *Journal of Geophysical Research: Solid Earth*, *115*(B4).

Simpson, G., M. Spiegelman, and M. I. Weinstein (2010b), A multiscale model of partial melts: 2. numerical results, *Journal of Geophysical Research: Solid Earth*, *115*(B4).

Sotin, C., and E. Parmentier (1989), Dynamical consequences of compositional and thermal density stratification beneath spreading centers, *Geophysical Research Letters*, *16*(8), 835–838.

Sparks, D. W., and E. M. Parmentier (1991), Melt extraction from the mantle beneath spreading centers, *Earth and Planetary Science Letters*, *105*(4), 368–377.

Spiegelman, M. (1993a), Flow in deformable porous media. Part 1 Simple analysis, *Journal of Fluid Mechanics*, *247*, 17–38.

Spiegelman, M. (1993b), Flow in deformable porous media. Part 2 numerical analysis–the relationship between shock waves and solitary waves, *Journal of Fluid Mechanics*, *247*, 39–63.

Spiegelman, M. (1993c), Physics of Melt Extraction: Theory, Implications and Applications, *Philosophical Transactions of the Royal Society A: Mathematical, Physical and Engineering Sciences*, *342*(1663), 23–41.

Spiegelman, M. (1996), Geochemical consequences of melt transport in 2-D: The sensitivity of trace elements to mantle dynamics, *Earth and Planetary Science Letters*, *139*(1-2), 115–132.

Spiegelman, M., and T. Elliott (1993), Consequences of melt transport for uranium series disequilibrium in young lavas, *Earth and Planetary Science Letters*, *118*(1-4), 1–20.

Spiegelman, M., and D. McKenzie (1987), Simple 2-d models for melt extraction at mid-ocean ridges and island arcs, *Earth and Planetary Science Letters*, *83*(1-4), 137–152.

Spiegelman, M., and J. R. Reynolds (1999), Combined dynamic and geochemical evidence for convergent melt flow beneath the east pacific rise, *Nature*, *402*(6759), 282–285.

Spiegelman, M., P. B. Kelemen, and E. Aharonov (2001), Causes and consequences of flow organization during melt transport: The reaction infiltration instability in compactible media, *Journal of Geophysical Research: Solid Earth*, *106*(B2), 2061–2077.

Spiegelman, M., D. A. May, and C. R. Wilson (2016), On the solvability of incompressible Stokes with viscoplastic rheologies in geodynamics, *Geochemistry Geophysics Geosystems*, *17*(6), 2213–2238.

Tosi, N., C. Stein, L. Noack, C. Hüttig, P. Maierova, H. Samuel, D. R. Davies, C. R. Wilson, S. C. Kramer, C. Thieulot, et al. (2015), A community benchmark for viscoplastic thermal convection in a 2-d square box, *Geochemistry, Geophysics, Geosystems*, *16*(7), 2175–2196.

Turner, A. J., R. F. Katz, M. D. Behn, and T. Keller (2017), Magmatic focusing to mid-ocean ridges: The role of grain-size variability and non-newtonian viscosity, *Geochemistry Geophysics Geosystems*, *23*(1), 15.

Wark, D. A., and E. B. Watson (1998), Grain-scale permeabilities of texturally equilibrated, monomineralic rocks, *Earth and Planetary Science Letters*, *164*(3-4), 591–605.

White, R. S., D. McKenzie, and R. K. O'Nions (1992), Oceanic crustal thickness from seismic measurements and rare earth element inversions, *Journal of Geophysical Research: Solid Earth*, *97*(B13), 19,683–19,715.

White, R. S., T. A. Minshull, M. J. Bickle, and C. J. Robinson (2001), Melt generation at very slow-spreading oceanic ridges: Constraints from geochemical and geophysical data, *Journal of Petrology*, *42*(6), 1171–1196.

Wilson, C. R., M. Spiegelman, and P. E. van Keken (2017), TerraFERMA: The

Transparent Finite Element Rapid Model Assembler for multiphysics problems in Earth sciences, *Geochemistry Geophysics Geosystems*, *18*(2), 769–810.

Zhu, W., C. David, and T.-f. Wong (1995), Network modeling of permeability evolution during cementation and hot isostatic pressing, *Journal of Geophysical Research: Solid Earth*, *100*(B8), 15,451–15,464.

# Chapter 4

# Large scale organization of multiple melt focusing mechanisms in two-phase flow models of mid-ocean ridges

## 4.1 Abstract

Magmatism at mid-ocean ridges generates new oceanic crust and accounts for 90% of global volcanism. The oceanic crust is emplaced in a narrow neo-volcanic region (e.g. *Macdonald* (1982); *Carbotte et al.* (2016)), whereas basaltic melt is generated in a wide region beneath mid-ocean ridges as suggested by a few geophysical surveys (*Forsyth et al.*, 1998a; *Key et al.*, 2013). A number of focusing mechanisms have been proposed such as ridge suction and decompaction layers (*Spiegelman and McKenzie*, 1987; *Sparks and Parmentier*, 1991; *Keller et al.*, 2017). I present results from a suite of two-phase models applied to the mid-ocean ridges using M3LT (Chapter 3), varying half spreading rate. The amount of oceanic crust versus half spreading rate generated by our models are within observations from active seismic surveys (*White et al.*, 1992; *Bown and White*, 1994; *White et al.*, 2001; *Harding et al.*, 2017). The models suggest that the suppression of porosity waves contributes to the decrease of oceanic crustal thickness variations with increasing spreading rate. I analyze how the melt focusing mechanisms present in our models (ridge suction from incompressible shear, decompaction layers and the recently discovered melting rate focusing) varies with spreading rate. Analyses suggest that melting

rate focusing decreases slightly with spreading rate whereas melt focusing from decompaction layers increases rapidly below half spreading rate of 4 cm/yr and then decreases beyond that. Melting rate focusing is persistent regardless of spreading rate and it focuses a higher proportion of melt produced at slower spreading rates.

## 4.2 Introduction

Mid-ocean ridges are a prominent feature of plate tectonics that run for more than 60,000 km along the major ocean basins. Tectonic forces pull the oceanic plates apart at these ridges, causing mantle upwelling and generating melt due to decompressional melting. New oceanic crust is created in a narrow neovolcanic region, accounting for 90% of global magmatism (*Macdonald*, 1982; *Vera et al.*, 1990; *Carbotte et al.*, 2016). Geophysical observations at specific locations suggest that there are wide regions of partially molten mantle at depth (*Bown and White*, 1994; *Forsyth et al.*, 1998a,b; *Key et al.*, 2013). These observations suggest that melt that forms oceanic crust has to be focused onto a narrow region at the ridge axis. The generation and segregation of melt in the mantle is obscured since the partially molten zone is not directly accessible. Geochemical and geophysical observations require significant efforts due to the difficulties accompanying the underwater nature of the mid-ocean ridges. Therefore, it is useful to complement our understanding of these systems by using theoretical models (*Spiegelman and McKenzie*, 1987; *Morgan*, 1987; **?**)).

In this study, I build on a new open-source two-phase flow model: Melt in the Mantle beneath Mid-ocean ridges model, or M3LT (Chapter 3). M3LT is based on TerraFERMA, the Transparent Finite Element Rapid Model Assembler (*Wilson et al.*, 2017), and solves the two-phase flow equations that were derived independently by a few workers (*McKenzie*, 1984; *Fowler*, 1985; *Scott and Stevenson*, 1986). I use M3LT to explore how the spreading rate changes the dynamics of the two-phase system. Varying the spreading rates in M3LT requires changing a few parameters and initial conditions to ensure numerical stability. I describe the changes in detail and provide the models in the form of TerraFERMA mark up language files (.tfml) to ensure reproducibility.

Theoretical models have to be validated by real world observations before further interpretations can be made. Active source seismic studies suggest that melt segregates from the mantle to form an average oceanic crustal thickness of about $6-7$ km (*White et al.*, 1992; *Bown and White*, 1994; *White et al.*, 2001; *Harding et al.*, 2017), which is a first order observation at mid-ocean ridges. Our models generate oceanic crust that has a thickness within these observations. Additionally, our models suggest that the suppression of waves carrying melt contributes to the decrease in variability of oceanic crustal thickness as spreading rate increases.

Focusing mechanisms are needed to explain how melt generated in a wide region is funneled to a narrow region of magmatism at the mid-ocean ridge. Several focusing mechanisms have been proposed. One of the earliest proposed mechanisms is 'ridge suction', in which flow is driven by a negative dynamic pressure arising from incompressible shear, and pulls melt towards the ridge axis from the surrounding region (*Spiegelman and McKenzie*, 1987; *Morgan*, 1987). Another proposed focusing mechanism is that caused by anisotropic permeability generated by dike propagation (*Morgan*, 1987). A similar proposed mechanism is the formation of shear driven melt bands from localization instabilities that align melt bands in accordance to shear direction (*Holtzman et al.*, 2003a,b; *Kohlstedt and Holtzman*, 2009). Another commonly invoked melt focusing mechanism is that of decompaction layers at the base of the lithosphere (*Sparks and Parmentier*, 1991; *Spiegelman*, 1993a; *Hebert and Montési*, 2010; *Keller et al.*, 2017). Buoyant melt is generated in a wide melting region and travels upwards until it encounters an impermeable barrier formed by the thermal boundary layer of the cold and stronger lithosphere. Melt is then deflected along this melt rich "decompaction layer" towards the ridge axis. Channelization is yet another melt focusing mechanism, in which reactive infiltration instabilities create melt channels that coalesce into larger channels as a way of focusing melt (*Aharonov et al.*, 1995; *Spiegelman et al.*, 2001). Finally, it is possible for the spatial gradient in melting rate to allow a negative compaction pressure to draw melt into the region with the highest melting rate (axial) as recently observed by *Turner et al.* (2017) and also observed and named melting rate focusing in Chapter 3. The models we discuss in this chap-

ter demonstrate a few of the mechanisms described above, namely ridge suction, decompaction layers and the melting rate focusing.

## 4.3 Method

### 4.3.1 Two-phase flow

The governing equations for a Darcy-like percolative fluid melt flow through a viscously deforming compactible solid mantle matrix were derived by three independent groups (*McKenzie*, 1984; *Scott and Stevenson*, 1984, 1986; *Fowler*, 1985). The set of governing equations follows Chapter 3 (equations 3.12-3.16):

$$\nabla \cdot 2\eta\dot{\epsilon}_d - \nabla p^* + \Delta\rho\phi\mathbf{g} = 0 \tag{4.1}$$

$$\mathcal{P} = \zeta\nabla \cdot \mathbf{v_s} \tag{4.2}$$

$$\frac{D\phi}{Dt} + (1-\phi)\frac{\mathcal{P}}{\zeta} = -\frac{\Gamma}{\rho_s} \tag{4.3}$$

$$\frac{\mathcal{P}}{\zeta} - \nabla \cdot \frac{K}{\mu}(\nabla\mathcal{P} + \nabla p^* + \Delta\rho\mathbf{g}) = \frac{\Delta\rho}{\rho_f\rho_s}\Gamma \tag{4.4}$$

$$\rho_f c_p^f \phi\frac{D_f T}{Dt} + \rho_s c_p^s(1-\phi)\frac{D_s T}{Dt} - \phi\alpha_f T\frac{D_f P}{Dt} - (1-\phi)\alpha_s T\frac{D_s P}{Dt} + T\Delta S\Gamma - \nabla \cdot k\nabla T = 0 \tag{4.5}$$

where $\eta$ is the solid shear viscosity, $\dot{\epsilon}_d$ is the deviatoric strain rate, $\mathbf{v_s}$ is the solid mantle velocity, $p^*$ is the dynamic pressure, $\Delta\rho = \rho_s - \rho_f$ is the difference between solid and fluid densities, $\rho_s$ and $\rho_f$ are the solid mantle and fluid densities respectively, $\phi$ is the porosity, $\mathbf{g}$ is the gravitational acceleration, $\mathcal{P}$ is the compaction pressure, $\zeta$ is the bulk viscosity, $t$ is time, $\Gamma$ is the total melting rate, $K$ is the permeability, $\mu$ is the viscosity of the fluid melt, $c_p^f$ is the heat capacity of the fluid melt at constant pressure, $T$ is the temperature, $c_p^s$ is the heat capacity of the solid mantle, $\alpha_s$ is the thermal expansion coefficient, $P$ is the thermodynamic pressure, $\Delta S = s_s - s_f$ is the change in entropy of melting, $k$ is the thermal conductivity and $\cdot_s$ and $\cdot_f$ are subscripts for solid and fluid. The symbols and their definitions are given in Table 3.1.

In the above formulation, the total pressure, $P$, has been decomposed into compaction pressure, $\mathcal{P}$ (defined in Equation 4.2), dynamic pressure, $p^*$, and lithostatic pressure, $P_L$ (Equation 3.9). The constitutive relationships for solid shear and bulk viscosities, permeability and interphase exchanges are discussed in Chapter 3.

### 4.3.2 Non-dimensionalization

Following Chapter 3, we substitute the non-dimensional scalings into equations 4.1-4.5 and drop the primes:

$$\frac{\delta_0^2}{h^2}\nabla \cdot 2\eta\dot{\epsilon}_d - \nabla p^* + \phi_0\phi\hat{\mathbf{k}} = 0 \tag{4.6}$$

$$\phi_0\frac{\mathcal{P}}{\zeta} = \frac{\delta_0^2}{h^2}\nabla \cdot \mathbf{v_s} \tag{4.7}$$

$$\frac{\partial\phi}{\partial t} + \mathbf{v_s}\cdot\nabla\phi + (1-\phi_0\phi)\frac{h^2}{\delta_0^2}\frac{\mathcal{P}}{\zeta} = -\Gamma \tag{4.8}$$

$$\frac{h^2}{\delta_0^2}\frac{\mathcal{P}}{\zeta} - \nabla\cdot\frac{K}{\mu}[\nabla(\mathcal{P}+p^*) + \hat{\mathbf{k}}] = \frac{\Delta\rho}{\rho_f\rho_s}\Gamma \tag{4.9}$$

$$\begin{aligned}(\frac{\rho_f}{\rho_s}\phi_0\phi + (1-\phi_0\phi))\frac{\partial T}{\partial t} + \frac{\rho_f}{\rho_s}\phi_0\phi\mathbf{v_f}\cdot\nabla T + (1-\phi_0\phi)\mathbf{v_s}\cdot\nabla T - \\ (1-\phi_0\phi)\frac{\alpha_s g h}{c_p}T\mathbf{v_s}\cdot\hat{\mathbf{k}} + \phi_0\frac{L_0}{c_pT_1}L\Gamma - \frac{1}{Pe}\nabla^2 T = 0\end{aligned} \tag{4.10}$$

where $\delta_0$ is the compaction length scale (Equation 3.42) and $Pe$ is the Peclet number (Equation 3.43) as defined in chapter 3.

We use results from one dimensional studies of the porosity structure in an upwelling mantle (e.g. *Ribe* (1987); *Spiegelman and Elliott* (1993)) to build intuition on how changing half spreading rate, $U_0$, might change these non-dimensional numbers. Conservation of mass for a one-dimensional upwelling, adiabatically melting mantle column shows that $\rho_f\phi_0 w_0 = \rho_s W_0 F_{max}$ for no melt separation, where $F_{max}$ is the maximum degree of melting and upwelling rate, $W_0$, can be approximated by $U_0$. Melt flux, $\phi_0 w_0$, is defined by the percolative melt flux in the Darcy-like equation:

$$\phi_0 w_0 = \frac{K_0\phi_0^n\Delta\rho g}{\mu} \tag{4.11}$$

**Table 4.1**: Scaling for non-dimensional quantities for varying half spreading rates

| Model | U1 | U2 | U4 | U8 |
|---|---|---|---|---|
| $U_0$ (cm/yr) | 1 | 2 | 4 | 8 |
| $\phi_0$ (%) | 0.195 | 0.276 | 0.390 | 0.551 |
| $w_0$ (cm/yr) | 120.8 | 170.8 | 241.6 | 341.7 |
| $t$ (kyrs) | 82.8 | 58.6 | 41.4 | 29.3 |
| $\delta_0$ (km) | 8.83 | 10.5 | 12.5 | 14.8 |
| $\left(\frac{h}{\delta_0}\right)^2$ | 128.2 | 90.6 | 64.1 | 45.4 |
| $Pe$ | 5264 | 7052 | 9974 | 14105 |

With these two equations for melt flux, we estimate the reference porosity, $\phi_0$, melt flow velocity, $w_0$, time, $t$, compaction length scale, $\delta_0$, and the Peclet number, $Pe$, for varying half spreading rate, $U_0$ (Table 4.1).

The reference porosity is fairly small, less than a percent regardless of spreading rate. The reference fluid velocity, $w_0$, is much faster than the half spreading rate, $U_0$, by about two orders of magnitude. As we increase half spreading rate, we increase both $\delta_0$ and $Pe$. Increasing half spreading rate will lead to an increase in upwelling rate and thus increasing the advection of heat. The reference compaction length scale, $\delta_0$, depends on both the solid and fluid material properties. As the solid remains largely unchanged, $\delta_0$ depends mostly on the reference porosity, $\phi_0$.

For the models presented here, we make the same small porosity approximation (Chapter 3), decoupling the equations such that the solid flow no longer depends on the fluid flow and solve for the solid system and the fluid system separately.

### 4.3.3 Numerical implementations

We explore the two-phase dynamics for mid-ocean ridges with varying half spreading rates $U_0 = 1, 2, 4, 8$ cm/yr. Ultra slow, slow, intermediate and fast spreading are defined by full spreading rates as $< 1.2 - 2$ cm/yr, $< 5.5$ cm/yr, $5.5 - 7$ cm/yr and more than 7 cm/yr respectively (e.g.*Dick et al.* (2003)). These definitions can vary. The models presented in this chapter are based on the example model presented in Chapter 3 and any changes are described here.

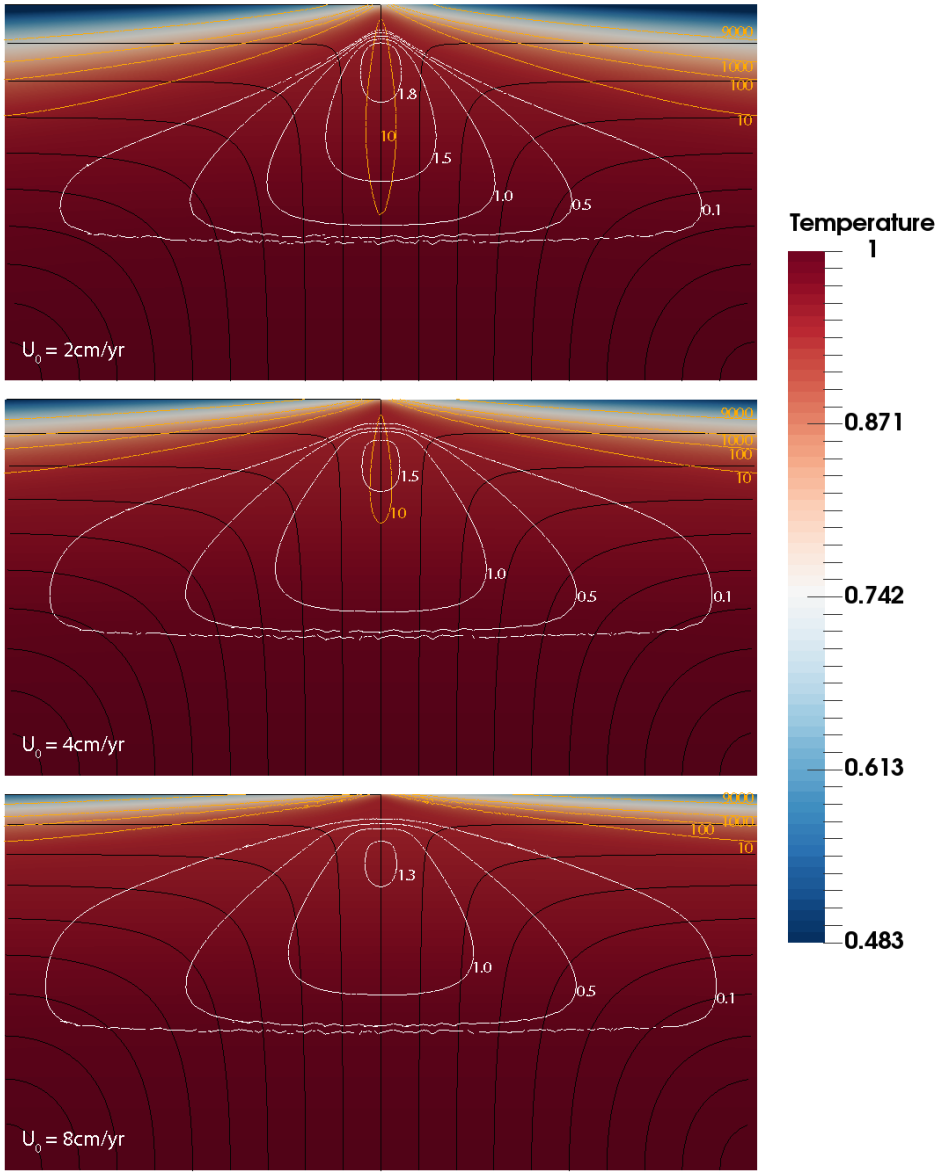


**Figure 4.1**: The converged temperature solutions from the solid system for models $U2$, $U4$ and $U8$. The domain is 100 km deep and 200 km wide. Black lines are solid flow lines. White labeled contours are non-dimensional total melting rate, $\Gamma$. Orange labeled contours are non-dimensional viscosity contours scaled by $\eta_0 = 10^{19}$ Pa s. We show models of increasing half spreading rate going down the panels. The melting rate is higher for smaller $U_0$ (higher degree melting for smaller $U_0$).

**Table 4.2**: Initial porosity pipe parameters, $\nabla p^*$ and freezing rate constant, $R$, choices for varying half spreading rates.

| Model | U1 | U2 | U4 | U8 |
|---|---|---|---|---|
| $U_0$ (cm/yr) | 1 | 2 | 4 | 8 |
| $x_{pipe}$ | 0.01 (1 km) | 0.005 (500 m) | 0.001 (100 m) | 0.005 (500 m) |
| $y_{pipe}$ | 0.1 (10 km) | 0.05 (5 km) | 0.05 (5 km) | 0.1 (10 km) |
| $m_p$ | 5 | 5 | 100 | 100 |
| $\nabla p^*$ | no | no | yes | yes |
| $R$ | 50 | 100 | 200 | 400 |

Each model with varying $U_0$ has a corresponding solid Stokes system solution for variables $p^*$, $\mathbf{v_s}$ and $T$. The temperature solution for the solid system for each model is used as the initial condition for the two-phase system (Figure 4.1). Both the temperature and orange viscosity contours show that the thickness of the lithosphere increases away from the ridge axis for all the models. The lithospheric thickness decreases with increasing half spreading rate, $U_0$, at the same distance away from the ridge axis. All the models show that the white contours for total melting rate, $\Gamma$, are roughly triangular in shape. The maximum total melting rate, $\Gamma$, decreases in magnitude with increasing half spreading rate, $U_0$. We dedicate a section later on for model $U1$ with the slowest spreading rate, $U_0 = 1$ cm/yr due to its uniqueness.

In conjunction with varying $U_0$, the initial porosity pipe and freezing rate constant, $R$, are adjusted accordingly for each model. The initial porosity pipe is described in detail in Chapter 3. The models presented here all have different initial porosity pipes (Figure 4.2) with the exact dimensions described in Table 4.2. Model $U4$ is exactly the same as the example model described in Chapter 3. We test a range of the initial porosity pipes for each model and use the smallest one that allows melt to leave the top boundary such that the numerical models will work.

As discussed in chapter 3, freezing rate $R$ is proportional to $\frac{\phi_0 w_0}{h}$ with units of per unit time, $s^{-1}$, from $\Gamma$ scaling and the freezing rate equation (Equation 3.28). A 1-D melting column approximation for freezing rate, $R$, should then scale linearly with half spreading rate, $U_0$ (Table 4.2). Other boundary and initial conditions

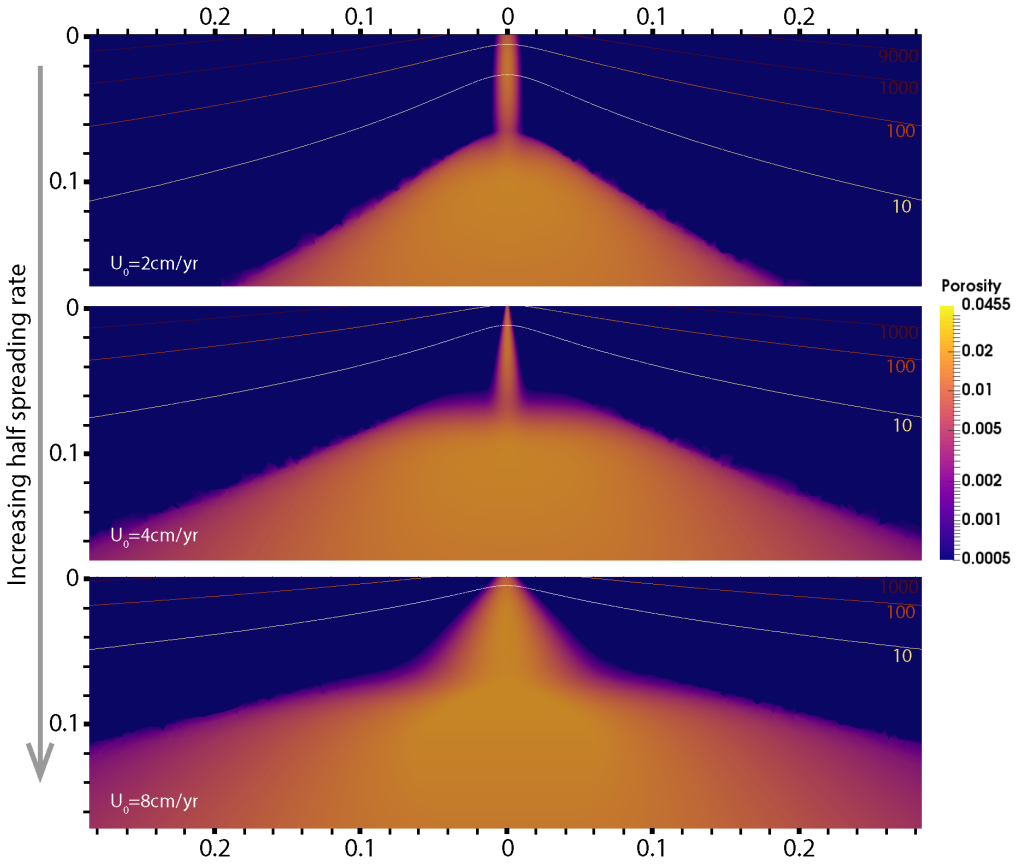


**Figure 4.2**: Close up view centered at the ridge axis to show the porosity initial conditions for models $U2$, $U4$ and $U8$. The width and depth of the panels are about 56 km and 18 km respectively. The top panel shows $U2$ while the bottom one shows $U8$. The initial porosity condition shows a pipe-like structure beneath the ridge axis and porosity in the the melting region approximated by the melting rate in the solid Stokes system. The initial porosity pipe facilitates melt out of the top boundary and has varying shapes depending on the spreading rates (dimensions are given in Table 4.2).

along with the mesh, numerical methods and solvers used are discussed in detail in chapter 3. The parameters and the values used are given in Table 3.2.

## 4.4 Results

### 4.4.1 Models $U2$, $U4$ and $U8$

All the models go through an initial transient period before reaching a quasi steady state. A detailed time-evolution of Model $U4$ is described in Chapter 3. All models run for the minimum time needed for a parcel of material to travel from the bottom of the domain and exit out the side boundaries or $t \sim 2h/U_0$, a duration which varies with the half spreading rate. The maximum run time is limited by computational resources. Each model has a different end time in Myrs as the scaling for time changes with half spreading rate (Table 4.1). We compare snapshots of our model results taken at $\sim$8 Myrs, which is near the end of the shortest model run in Myrs ($U8$).

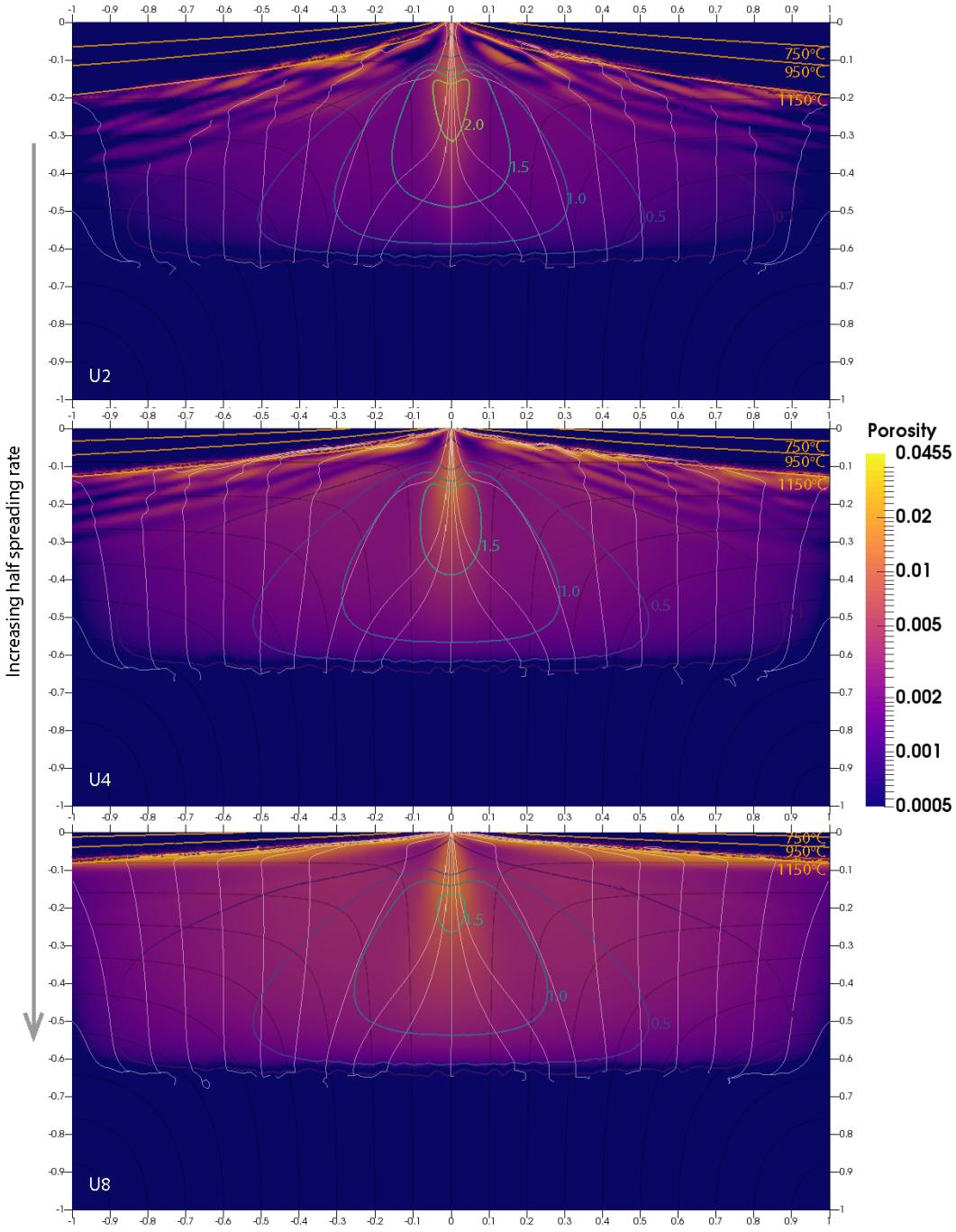


**Figure 4.3**: Snapshots of the porosity field for models, $U2$, $U4$ and $U8$ taken at 8.5 Myrs. The domain is 200 km wide and 100 km deep. Non-dimensional total melting rate, $\Gamma$, contours are in lime green to dark violet.

Figure 4.3 (continued): $\Gamma$ contours are roughly triangular in shape. The maximum melting rate is higher for smaller $U_0$. Orange contours are for temperature (labeled in degree Celsius). Solid flow lines are in black. Melt flux flow lines are in white. These flow lines show melt moving towards the ridge axis deep in the melting region regardless of spreading rates. They bunch up where melting rate is the highest. There are two regions of higher porosity, at the center and on the sides.

The temperature is different between the solid system and the two phase system at the ridge axis, where it is warmer in the fluid flow models. $\Gamma$ contours show that the main structure of the melting region has not changed significantly from the solid Stokes solution except on the ridge axis (Figures 4.1 and 4.3).

The porosity structure changes for each model of a different spreading rate (Figure 4.3). One of the similarities in all the models is that the higher melting regions are in the center of the domain beneath the ridge axis and in the decompaction layers on both sides. Both model $U2$ and $U4$ have roughly triangular porosity structures that lie in the melting region. There are transient porosity waves above the sloped sides of the melting region traveling upwards towards the thermal boundary layer where freezing begins as melt encounters the cold and stronger lithosphere. These porosity waves are melt rich pockets that form due to the viscous resistance to compaction/decompaction of the solid matrix. There are less transient porosity waves in model $U4$ compared to model $U2$.

The interaction with the thermal boundary layer has been described as "decompaction melt layers" (e.g *Sparks and Parmentier* (1991); *Spiegelman* (1993a)). The decompaction layer is a melt rich layer that deflects melt from the cold strong lithosphere and focuses it towards the ridge axis. In model $U2$, the decompaction layer is not uniform or constant or continuous but changes with time as the time dependent porosity waves comes from below. The decompaction layer in model U4 is more continuous in space than that observed in model U2. Model $U8$ shows a more constant porosity structure with no porosity waves between the melting region and decompaction layers like in models $U2$ and $U4$. The decompaction layer here is uniform, constant and continuous compared with the models with lower spreading rates.

The snapshots of the models in Figure 4.3 show two sets of melt flux flow lines. The first set shows melt pulled towards the ridge axis deep in melting region. The flow lines gather together in the region of highest melting rate. They bunch up tighter for smaller half spreading rate, where the maximum $\Gamma$ is higher. The second set of flow lines follows melt produced on the sides of the melting region, buoyantly rising before encountering the thermal boundary layer, where melt is focused by the decompaction melt layers. The melt flux flow lines in model $U8$ show that the flow lines bend more to the sides the further away it is from the ridge axis.

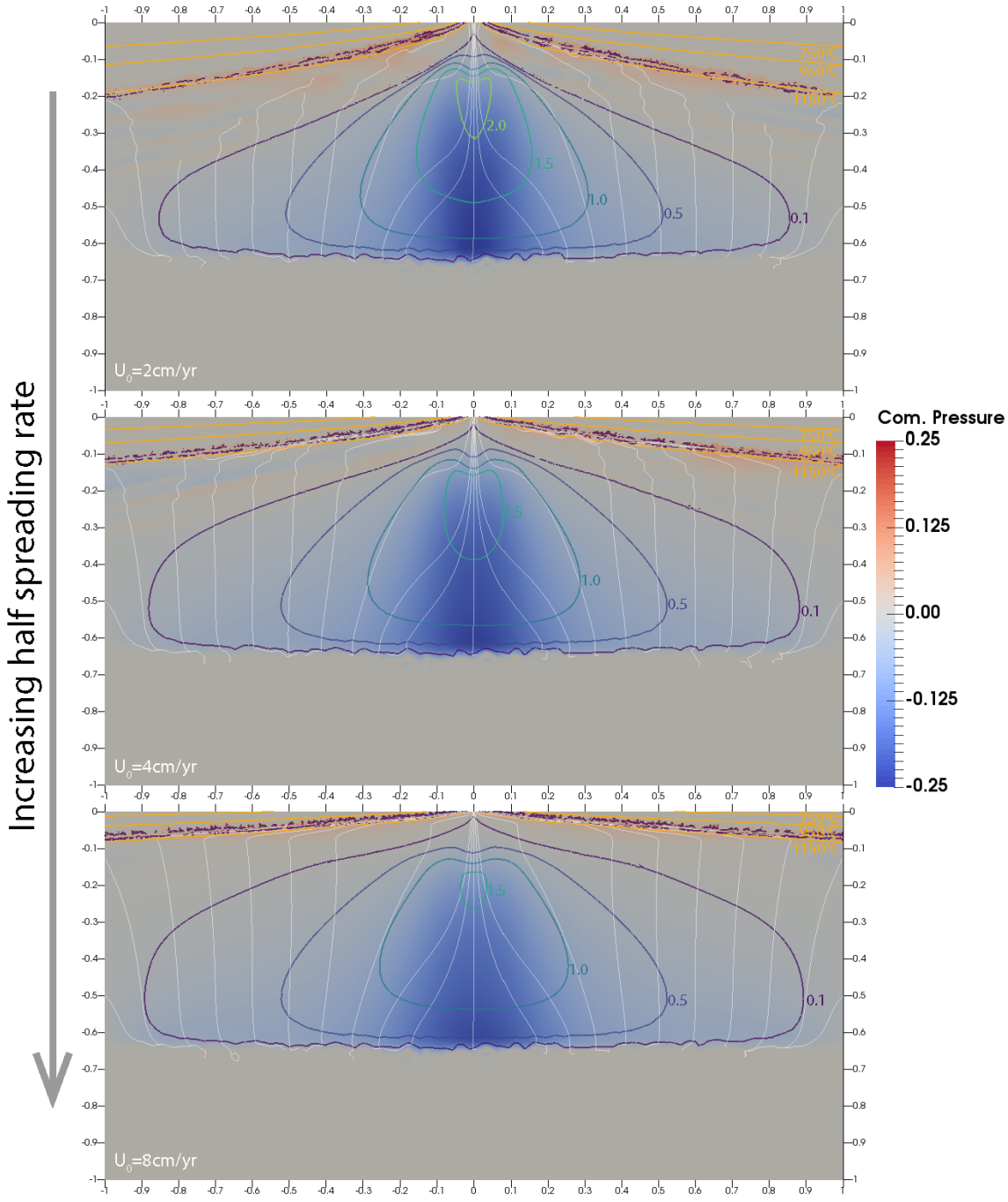


**Figure 4.4**: Snapshots of non-dimensional compaction pressure for models $U2$, $U4$ and $U8$, at 8.5 Myrs along with orange temperature contours and white melt flux flow lines.

Figure 4.4 (continued): Non-dimensional total melting rate, $\Gamma$, contours are in lime green to dark violet. 0.1 non-dimensional pressure represents 50 MPa. Compaction pressure is negative in the melting region. The largest negative compaction pressure occurs where melting first begins when temperature crosses the peridotite solidus at depths on the ridge axis. The area ahead of the porosity waves in models $U2$ and $U4$ have positive compaction pressure, where the solid matrix is decompacting to allow melt in.

The compaction pressure is defined as the compaction and decompaction of the solid matrix as melt is generated and segregated (Equation 4.2). When compaction pressure is positive, the divergence of solid velocity is positive, i.e the solid matrix is expanding as melt comes in. Conversely, when compaction pressure is negative, the divergence of solid velocity is negative, i.e the solid matrix is contracting as melt leaves. The compaction pressure in models $U2$, $U4$ and $U8$ is negative in the melting region as melt is segregating from the melting region (Figure 4.4). The compaction pressure is positive on the front of porosity waves as the solid matrix expands to allow melt moving in. Compaction pressure is also positive in the decompaction layers in all three models as melt continuously moves into it. Compaction pressure is most negative at the base of the melting region on the ridge axis where the solid mantle starts melting. The negative compaction pressure is largest in magnitude for model $U2$.

We track clinopyroxene depletion in our models to have more realistic melting and have a sense of how much depletion the solid mantle experiences. All three models show a primarily one-dimensional structure with depletion increasing towards the surface (Figure 4.5). The amount of melting follows the solid flow lines closely, therefore producing the one-dimensional structure. The solid mantle experiences more melting as it upwells on the ridge axis, as evident from the melting rate contours which are highest on the ridge axis. Away from the ridge axis, the solid mantle experiences less melting before turning the corner. At the thermal boundary layer, melt freezes into the lithosphere and moves with the solid flow outwards, creating enrichment in the lithosphere (Figure 4.5). The porosity waves in the models with slower spreading rates create distinctive patterns of depletion in the lithosphere. These are dependent on the parameterization of freezing.

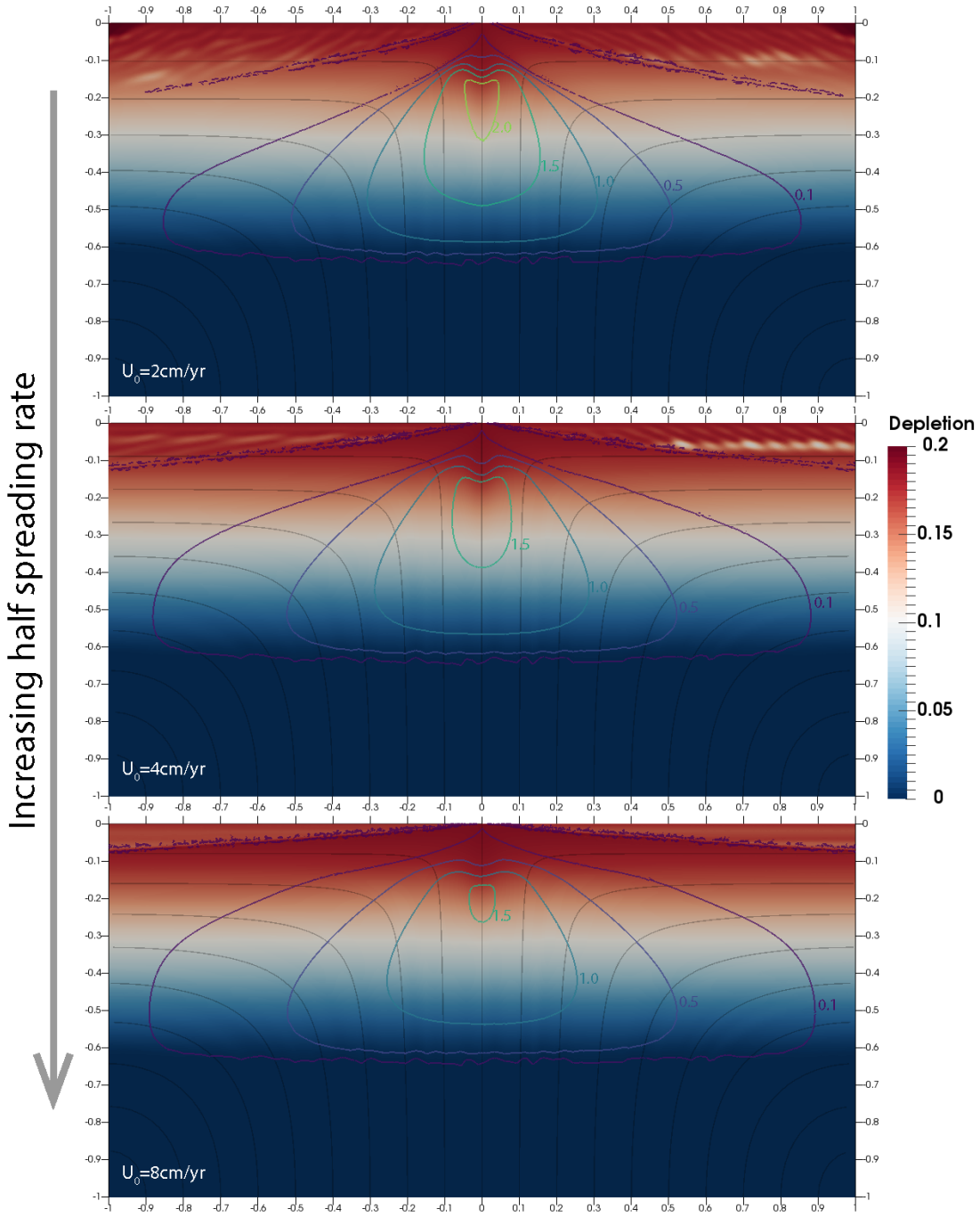


**Figure 4.5**: Snapshots of depletion, $F_d$, for models $U2$, $U4$ and $U8$, at 8.5 Myrs along with black solid flow lines. Non-dimensional total melting rate, $\Gamma$, contours are in lime green to dark violet. Depletion decreases with depth as the mantle upwells and melts. Above the decompaction layers, there are patterns of smaller depletion as melt freezes into the lithosphere.

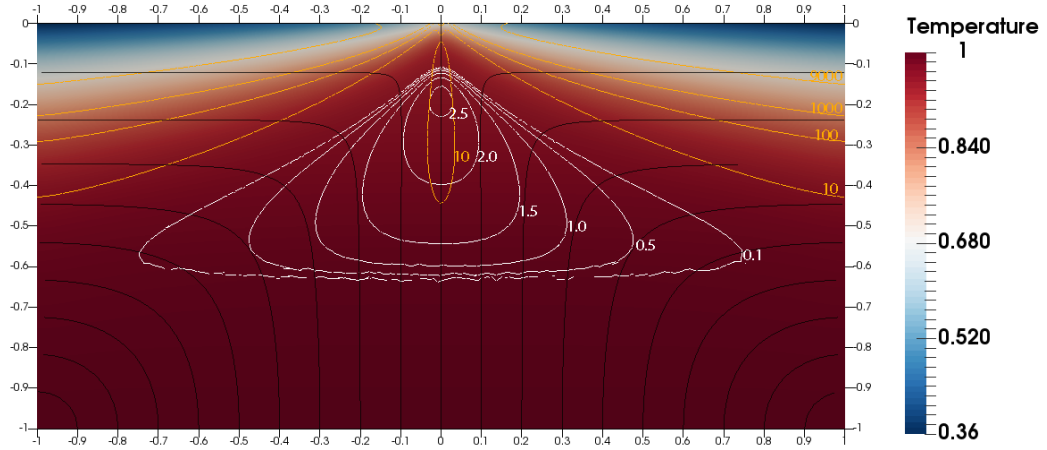


**Figure 4.6**: Temperature from solid system for model $U1$ with half spreading rate, $U_0 = 1$ cm/yr. The domain is 100 km deep and 200 km wide. Black lines are solid flow lines. White labeled contours are non-dimensional melting rate production, $\Gamma$. Orange labeled contours are non-dimensional viscosity contours scaled by $\eta_0 = 10^{19}$ Pa s.

### 4.4.2 Model $U1$

The model $U1$ with half spreading rate, $U_0 = 1$ cm/yr (characteristic to slow mid-ocean ridges), requires special treatment as a different set of numerical problems surfaces with a small spreading rate. Model $U1$ runs to maximum time of $\sim 90t$ ($\sim$7.5 Myrs). The solid system solution for model U1 is shown in Figure 4.6. The temperature field shows a thicker lithosphere compared to models with faster spreading rates. The melting region is triangular in shape. Similar to other models, model U1 requires a certain initial porosity pipe (Figure 4.7), the dimensions of which are given in Table 4.2.

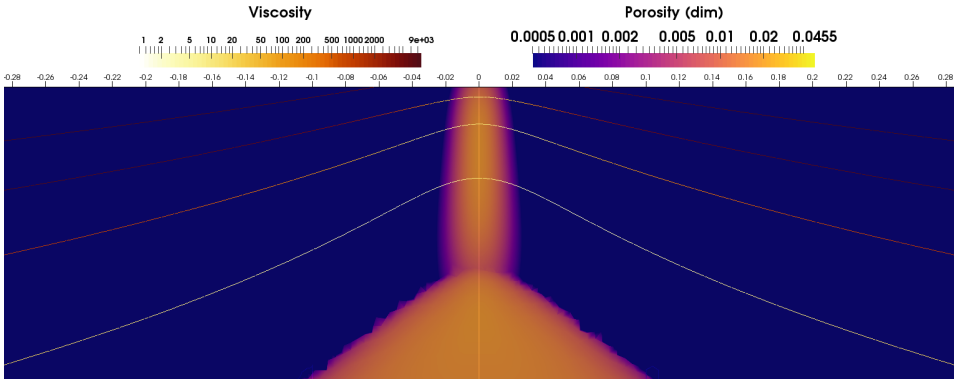


**Figure 4.7**: Close up view centered at the ridge axis to show the initial porosity pipe for model $U1$. The domain is 56 km wide and 18 km deep. The dimensions of the initial porosity pipe are given in Table 4.2.

Similar to the other models, the porosity structure in Figure 4.8a shows that the largest amount of melt occurs in the melting region and in the porosity waves above the melting region, similar to models $U2$ and $U4$. The porosity structure is shifted upwards from the base of the melting region as melt segregates much faster than the solid mantle is moving. Similar to models with faster spreading rate, melt is pulled towards the ridge axis deep in the melting region. The melt flow lines also gather towards the ridge axis at the depth where the melting rate is the greatest. Melt then moves upwards on the ridge axis and eventually out of the top of the domain. The sub-axial melting rate is larger in model $U1$ than in other models.

Unlike the other models, melt in model $U1$ pools beneath the thermal boundary layer on both sides (15 km depth and ∼15-40 km away from the ridge axis) before reaching the ridge axis. The porosities in these melt pools reach as high as ∼60%. As melt leaves the melting region and travels upwards away from the ridge axis, it forms porosity waves as observed in models $U2$ and $U4$. In models $U2$ and $U4$, the melt is then focused to the ridge axis by decompaction melt layer but in model $U1$, the melt never reaches the ridge axis. In model $U1$, all the melt pools and freezes into the colder and stronger lithosphere generating regions of enrichment within the mostly depleted asthenosphere before reaching the ridge axis (Figure 4.8c).

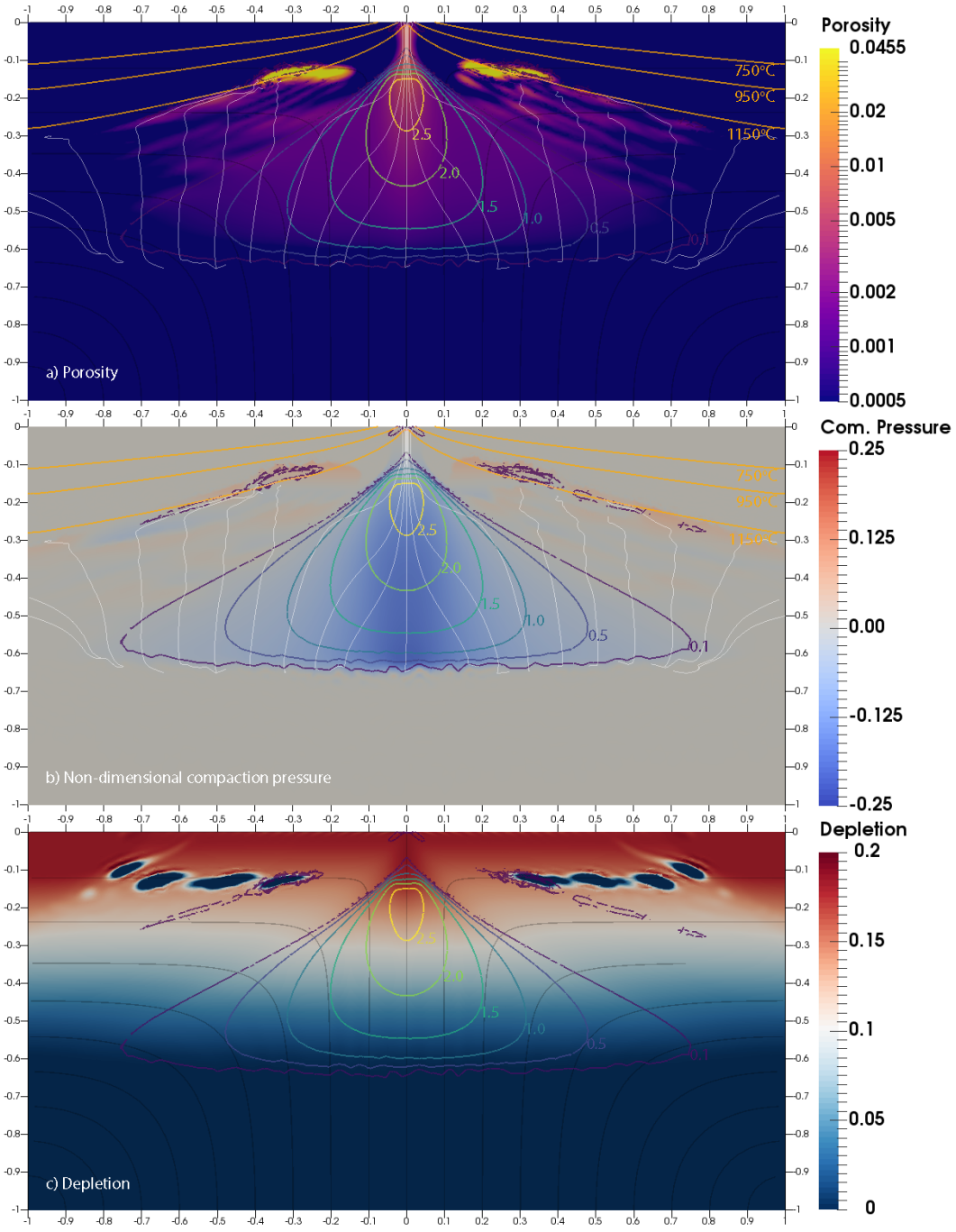


**Figure 4.8**: A snapshot of the a) porosity, b) non-dimensional compaction pressure and c) depletion for model $U1$ taken at the end of the model run at 7.5 Myrs. Contours of non-dimensional total melting rate $\Gamma$, are lime green to dark violet.

Figure 4.8 (continued): The melting region is triangular. Temperature contours are in orange. Solid flow lines are in black Melt flux flow lines are in white. Melt is pooling on both sides beneath the lithosphere in the thermal boundary layer. b) 0.1 of non-dimensional pressure here represents 50 MPa. Similar to the other models, there is a large negative compaction pressure at the base of the melting region on the ridge axis when melting first begins. The compaction pressure also shows where the porosity waves are moving. c) The depletion field shows blobs of enriched solid in the lithosphere.

Model $U1$ has similar compaction pressure structure as the other models, which are mostly negative in the melting region. There are larger positive compaction pressures where large amount of freezing is occurring. Like other models, the depletion field shows a one-dimensional structure, which increases as the solid mantle melts. There are also blobs of enriched solid in the lithosphere due to the high amount of freezing of the pools of trapped melt. The structure of this enrichment depends on the parameterization of freezing.

### 4.4.3 Pressure comparison

We compare the dynamic and compaction pressure on the ridge axis at 8.5 Myrs for models $U2$, $U4$ and $U8$ and at 7.5 Myrs for model $U1$ (Figure 4.9). The dynamic pressure is only significant near the ridge axis and is an order of magnitude smaller than the compaction pressure. On the other hand, the compaction pressure is significant in a much larger region where melting occurs. $\mathcal{P}$ is most negative where the solid mantle begins to melt at the dry peridotite solidus. The magnitude of $\mathcal{P}$ decreases with increasing half spreading rate except for model $U1$, which has the smallest $\mathcal{P}$ on the ridge axis.

Since compaction pressure is significant for most of the melting region, we show two depth profiles at 30 km and 60 km across the domain in Figure 4.10. The compaction pressure profiles for all the models are similar in that $\mathcal{P}$ is most negative on the ridge axis at 60 km, where the solid mantle is beginning to go through decompression melting. The profiles at 30 km depths is less negative but has a similar shape compared to the profiles at 60 km depths. All the profiles have similar shapes with steep gradients within 40 km of the ridge axis and gentler

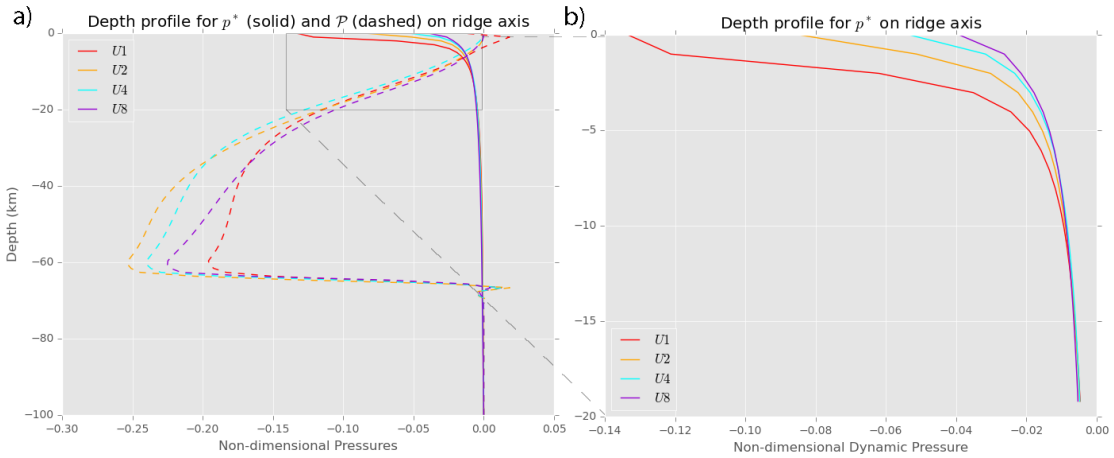


**Figure 4.9**: a) Snapshots of the depth profile of dynamic pressure, $p^*$ (solid), and compaction pressure, $\mathcal{P}$ (dashed), on the ridge axis for all models. The time taken at the snapshots correspond to the same time as in Figures 4.4 and 4.8b. The inset box show where the close up of $p^*$ is taken for b). Compaction pressure increases in magnitude with decreasing half spreading rate for $U_0 > 2$ cm/yr. Model $U1$ has the smallest compaction pressure on the ridge axis. b) Close up of depth profile of $p^*$ near the ridge axis. Dynamic pressure decreases in magnitude with increasing half spreading rate.

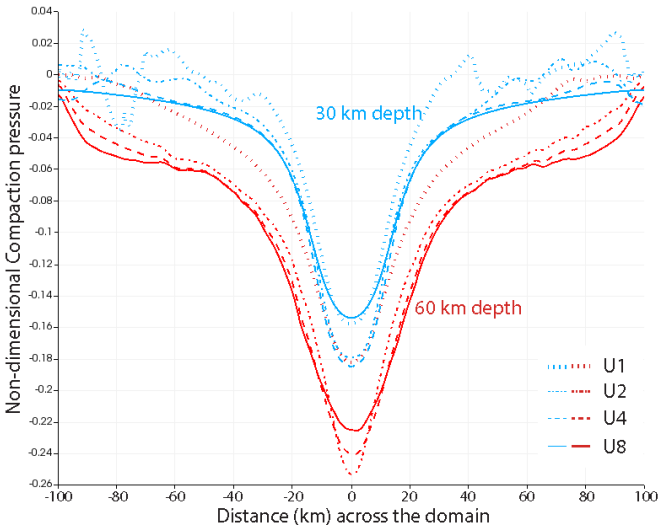


**Figure 4.10**: Profile of compaction pressure, $\mathcal{P}$, across the domain at 30 km (blue) and 60 km (red) depths for all the models. This depth profile shows where $\mathcal{P}$ is most negative where the solid mantle begins to melt. The profile for models $U2$, $U4$ and $U8$ are similar except on the ridge axis where the magnitude differs. Model $U1$ is shifted upwards to be less negative compared to the other models but has a similar shape overall.

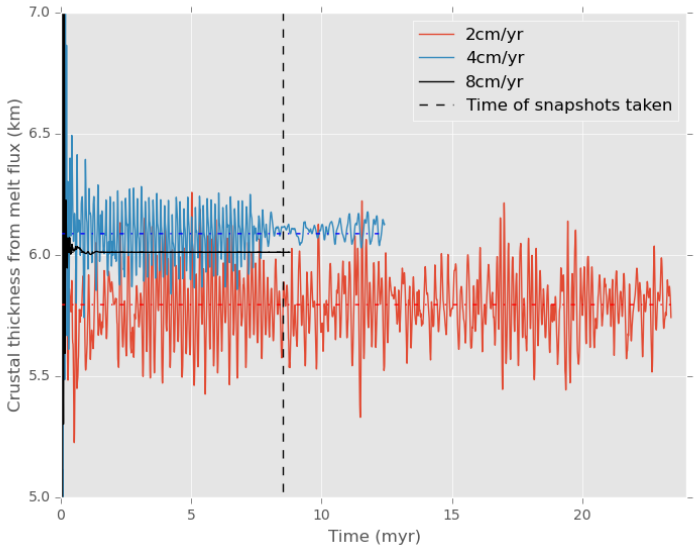


**Figure 4.11**: Oceanic crustal production (km) over time (Myrs) for models $U2$, $U4$ and $U8$ in red, blue and black respectively. Crustal thickness is calculated using the accumulated melt flux across the top boundary $\int \mathbf{q} ds_{top}$ assuming a oceanic crustal density of $\rho_c = 2800\,kg/m^3$. The black dashed line indicates 8.5 Myrs, where the snapshots are taken for Figures 4.3, 4.4 and 4.5. Each model extends to a different time because of the non-dimensional scaling (Table 4.1) and computational resources. There is a transient time at the beginning where the crustal production varies much more over a short period of time. The red and blue dashed lines are the averages for models $U2$ and $U4$. The crustal thickness goes into a steady state ~6 km for model $U8$. For the lower spreading rates, the crustal thickness predictions fluctuate around an average.

gradients beyond. The compaction pressure profile at 60 km for model $U1$ is shifted upwards compared to models $U2$, $U4$ and $U8$, which only differ slightly at the ridge axis.

### 4.4.4 Crustal production versus spreading rate

One of the seismically observable features of mid-ocean ridges is the amount of oceanic crust as a function of spreading rate (*White et al.*, 2001; *Harding et al.*, 2017). We predict the oceanic crustal thicknesses from models $U2$, $U4$ and $U8$ (Figure 4.11). The prediction from model $U1$ is not on the same plot as it fluctuates more and has a wider range that will obscure the predictions from the other models.

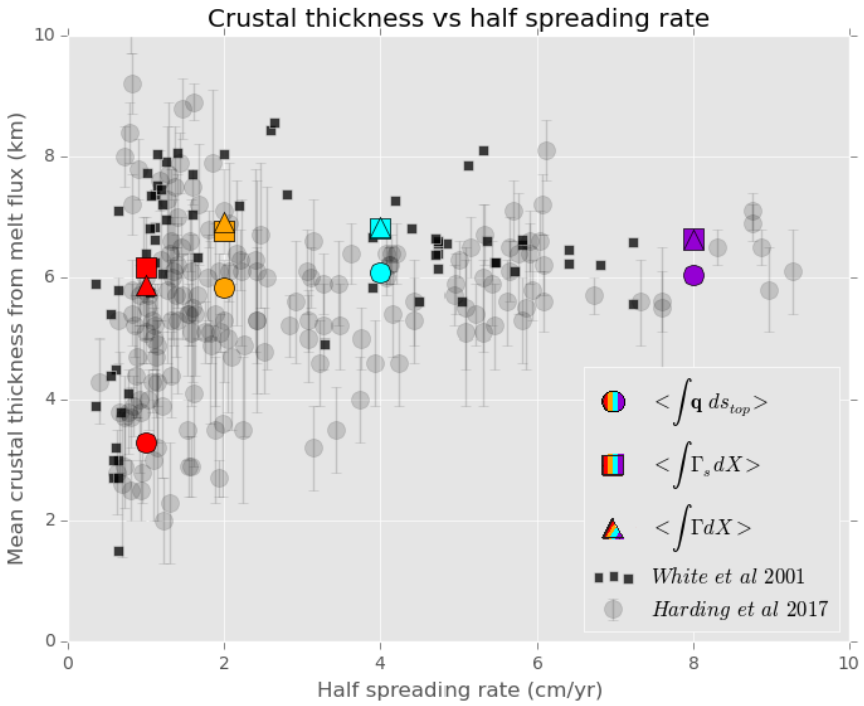


**Figure 4.12**: A plot of mean crustal thickness production versus half spreading rate, $U_0$, for our model predictions and geophysical observations. Colored circles are mean crustal thickness calculated from total melt flux coming out of the top boundary for the two-phase solve as shown in Figure 4.11. Colored squares and triangles are calculated from total melt production from solid system and fluid system respectively. The solid Stokes system represents passively driven single phase flow with thermal feedback. Red, orange, cyan and dark violet colors represent models $U1$, $U2$, $U4$ and $U8$ respectively. Black squares are from an active seismic data compilation (*White et al.*, 2001). Open circles are from a more recent compilation of active seismic data along with error bars (*Harding et al.*, 2017).

To calculate the oceanic crustal thickness from our models, we use the integral amount of melt flux that leaves the top boundary, i.e $\int \mathbf{q}\, ds_{top}$, and assume an oceanic crustal density of $\rho_c = 2800$ kg/m$^3$. With the melt density and half spreading rate, we can obtain the expected oceanic crustal thickness.

All the models go through a transient period of time at the beginning, when the estimates of crustal thickness fluctuate more. The model predictions then settle into quasi steady states, fluctuating about a mean, which is shown in Figure 4.12 as colored circles. The time series of predicted crustal thickness for model $U8$ has no fluctuations after the transient period compared to models $U2$ and $U4$. The prediction from model $U2$ has the most persistent fluctuations, which look like a combination of both high and low frequency waves. Model $U4$ also shows fluctuations in the prediction, which dampens after 7.5 Myrs and picks up after 10 Myrs with a different frequency.

To establish the relationship between spreading rate and oceanic crustal production, the mean crustal thickness from our model predictions is plotted against the half spreading rate for all the models in Figure 4.12. The colored squares and triangles show the predicted oceanic crustal thickness calculated from the total melt production from the two-phase flow and the solid Stokes flow respectively. Both the predictions calculated from the total melt production are close to each other since the total melting rate does not change significantly for a one way coupled model. The predicted oceanic crustal thicknesses calculated from the total melt production is the maximum possible from our models. The crustal thickness predictions from total melt flux are lower than that predicted from total melt production since some of the melt produced does not leave the domain to create oceanic crust but rather, freezes into the lithosphere. This difference in crustal thickness prediction between that calculated from the total melt flux and the total melt production shows that a greater amount of melt freezes into the lithosphere with slower spreading rates (*Cannat*, 1993).

Along with our model predictions in Figure 4.12, a compilation of observed oceanic crustal thicknesses versus half spreading rates from active seismic surveys is plotted in black squares (*White et al.*, 2001) along with a more recent compi-

lation plotted as open circles with error bars (*Harding et al.*, 2017). Our model predictions fit within the geophysical observations of oceanic crustal thicknesses versus half spreading rates. The older compilation of seismic data suggests that crustal thickness is about 7 km irrespective of half spreading rate for half spreading rate more than 1 cm/yr and rapidly decreases for slower spreading rates. The more recent compilation of *Harding et al.* (2017) gives an average oceanic crustal thickness of ∼6 km. The recent compilation also suggests that not only does the oceanic crustal thicknesses vary more than previously observed, this variability seems to decrease as spreading rates increase. The variability in predicted crustal thickness decreases with increasing spreading rate in our models (Figure 4.11), due to time dependent porosity waves. The porosity waves are more prominent at slower spreading rates (Figure 4.3). At slower spreading rates, porosity is wavy in the decompaction layer, which creates the fluctuating melt flux out of the top boundary at the ridge axis (Figure 4.3).

Our models suggest that the presence of porosity waves may contribute to the observed variability in crustal thickness at a given location. Other factors such as the mantle potential temperature would only change the average melt production for a region. For faster spreading rates, where porosity waves are suppressed, the variability in crustal thickness at different mid-ocean ridges might point to a change in mantle potential temperature or other regional factors. The characteristics of porosity waves depends on spreading rate. When melt flux varies at compaction length scales, viscous resistance to volumetric expansion or contraction is important, therefore creating dispersive porosity waves (*Spiegelman*, 1993b,c). At slower spreading rates, melt flux varies at the local compaction length scale, thus creating porosity waves. At faster spreading rates (such as in model $U8$), melt flux varies at a length scale larger than the local compaction length scale, therefore creating porosity waves as melt moves through the mantle matrix in the absence of significant viscous resistance. This is distinctly different than the fluctuations in crustal thickness reported by *Sotin and Parmentier* (1989) which were due to opposing compositional and thermal buoyancy.

## 4.5 Discussion

Model choices such as one-way coupling and parameterization of melting are discussed in Chapter 3. In our models, we explore how varying half spreading rate affects two-phase dynamics beneath mid-ocean ridges. In the model set up, varying half spreading rate requires that we vary the initial conditions (specifically the porosity pipe), freezing rate, $R$, and inclusion of $\nabla p^*$ in the Darcy's flow equation. The porosity pipe is needed to assist melt flow out of the domain to create crust. Without the porosity pipe, melt will pile up beneath the Moho at the ridge axis and create numerical problems. We test a range of shapes and sizes for the porosity pipes and used the smallest configuration that allows numerical stability.

In our model, we have parameterized freezing using an arbitrary freezing rate constant, $R$. If the models had no freezing, melt simply moves into the cold and thus stronger lithosphere. The cold strong lithosphere is viscously resistance to the compaction pressure that wants to move the melt out. As a parcel of melt moves into colder thus stronger lithosphere, compaction pressure builds up, which eventually leads to numerical failures. A better parameterization of freezing is beyond the scope of this study.

The inclusion of $\nabla p^*$ in equation 4.4 gives the ridge suction focusing mechanism. $\nabla p^*$ has been excluded from models $U1$ and $U2$ with lower half spreading rate because, as seen in Figure 4.9, the dynamic pressure becomes so strong in the small region around the ridge axis that the numerical solvers fail immediately. This might be resolved if the models were fully coupled since the dynamic pressure will adjust to a weaker ridge axis in the two phase system. An example of fully coupled ridge model with an isoviscous rheology is included in the primary TerraFERMA paper (*Wilson et al.*, 2017). More computational resources will be required to solve the Stokes problem at every time step.

Our models predict oceanic crustal productions that are within the observed oceanic crustal thicknesses from geophysical surveys (Figure 4.12). Changing the mantle potential temperature, interphase exchanges, melting/phase diagram, enrichment of mantle and volatiles will no doubt alter the predictions. Magnetotel-

luric (MT) imaging of mantle upwelling beneath the East Pacific Rise shows a conductive region 20-90 km beneath the ridge axis that is interpreted as partially molten mantle (*Key et al.*, 2013). Our models $U4$ and $U8$ with faster spreading rates show a higher porosity region around the same depths as that observed, although the observation of melt extends much deeper. Adding volatile-enhanced melting to our models would extend our melting region deeper.

### 4.5.1 Melt focusing

In our models, melt is produced in a wide melting region of more than 100 km and focused to the ridge axis to form oceanic crust. We illustrate the three distinct melt focusing mechanisms observed in our M3LT models and previous models, namely: melting rate suction, decompaction layers and ridge suction in Figure 4.13.

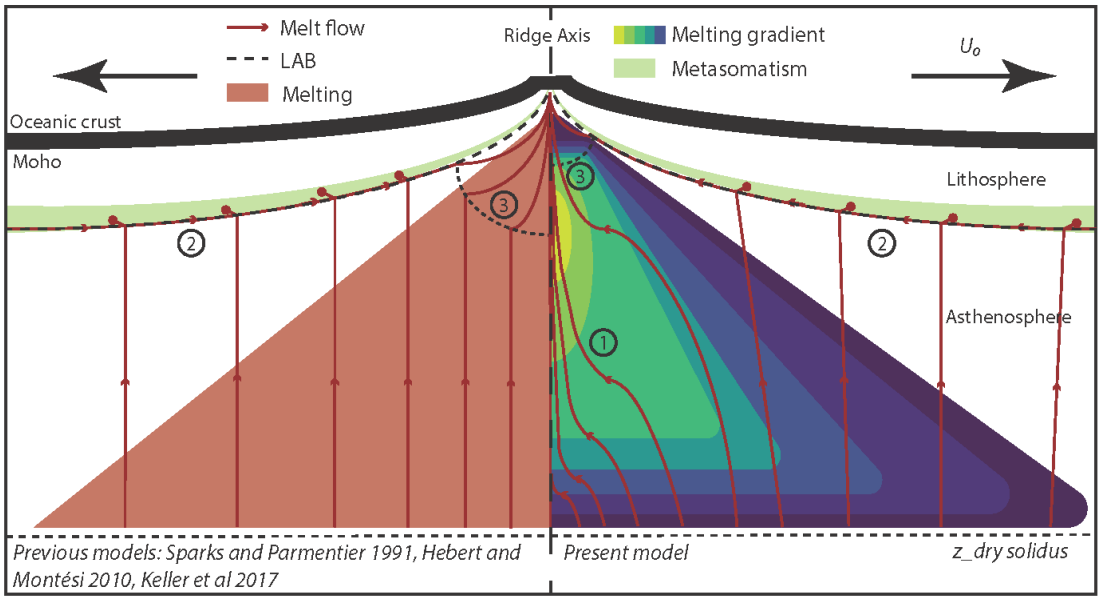


**Figure 4.13**: Illustration of melt focusing mechanisms from past and present work. The dashed black line down the center represents the ridge axis. The thick black curved lines that connect at the highest point at the ridge axis represent the oceanic crust. The Moho is the bottom of the oceanic crust. Melting is represented as the salmon pink triangle on the left for previous work while it is represented by a lime green to dark violet melting triangle on the right for our models. Red lines and arrows indicate melt flow and direction. Red circles indicate where melt freezes into the lithosphere in the green region of metasomatism above the black dashed line for the lithosphere-asthenosphere boundary (LAB). The three melt focusing mechanisms observed in our models are numbered on the right side, 1) Magmatic focusing 2) decompaction layers and 3) ridge suction. Melt generated deep in the melting region on the ridge axis is pulled towards the ridge axis due to compaction pressures from melting rate gradient. This effect is observed in a recent model (*Turner et al.*, 2017).

Figure 4.13 (continued): Both previously recognized decompaction layers and ridge suction effects are observed in our models as well. Decompaction layers (*Sparks and Parmentier*, 1991; *Hebert and Montési*, 2010; *Keller et al.*, 2017) are represented by the red lines and arrows on the LAB beneath the metasomatism region, moving melt towards the ridge axis As melt is generated in the melting region, it is buoyant and moves upwards. Melt then encounters the colder and thus stronger lithosphere. Some melt freezes into the lithosphere while the rest are deflected upwards along this thermal boundary layer towards the ridge axis, thus forming the decompaction layer. Ridge suction near the ridge axis is due to the incompressible shear as tectonic forces are pulling the oceanic plates apart (*Spiegelman and McKenzie*, 1987; *Keller et al.*, 2017). Melt suction at the ridge axis in our models is smaller than previous models as much of the melt is already focused deep in the melting region.

As discussed in chapter 3, other two phase flow models applied to mid-ocean ridges use the same governing equations but make various assumptions (e.g zero compaction length approximation, small porosity approximation like we used in our models). All the focusing mechanisms illustrated in Figure 4.13 exist in the models that include the pressure gradients due to viscous deformation. However, the mechanisms might not manifest themselves due to specific model choices for the constitutive rheological relations. In general, melt flows due to pressure gradients. Pressure can be decomposed into compaction pressure, dynamic pressure and buoyancy (Equation 3.9) in the Darcy-like flow equation (Equation 3.5):

$$\phi(\mathbf{v_f} - \mathbf{v_s}) = -\frac{K}{\mu}[\nabla\mathcal{P} + \nabla p^* + \Delta\rho\mathbf{g}] \tag{4.12}$$

The non-dimensionalized buoyancy term is of order unity such that all the generated melt flows upwards, as indicated by $\hat{\mathbf{k}}$ in Equation 3.48. The other two pressure gradients will move melt horizontally if the gradient in the horizontal direction is also of order unity or larger, therefore focusing melt. Compaction and dynamic pressures depend on volumetric and shear deformations respectively. Therefore, the specified rheological relations (i.e shear and bulk viscosities) in these models play an important role in determining the focusing mechanisms observed.

**Melting rate suction/focusing**

This mechanism was first observed recently in a model with grain growth evolution and grain size dependence viscosity (*Turner et al.*, 2017) (numbered one in Figure 4.13). In our models, the same mechanism is observed with a variable viscosity without any grain size dependence. We propose that even with a simpler rheological relationship for shear viscosity, this focusing mechanism will still persist, since the physics behind the melting rate focusing is a basic aspect of the two phase flow equations as discussed in Chapter 3. Melt generated deep in the melting region is focused towards the ridge axis due to compaction pressure, $\mathcal{P}$, from melting rate gradient (as observed in Figure 4.4). The horizontal gradient for compaction pressure is the strongest within $\sim$40 km of the ridge axis and it does not seem to vary significantly with half spreading rates (Figure 4.10). The strength of the melting rate focusing largely depends on the bulk viscosity, $\zeta$ as shown in chapter 3.

**Decompaction layers**

Decompaction layers are melt rich layers along which melt is focused towards the ridge axis (*Sparks and Parmentier*, 1991; *Hebert and Montési*, 2010; *Keller et al.*, 2017). This melt focusing mechanism is illustrated in Figure 4.13. Melt generated in the melting region is more buoyant than the surrounding mantle and segregates upwards. In some of the models with slower spreading rates, melt leaves the melting region and forms porosity waves. Melt encounters the thermal boundary layer at the Lithosphere-Astenosphere Boundary (LAB), where some melt freezes into the colder stronger lithosphere and the rest is deflected along this decompaction layer towards the ridge axis. This layer is known as decompaction layer simply because the mantle matrix has to decompact to accommodate the melt flow towards the ridge axis. Melt focusing by decompaction layers works similar to an inverted funnel.

### Ridges suction

As tectonic forces pull oceanic plates apart, a negative dynamic pressure pulls melt towards the ridge axis from the surrounding region due to incompressible shear (*Spiegelman and McKenzie*, 1987; *Morgan*, 1987). This ridge suction focuses melt in the vicinity of the ridge axis (*Spiegelman and McKenzie*, 1987; *Morgan*, 1987). The length scale over which this pressure exerts itself is

$$L_{ridge} = \sqrt{\frac{\eta U_0}{\Delta \rho g}} \tag{4.13}$$

where it is a balance between incompressible shear and buoyancy (*Spiegelman*, 1993b,c). Tectonic forces pull on the plates more as half spreading rate $U_0$ increases, therefore dynamic pressure should increase in magnitude as well. However, the temperature dependent shear viscosity is a tradeoff that has the opposite effect on dynamic pressure, decreasing dynamic pressure with increasing half spreading rate (Figure 4.9) as the upper mantle weakens. In a fully coupled model with temperature dependent shear viscosity and a weak ridge axis, this ridge suction focusing effect will be kept small.

### Melt flux proportion from dominant focusing mechanisms

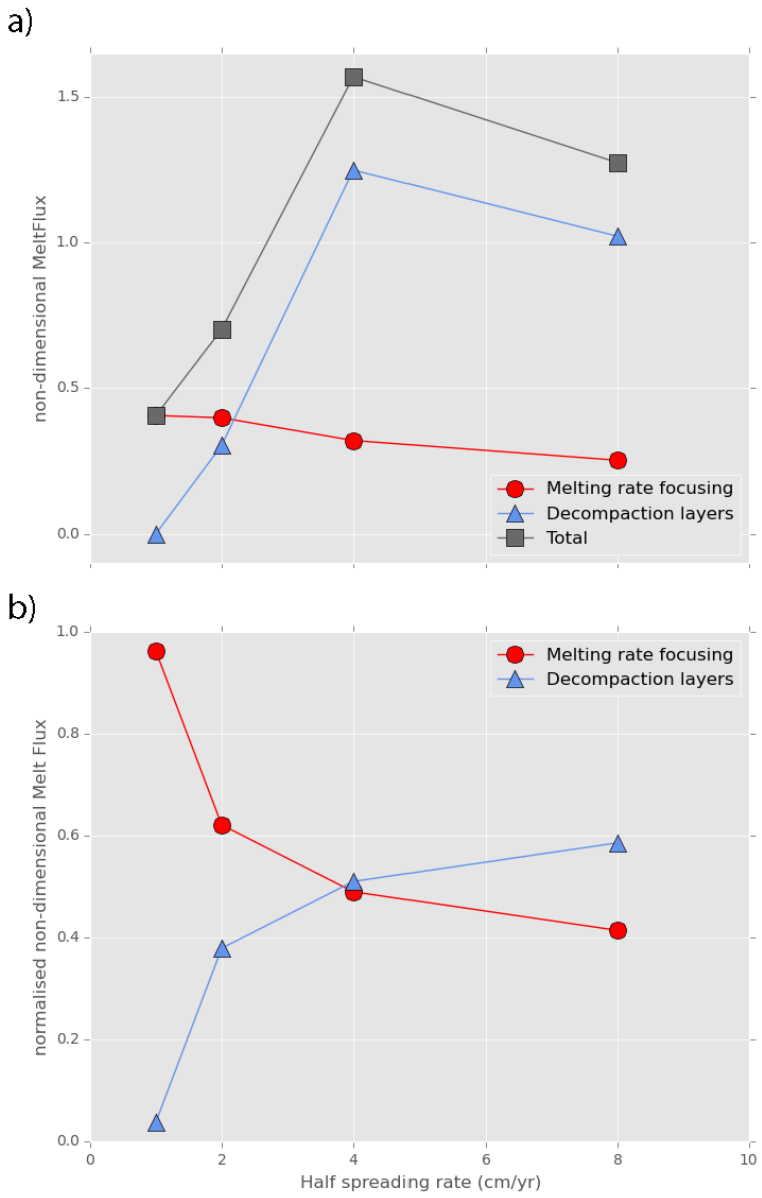


**Figure 4.14**: a) Cumulative non-dimensional melt flux from decompaction layers (blue triangles), magmatic focusing (red circles) and total melt flux (purple squares) versus spreading rates calculated from our models. The cumulative melt flux is calculated from a profile across the domain at 5 km depth. Melt flux from magmatic focusing does not vary significantly with $U_0$, decreasing slightly with increasing $U_0$. It is the dominant melt focusing mechanism that focuses melt to the ridge axis in model $U1$ with $U_0 = 1$ cm/yr.

Figure 4.14 (continued): The decompaction layers focusing contributes to the total melt flux significantly for increasing $U_0$. b) Melt flux contribution from the two melt focusing mechanisms normalized by the total melt flux versus half spreading rates, $U_0$. The melt flux contribution from decompaction layers focusing increases with increasing $U_0$ while that from magmatic focusing decreases.

To make sense of the melt focusing contributions from the melt focusing mechanisms in our models, we analyze the melt flux profiles at 5 km depths across the domain, where the melt focused from the two dominant melt focusing mechanisms (decompaction layers and melting rate focusing) are distinct. We integrate the melt flux from each focusing mechanism and compare them on Figure 4.14, along with the total melt flux averaged over time that leaves the top boundary to create oceanic crust (grey squares in Figure 4.14a). The averaged total melt flux increases with half spreading rate below 4 cm/yr and decreases above 4 cm/yr.

The total melt flux comes from melt focused deep in the melting region by the melting rate suction and melt focused on the sides by decompaction layers. The proportion of melt flux focused by melting rate suction decreases slightly with half spreading rate (red line in Figure 4.14a), while the proportion of melt flux focused by decompaction layers mimics the pattern of the total melt flux, but is offset vertically (blue line in Figure 4.14a). For model $U1$ with the slowest half spreading rate, the melt that forms oceanic crust is only those focused by the melting rate suction. When these melt flux proportions are normalised by the total melt flux, the proportion of melt flux focused by melting rate suction decreases with half spreading rate while the opposite is true for the proportion of melt flux focused by decompaction layer (Figure 4.14b).

### 4.5.2 Geophysical and geochemical implications

Magnetotelluric (MT) survey of the East Pacific Rise suggests that melt is focused even before reaching the decompaction layers (*Key et al.*, 2013). The shallow upper mantle is resistive and devoid of melt where the decompaction layers are predicted to be in previous models and models presented in this study. The MT method is sensitive to conductors but less so to resistors, suggesting that the

upper mantle might be less resistive than shown in *Key et al.* (2013). Since the porosities shown in our models are volumetric averages of each mesh element, it is possible that there exist high porosity channels that transport melt fast along this decompaction layer that are too small to be detected by geophysical observations. However, if the interpretations of the MT surveys are accurate, one possibility to reconcile this discrepancy would be that the recently recognized melting rate focusing is stronger in reality compared to our models, since it is the only mechanism in our models that focuses melt in the melting region before it reaches the thermal boundary layer. To strengthen the melting rate focusing, either the melting rate has to increase or change its structure without increasing the total melt production or the bulk viscosity has to be larger. Both of these would focus melt within the melting region before they leave the melting region buoyantly upwards to reach the decompaction layer. Since the structure of the melt production field is largely determined by the solid flow field that is relatively well understood, it is more probable that the bulk viscosity is larger in reality.

The melt that ends up in decompaction layer comes from deeper low degree melts. Some of this melt freezes into the strong cold lithosphere. Therefore, we should expect geochemical signature for low degree melts (higher concentrations of sodium and titanium oxides, $Na_2O$ and $TiO_2$, (*McDonough and Rudnick*, 1998)) for off axis melting/volcano if the melt escapes. If off axis melt freezes in completely, the last remaining melt will be enriched since the first solid that froze in will be depleted. Therefore, depending on the freezing patterns (which depends on the parameterization of freezing), we expect to see a geochemical signature when looking at exhumed lithosphere created at this setting.

In contrast, the central melting region has a mixture of deeper low degree melts and shallower high degree melts. Melt is focused deep in the melting region to the ridge axis by the melting rate focusing mechanism. Both the melts from the central melt region and the decompaction layers converge at the ridge axis to form oceanic crust. We can expect either a well mixed melt or distinct melts from these two regions depending on the mixing as melt is extracted to form oceanic crust. The former would give a smaller range of geochemical signatures while the

latter would give variations of either the mixed signature from the central melting or the deep low degree melting from the sides. For slower spreading rates, the models suggest that there might be pulses of melt injection due to porosity waves. In addition, the results from model $U1$ suggest that melt is only focused by the melting rate suction and therefore this should provide us a way to test the difference between the geochemical signature of mid-ocean ridge basalts at slow spreading versus those at faster spreading rates.

## 4.6 Conclusion

We present a suite of two-phase flow models applied to mid-ocean ridge setting with varying half spreading rates. We describe the model setup with varying half spreading rates along with corresponding parameters for the initial porosity pipe and freezing rate constant. First, our M3LT models predict oceanic crustal production versus spreading rates that are within the observations from geophysical surveys. The geophysical observations suggest a trend of decreasing variability in crustal production rate with increasing spreading rate. Our models suggest that the persistence of porosity waves at slower spreading rates may contribute to this observed variability. These porosity waves modulate the melt flux coming out the top boundary to form oceanic crust for half spreading rates less than 4 cm/yr.

Secondly, we observe three focusing mechanisms in our models: ridge suction, decompaction layers and a newly observed melting rate focusing from structure of the melting field. Our analysis shows that proportion of melt focused by melting rate focusing does not change significantly with half spreading rate, decreasing only slightly with increasing half spreading rate. We also show that melt focusing from decompaction layers becomes significant when the half spreading rate is more than 2 cm/yr. Decompaction layers and melting rate focusing are the two dominant mechanisms that focus melt to the ridge axis. Ridge suction affects melt flow only around the ridge axis.

Chapter 4, in part is currently being prepared for submission for publication of the material. Shi Sim, Marc Spiegelman, Dave R Stegman and Cian Wilson. The dissertation/thesis author was the primary investigator and author of this

material. I would like to acknowledge my co-authors, Marc Spiegelman, Dave R Stegman and Cian Wilson.

# References

Aharonov, E., J. Whitehead, P. Kelemen, and M. Spiegelman (1995), Channeling instability of upwelling melt in the mantle, *Journal of Geophysical Research: Solid Earth*, *100*(B10), 20,433–20,450.

Bown, J. W., and R. S. White (1994), Variation with spreading rate of oceanic crustal thickness and geochemistry, *Earth and Planetary Science Letters*, *121*(3-4), 435–449.

Cannat, M. (1993), Emplacement of mantle rocks in the seafloor at mid-ocean ridges, *Journal of Geophysical Research: Solid Earth*, *98*(B3), 4163–4172.

Carbotte, S. M., D. K. Smith, M. Cannat, and E. M. Klein (2016), Tectonic and magmatic segmentation of the global ocean ridge system: A synthesis of observations, *Geological Society, London, Special Publications*, *420*(1), 249–295.

Dick, H., J. Lin, and H. Schouten (2003), An ultraslow-spreading class of ocean ridge, *Nature*, *426*(6965), 405.

Dullien, F. A. (2012), *Porous media: fluid transport and pore structure*, Academic press.

Forsyth, D. W., S. C. Webb, L. Dorman, and Y. Shen (1998a), Phase velocities of Rayleigh waves in the MELT experiment on the East Pacific Rise, *Science*, *280*(5367), 1235–1238.

Forsyth, D. W., D. S. Scheirer, S. C. Webb, and L. M. Dorman (1998b), Imaging the deep seismic structure beneath a mid-ocean ridge: The MELT experiment, *Science*, *280*(5367), 1215–1220.

Fowler, A. (1985), A mathematical model of magma transport in the asthenosphere, *Geophysical & Astrophysical Fluid Dynamics*, *33*(1-4), 63–96.

Harding, J. L., H. J. Van Avendonk, N. W. Hayman, I. Grevemeyer, C. Peirce, and A. Dannowski (2017), Magmatic-tectonic conditions for hydrothermal venting on an ultraslow-spread oceanic core complex, *Geology*, *45*(9), 839–842.

Hebert, L. B., and L. G. Montési (2010), Generation of permeability barriers during melt extraction at mid-ocean ridges, *Geochemistry, Geophysics, Geosystems*, *11*(12).

Hirschmann, M. M. (2000), Mantle solidus: Experimental constraints and the effects of peridotite composition, *Geochemistry Geophysics Geosystems*, *1*(10).

Hirth, G., and D. Kohlstedt (2003), Rheology of the upper mantle and the mantle wedge: A view from the experimentalists, *Inside the subduction Factory*, 83–105.

Holtzman, B., D. Kohlstedt, M. Zimmerman, F. Heidelbach, T. Hiraga, and J. Hustoft (2003a), Melt segregation and strain partitioning: implications for seismic anisotropy and mantle flow, *Science*, *301*(5637), 1227–1230.

Holtzman, B., N. Groebner, M. Zimmerman, S. Ginsberg, and D. Kohlstedt (2003b), Stress-driven melt segregation in partially molten rocks, *Geochemistry, Geophysics, Geosystems*, *4*(5).

Karato, S.-i., and P. Wu (1993), Rheology of the upper mantle: a synthesis, *Science*, *260*(5109), 771–778.

Katz, R. F., M. Spiegelman, and C. H. Langmuir (2003), A new parameterization of hydrous mantle melting, *Geochemistry Geophysics Geosystems*, *4*(9).

Keller, T., R. F. Katz, and M. M. Hirschmann (2017), Volatiles beneath mid-ocean ridges: Deep melting, channelised transport, focusing, and metasomatism., *Earth and Planetary Science Letters*, *464*, 55–68.

Key, K., S. Constable, L. Liu, and A. Pommier (2013), Electrical image of passive mantle upwelling beneath the northern East Pacific Rise, *Nature*, *495*(7442), 499–502.

Kohlstedt, D. L., and B. K. Holtzman (2009), Shearing melt out of the earth: An experimentalist's perspective on the influence of deformation on melt extraction, *Annual Review of Earth and Planetary Sciences*, *37*, 561–593.

Macdonald, K. C. (1982), Mid-ocean ridges: Fine scale tectonic, volcanic and hydrothermal processes within the plate boundary zone, *Annual Review of Earth and Planetary Sciences*, *10*(1), 155–190.

McDonough, W. F., and R. L. Rudnick (1998), Mineralogy and composition of the upper mantle, *Reviews in mineralogy*, *37*, 139–164.

McKenzie, D. (1984), The Generation and Compaction of Partially Molten Rock, *Journal of Petrology*, 1–53.

Morgan, J. P. (1987), Melt migration beneath mid?ocean spreading centers, *Geophysical Research Letters*, *14*(12), 1238–1241.

Ribe, N. M. (1987), Theory of melt segregation: a review, *Journal of volcanology and geothermal research*, *33*(4), 241–253.

Rudge, J. F. (2017), Textural equilibrium melt geometries around tetrakaidecahedral grains, *arXiv preprint arXiv:1709.03303*.

Schmeling, H., N. Bagdassarov, D. Laporte, and A. Thompson (2000), Partial melting and melt segregation in a convecting mantle, *Physics and Chemistry of Partially Molten Rocks*, *11*, 141–178.

Scott, D. R., and D. J. Stevenson (1984), Magma solitons, *Geophysical Research Letters*, *11*(11), 1161–1164.

Scott, D. R., and D. J. Stevenson (1986), Magma ascent by porous flow, *Journal of Geophysical Research: Solid Earth*, *91*(B9), 9283–9296.

Sim, S. J., M. Spiegelman, D. R. Stegman, and C. Wilson (2018), M3LT: A new model to explore the dynamics of Melt in the Mantle beneath Mid-ocean ridges.

Simpson, G., M. Spiegelman, and M. I. Weinstein (2010a), A multiscale model of partial melts: 1. effective equations, *Journal of Geophysical Research: Solid Earth*, *115*(B4).

Simpson, G., M. Spiegelman, and M. I. Weinstein (2010b), A multiscale model of partial melts: 2. numerical results, *Journal of Geophysical Research: Solid Earth*, *115*(B4).

Sotin, C., and E. Parmentier (1989), Dynamical consequences of compositional and thermal density stratification beneath spreading centers, *Geophysical Research Letters*, *16*(8), 835–838.

Sparks, D. W., and E. M. Parmentier (1991), Melt extraction from the mantle beneath spreading centers, *Earth and Planetary Science Letters*, *105*(4), 368–377.

Spiegelman, M. (1993a), Physics of Melt Extraction: Theory, Implications and Applications, *Philosophical Transactions of the Royal Society A: Mathematical, Physical and Engineering Sciences*, *342*(1663), 23–41.

Spiegelman, M. (1993b), Flow in deformable porous media. Part 1 Simple analysis, *Journal of Fluid Mechanics*, *247*, 17–38.

Spiegelman, M. (1993c), Flow in deformable porous media. part 2 numerical analysis–the relationship between shock waves and solitary waves, *Journal of Fluid Mechanics*, *247*, 39–63.

Spiegelman, M. (1996), Geochemical consequences of melt transport in 2-D: The sensitivity of trace elements to mantle dynamics, *Earth and Planetary Science Letters*, *139*(1-2), 115–132.

Spiegelman, M., and T. Elliott (1993), Consequences of melt transport for uranium series disequilibrium in young lavas, *Earth and Planetary Science Letters*, 118(1-4), 1-20.

Spiegelman, M., and D. McKenzie (1987), Simple 2-D models for melt extraction at mid-ocean ridges and island arcs, *Earth and Planetary Science Letters*, *83*(1-4), 137-152.

Spiegelman, M., P. B. Kelemen, and E. Aharonov (2001), Causes and consequences of flow organization during melt transport: The reaction infiltration instability in compactible media, *Journal of Geophysical Research: Solid Earth*, *106*(B2), 2061–2077.

Spiegelman, M., D. A. May, and C. R. Wilson (2016), On the solvability of incompressible Stokes with viscoplastic rheologies in geodynamics, *Geochemistry Geophysics Geosystems*, *17*(6), 2213–2238.

Turner, A. J., R. F. Katz, M. D. Behn, and T. Keller (2017), Magmatic Focusing to Mid-Ocean Ridges: The Role of Grain-Size Variability and Non-Newtonian Viscosity, *Geochemistry Geophysics Geosystems*, *23*(1), 15.

Vera, E., J. Mutter, P. Buhl, J. Orcutt, A. Harding, M. Kappus, R. Detrick, and T. Brocher (1990), The structure of 0-to 0.2-my-old oceanic crust at 9 n on the east pacific rise from expanded spread profiles, *Journal of Geophysical Research: Solid Earth*, *95*(B10), 15,529–15,556.

Wark, D. A., and E. B. Watson (1998), Grain-scale permeabilities of texturally equilibrated, monomineralic rocks, *Earth and Planetary Science Letters*, *164*(3-4), 591–605.

White, R. S., D. McKenzie, and R. K. O'Nions (1992), Oceanic crustal thickness from seismic measurements and rare earth element inversions, *Journal of Geophysical Research: Solid Earth*, *97*(B13), 19,683–19,715.

White, R. S., T. A. Minshull, M. J. Bickle, and C. J. Robinson (2001), Melt generation at very slow-spreading oceanic ridges: Constraints from geochemical and geophysical data, *Journal of Petrology*, *42*(6), 1171–1196.

Wilson, C. R., M. Spiegelman, and P. E. van Keken (2017), TerraFERMA: The

Transparent Finite Element Rapid Model Assembler for multiphysics problems in Earth sciences, *Geochemistry Geophysics Geosystems*, *18*(2), 769–810.

Zhu, W., C. David, and T. Wong (1995), Network modeling of permeability evolution during cementation and hot isostatic pressing, *Journal of Geophysical Research*, *100*(B8), 15451-15464.

# Chapter 5

# Conclusions

## 5.1 Global mid-ocean ridge depths

I did a global study of depths of mid-ocean ridges using three dimensional whole earth mantle convection models. The mantle convection models have varying amount of continents and mantle potential temperature to simulate different periods in Earth's history. The models show that mid-ocean ridges likely remained submerged since Hadean eon. From the analyses, I conclude that the average depths of mid-ocean ridges might not have varied $> 500$ m from early Earth up until modern day.

## 5.2 Two phase flows beneath mid-ocean ridge

I present a new open-source two phase flow models, Melt in the Mantle beneath Mid-ocean ridges, M3LT. These models are built using TerraFERMA and consist of a set of structured input files for TerraFERMA that describe all the model choices required to solve the complex two-phase models described here. By building M3LT on TerraFERMA, I provide a consistent mechanism for reproducing, understanding and potentially modifying published models in a way that the derived models can also be used and shared.

I describe in detail the model set up for our example model with half spreading rate of $U_0 = 4$ cm/yr. I discuss the various focusing mechanisms seen in our example model, highlighting the new magmatic focusing mechanism. This new

mechanism is a natural consequence of the two-phase flow equations, creating a compaction pressure suction from the melting rate gradient. It focuses a significant proportion of the melt generated from a wide region beneath the mid-ocean ridges to a small area and may explain two of the fundamental observations of mid-ocean ridges, the extreme narrowness of the neo-volcanic zone and the relative constancy of crustal thickness independent of spreading rate for intermediate to fast spreading ridges.

I present a suite of two-phase flow models applied to mid-ocean ridge setting with varying half spreading rates using M3LT. I describe the model set up with varying half spreading rates along with corresponding parameters for the initial porosity pipe and freezing rate constant. The M3LT models predict oceanic crustal production versus spreading rates that lie within the observations. The geophysical observations suggest a trend of decreasing variability in crustal production rate with increasing spreading rate. The M3LT models suggest that the persistence of porosity waves at slower spreading rates may contribute to this observed variability. These porosity waves modulate the melt flux coming out the top boundary to form oceanic crust for half spreading rates less than 4 cm/yr.

Three focusing mechanisms are observed in our models: ridge suction, decompaction layers and a recently recognized magmatic focusing from melting rate focusing Analyses show that magmatic focusing does not change significantly with half spreading rate, decreasing only slightly with increasing half spreading rate. I also show that melt focusing from decompaction layers becomes significant when the half spreading rate is more than 2 cm/yr. Decompaction layers and magmatic focusing are the two dominant mechanisms that focus melt to the ridge axis. Ridge suction affects melt flow only around the ridge axis.

Future work includes an exploration of what the seismic and electromagnetic signatures of these models are. There is much to be done as the M3LT models gets us closer to reality but are still far from perfect. Working on the fully coupled two phase problem would shed light on some inconsistencies in the M3LT models. Exploration of parameters such as mantle potential temperature, melting and freezing parameterization, enrichment/depletion and tracking trace elements

of varying partition coefficient would also be enlightening.

# Appendix A

# Bulk viscosity

## A.1 Rheology: Bulk Viscosity $\xi$

This is an exploration of mixture models for bulk viscosity. Strictly in the two phase flow models applied to Earth material, we are dealing with incompressible individual materials but the solid is compressible in the porous sense. The compaction pressure, $\mathcal{P}$, is defined as:

$$\mathcal{P} = \zeta \nabla \cdot \mathbf{v_s} \tag{A.1}$$

where $\zeta$ is the bulk viscosity and $\mathbf{v_s}$ is the solid velocity. The bulk viscosity used in our models is:

$$\zeta = \frac{\eta}{\phi} \tag{A.2}$$

where $\eta$ is the shear viscosity and $\phi$ is the porosity.

We can regularize bulk viscosity to depend on compaction pressure such that when compaction pressure gets too large and yields at a failure criteria, bulk viscosity has to decrease so that the solid matrix can decompact. The conditions that need to be fulfilled follow:

1) When $\mathcal{P}^+ \to \mathcal{P}_f$, $\frac{1}{\zeta} \to \frac{1}{\zeta_{min}}$

2) When $\phi \to 0$, $\zeta \to \zeta_{max}$

3) No negative $\zeta$

4) Has to work for both $\mathcal{P}^+ > \mathcal{P}_f$ or $\mathcal{P}^+ < \mathcal{P}_f$

$\mathcal{P}^+$ is the compaction pressure approaching from the positive side, $\mathcal{P}_f$ is the compaction pressure at failure, $\zeta_{min}$ is the minimum bulk viscosity and $\zeta_{max}$ is the

maximum bulk viscosity. The goal is to find a mixture model that can fulfill all these conditions. We try three different mixture models.

### A.1.1 Mixture model 1

$$\zeta = \zeta_{min} + \left[\frac{1}{\zeta_\phi} + \frac{P^+}{\zeta P_f}\right]^{-1} \tag{A.3}$$

There are two ways to look at this case, $\frac{1}{\zeta}$ or $\zeta$.

**a** : $\frac{\mathbf{1}}{\zeta}$

$$\frac{1}{\zeta} = \frac{1}{\zeta_{min} + \frac{1}{\frac{1}{\zeta_\phi} + \frac{P^+}{\zeta P_f}}}$$

$$\frac{1}{\zeta} = \frac{\left(-\frac{\zeta_{min}}{\zeta_\phi} - 1 + \frac{P^+}{P_f}\right) \pm \sqrt{\left(\frac{\zeta_{min}}{\zeta_\phi} + 1 - \frac{P^+}{P_f}\right)^2 + 4\frac{\zeta_{min}}{\zeta_\phi}\frac{P^+}{P_f}}}{2\zeta_{min}\frac{P^+}{P_f}} \tag{A.4}$$

**b** : $\zeta$

$$\zeta = \zeta_{min} + \frac{1}{\left[\frac{1}{\zeta_\phi} + \frac{P^+}{\zeta P_f}\right]}$$

$$\zeta = \frac{1}{2}\left[(\zeta_{min} - \zeta_\phi\left(1 - \frac{P^+}{P_f}\right)) \pm \sqrt{(\zeta_\phi\left(1 - \frac{P^+}{P_f}\right) - \zeta_{min})^2 + 4\zeta_{min}\zeta_\phi\frac{P^+}{P_f}}\right] \tag{A.5}$$

**Case 1: At failure, $P^+ \to P_f$**

Using the **a** : $\frac{\mathbf{1}}{\zeta}$ solution

$$\frac{1}{\zeta} = \frac{-\frac{\zeta_{min}}{\zeta_\phi} \pm \sqrt{\left(\frac{\zeta_{min}}{\zeta_\phi}\right)^2 + 4\frac{\zeta_{min}}{\zeta_\phi}}}{2\zeta_{min}}$$

As $\phi \to 0$, $\zeta_\phi \to \infty$

$$\frac{1}{\zeta} = 0$$

Thus, we need to have an upper bound $\zeta_{max}$ so that as $\phi \to 0$, $\zeta_\phi \to \zeta_{max}$

Using the $\mathbf{b} : \zeta$ solution:

$$\zeta = \frac{1}{2}\left[\zeta_{min} \pm \sqrt{\zeta_{min}^2 + 4\zeta_{min}\zeta_\phi}\right]$$

$$\zeta = \frac{1}{2}\left[\zeta_{min} \pm \sqrt{\zeta_{min}^2 + 4\zeta_{min}\zeta_{max}}\right]$$

If $\zeta_{max} >> \zeta_{min}$ such that $\zeta_{max} = \alpha\zeta_{min}$ where $\alpha << 1$

$$\zeta = \frac{1}{2}\left[\zeta_{min} \pm \sqrt{\zeta_{min}^2 + 4\alpha\zeta_{min}^2}\right]$$

$$\zeta = \frac{1}{2}\left[\zeta_{min} \pm \sqrt{\zeta_{min}^2(1+4\alpha)}\right] \approx \frac{1}{2}\left[\zeta_{min} \pm \zeta_{min}\right] \approx \zeta_{min} \tag{A.6}$$

**Case 2: Not at failure, as $\phi \to 0$, $\zeta_\phi \to \infty$**

Using the $\mathbf{a} : \frac{1}{\zeta}$ solution

$$\frac{1}{\zeta} = \frac{\left(-1 + \frac{P^+}{P_f}\right) \pm \sqrt{\left(1 - \frac{P^+}{P_f}\right)^2}}{2\zeta_{min}\frac{P^+}{P_f}}$$

therefore,

$$\frac{1}{\zeta} = \frac{\frac{P^+}{P_f} - 1}{\zeta_{min}\frac{P^+}{P_f}} \;\; or \;\; 0$$

for $P^+ < P_f$, $\frac{1}{\zeta} < 0$ and for $P^+ > P_f$, $\frac{1}{\zeta} > 0$.

### A.1.2 Mixture model 2

$$\frac{1}{\zeta} = \frac{1}{\zeta_\phi} + \frac{P^+}{P_f(\zeta + \zeta_{min})} \tag{A.7}$$

$\mathbf{A} : \zeta$

$$\frac{1}{\zeta} = \frac{P_f(\zeta + \zeta_{min}) + \zeta_\phi P^+}{\zeta_\phi P_f(\zeta + \zeta_{min})}$$

$$\zeta = \frac{1}{2}\left[(\zeta_\phi(1 - \frac{P^+}{P_f}) - \zeta_{min}) \pm \sqrt{(\zeta_{min} + \zeta_\phi(\frac{P^+}{P_f} - 1))^2 + 4\zeta_\phi\zeta_{min}}\right] \tag{A.8}$$

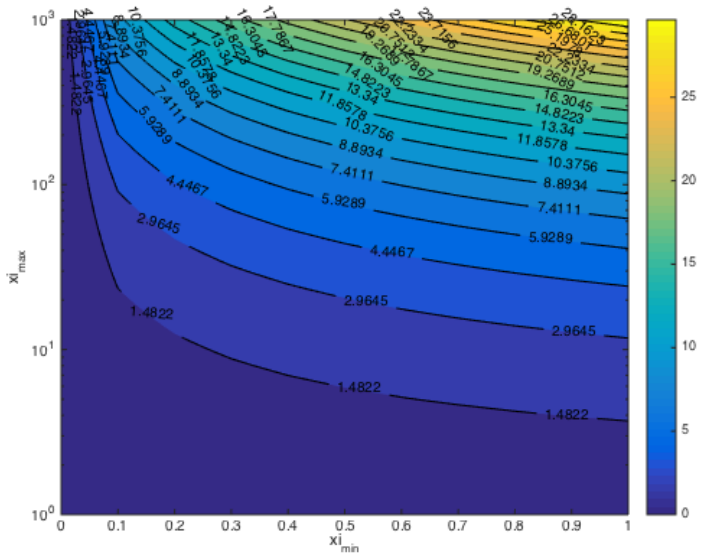


**Figure A.1**: $\xi_{min}$ for $P^+ \to P_f$, $\phi \to 0$, $\xi \to \xi_{max}$

**B** : $\frac{1}{\zeta}$

Divide throughout by $\zeta^2$ and $\zeta_\phi$ and rearranging:

$$\frac{1}{\zeta_\phi} + \frac{1}{\zeta}(\frac{\zeta_{min}}{\zeta_\phi} + \frac{P^+}{P_f} - 1) - \frac{1}{\zeta^2}\zeta_{min} = 0$$

$$\frac{1}{\zeta} = \frac{1}{2}\left[(\frac{\zeta_{min}}{\zeta_\phi} + \frac{P^+}{P_f} - 1) \pm \sqrt{(1 - \frac{P^+}{P_f} - \frac{\zeta_{min}}{\zeta_\phi})^2 + 4\frac{\zeta_{min}}{\zeta_\phi}}\right] \tag{A.9}$$

**Case 1: At failure,** $P^+ \to P_f$

$$\zeta = \frac{1}{2}\left[-\zeta_{min} \pm \sqrt{(\zeta_{min})^2 + 4\zeta_\phi\zeta_{min}}\right]$$

$$\frac{1}{\zeta} = \frac{1}{2}\left[\frac{\zeta_{min}}{\zeta_\phi} \pm \sqrt{(\frac{\zeta_{min}}{\zeta_\phi})^2 + 4\frac{\zeta_{min}}{\zeta_\phi}}\right]$$

further, as $\phi \to 0$, $\zeta_\phi \to \infty$

$$\frac{1}{\zeta} = 0$$

As seen in the first mixture model, we want $\zeta_\phi \to \zeta_{max}$. This case has a negative with $-\zeta_{min}$, which is not ideal.

**Case 2: Not at failure, as $\phi \to 0$, $\zeta_\phi \to \infty$**

$$\frac{1}{\zeta} = \frac{1}{2}\left[(\frac{P^+}{P_f} - 1) \pm \sqrt{(1 - \frac{P^+}{P_f})^2}\right]$$
$$\frac{1}{\zeta} = (\frac{P^+}{P_f} - 1) \ \ or \ \ 0 \tag{A.10}$$

for $P^+ < P_f$, $\frac{1}{\zeta} < 0$ and for $P^+ > P_f$, $\frac{1}{\zeta} > 0$.

### A.1.3 Mixture model 3

$$\zeta = (1 - C)\zeta_{\phi'} + C\zeta_{min} \tag{A.11}$$

where

$$C = \frac{1}{2}\left[\tanh\left(20\left(\frac{P^+}{P_f} - 1\right)\right) + 1\right] \tag{A.12}$$

and

$$\frac{1}{\zeta_{\phi'}} = \frac{1}{\zeta_\phi} + \frac{1}{\zeta_{\max}} \tag{A.13}$$

so as $\phi \to 0$, $\zeta_\phi \to \infty$ so $\frac{1}{\zeta_{\phi'}} \to \frac{1}{\zeta_{\max}}$ since $\frac{1}{\zeta_\phi} \to 0$

**Case 1: At failure, $P^+ \to P_f$**

$$\zeta = \zeta_{min} \tag{A.14}$$

**Case 2: Not at failure, as $\phi \to 0$, $\zeta_\phi \to \infty$**

for $P^+ < P_f$

$$\frac{1}{2}\left[\tanh\left(20\left(\frac{P^+}{P_f} - 1\right)\right)\right] = 0 \tag{A.15}$$

therefore

$$\zeta = \zeta_{\phi'} = \zeta_{max} \tag{A.16}$$

for $P^+ > P_f$, $\tanh \to 1$

$$\zeta = \zeta_{min} \tag{A.17}$$